ELECTROKINETIC CONCENTRATION ENRICHMENT WITHIN A MICROFLUIDIC DEVICE INTEGRATED WITH A HYDROGEL MICROPLUG

A Dissertation

by

RAHUL RAJESH DHOPESHWARKAR

Submitted to the Office of Graduate Studies of
Texas A&M University
in partial fulfillment of the requirements for the degree of

DOCTOR OF PHILOSOPHY

August 2007

Major Subject: Chemical Engineering

ELECTROKINETIC CONCENTRATION ENRICHMENT WITHIN A MICROFLUIDIC DEVICE INTEGRATED WITH A HYDROGEL MICROPLUG

A Dissertation

by

RAHUL RAJESH DHOPESHWARKAR

Submitted to the Office of Graduate Studies of
Texas A&M University
in partial fulfillment of the requirements for the degree of

DOCTOR OF PHILOSOPHY

Approved by:

Co-Chairs of Committee,	Richard M. Crooks
	Daniel F. Shantz
Committee Members,	Victor M. Ugaz
	Raymond E. Schaak
Head of Department,	N. K. Anand

August 2007

Major Subject: Chemical Engineering

ABSTRACT

Electrokinetic Concentration Enrichment within a Microfluidic Device Integrated with a Hydrogel Microplug. (August 2007)

Rahul Rajesh Dhopeshwarkar, B.E., Shivaji University

Co-Chairs of Advisory Committee: Dr. Richard M. Crooks
Dr. Daniel F. Shantz

A simple and efficient technique for the concentration enrichment of charged species within a microfluidic device was developed. The functional component of the system is a hydrogel microplug photopolymerized inside the microfluidic channel. The fundamental properties of the nanoporous hydrogel microplug in modulating the electrokinetic transport during the concentration enrichment were investigated. The physicochemical properties of the hydrogel plug play a key role in determining the mode of concentration enrichment. A neutral hydrogel plug acts as a physical barrier to the electrophoretic transport of charged analytes resulting in size-based concentration enrichment. In contrast, an anionic hydrogel plug introduces concentration polarization effects, facilitating a size and charge-based concentration enrichment. The concentration polarization effects result in redistribution of the local electric field and subsequent lowering of the extent of concentration enrichment. In addition, an electroosmotic flow originating inside the pores of the anionic hydrogel manipulates the location of concentration enrichment. A theoretical model qualitatively consistent with the experimental observations is provided.

To my parents

and little sister

ACKNOWLEDGMENTS

I would like to express my deep gratitude to Prof. Richard M. Crooks for providing me a platform to conduct research in this exciting field of microfluidics. I truly appreciate his unwavering support, encouragement and interest in my work. To me, he has always been more than a mentor: a father figure and a wonderful human being. I am also thankful to Dr. Crooks for giving me the freedom to implement my own ideas and expand my scientific skills.

During the course of my studies, I had the privilege of interacting, on a professional as well as personal level, with many great intellectuals like Dr. Li Sun and Dr. Arnaud Chovin. I am also thankful to Dr. Ulrich Tallarek (Institut für Verfahrenstechnik, Otto-von-Guericke-Universität Magdeburg, Germany) for helpful discussions and valuable suggestions. It is also worth mentioning the camaraderie of all the Crooks group members, especially, Raphael Lezutekong, Yong-Gu Kim, Joohoon Kim, Kwok-Fan Chow, Javier Guerra, Mark Nguyen and of course, Angie Nelson and Debbie Maser. Special thanks to Dr. Daniel F. Shantz, Dr. Victor M. Ugaz and Dr. Raymond E. Schaak for their willingness to be a part of my committee.

This note of appreciation cannot be complete without thanking my mom (Aai), dad (Baba) and little sis Rasika for their affection and support all the way.

Financial support from the U.S. Department of Energy, Office of Basic Energy Sciences, is gratefully acknowledged.

NOMENCLATURE

a	characteristic channel dimension
A	cross-sectional area of a channel
C_i	local concentration of species ‘i’
$C_{i,bulk}$	bulk concentration of species ‘i’
d	diameter of a conduit
D_i	diffusivity of a species ‘i’
e	electronic charge, 1.60×10^{-19} C
E , $\overline{E}$	external electric field, scalar and vector representation
$\bar{f}_e$	electrostatic force
f_E	Lorentz body force
$\bar{f}_f$	frictional drag
F	Faraday constant, $N_A \cdot e$, 9.65×10^4 C/mol
G	modulus of elasticity or Young’s modulus
I	electric current density
$I^{\lim}$	limiting current density
J_i	molar flux of ionic species ‘i’
k_B	Boltzmann constant, 1.38×10^{-23} J/K
K_i	hydrogel partition coefficient for species ‘i’
l	length of a hydrogel plug
l_0	original length of a hydrogel plug
L	length of a channel
N_A	Avogadro’s number, 6.02×10^{23}/mol
N_{Re}	dimensionless Reynolds number
p	pressure

P_i	permeability of a species ‘i’ in hydrogel
q	ionic charge
Q	volumetric flow rate of liquid
r	ionic radius
R	ideal gas constant, 8.31 J/mol·K
T	absolute temperature
z_i	ionic charge number

Greek symbols

δ_D	the Debye length
ε	permittivity of a medium
ε_p	hydrogel porosity
ζ	zeta potential
η	liquid viscosity
μ_{eo}	electroosmotic mobility
μ_{ep}	electrophoretic mobility
v , $\overline{v}$	flow velocity, scalar and vector representation
$\overline{v}^{eff}$	effective flow velocity
ρ	liquid density
ρ_E	total charge density
σ	tensile stress
ϕ	electric potential

Subscripts

A	anionic species
ch	inside microchannel

crit	critical value
eo	electroosmotic
ep	electrophoretic
Fl	fluorescein
gel	hydrogel or intra-hydrogel
w	at wall
U	ultimate

Abbreviations

2D	two-dimensional
3D	three-dimensional
AA	acrylic acid
CP	concentration polarization
DBL	diffusion boundary layer
EDL	electric double layer
EGDMA	ethylene glycol dimethacrylate
EOF	electroosmotic flow
EP	electrophoresis
EZ	enrichment zone
HEMA	2-hydroxyethyl methacylate
MW	molecular weight
PDF	pressure driven flow
PDMS	poly(dimethylsiloxane)
Res	reservoir
ROI	region of interest
SCh	side channel

TABLE OF CONTENTS

Page

LIST OF FIGURES

FIGURE Page

FIGURE Page

FIGURE Page

FIGURE Page

FIGURE Page

CHAPTER I

INTRODUCTION

1.1 Motivation and Objectives

In a natural human quest of making things easier, miniaturization of chemical and bioanalytical systems has drawn the attention of the scientists and engineers around the globe. Employing such microfluidic devices offers many physical advantages, particularly those that are of interest to the biomedical field. However, their large-scale introduction is still limited, primarily due to the difficulties involved in the optical detection of low concentration species in these microscale geometries.

Sample preconcentration and concentration enrichment techniques present an attractive solution toward lowering the optical detection limits in microfluidic channels. Though a wide range of techniques have been implemented to achieve concentration enrichment, there is room for developing a simple, robust method with improved performance.

The central objective of this project is to develop a simple and efficient technique for the concentration enrichment of charged species within a microfluidic device (Chapter III). The project also underlines the application of the basic concepts of electrokinetically driven flows to miniaturized architectures and a detailed insight of the hydrogel based concentration enrichment technique (Chapter IV).

This dissertation follows the style of *Journal of the American Chemical Society*.

1.2 Background

1.2.1 micro-Total Analysis Systems (μTAS)

Since the emergence of the field of miniaturization of chemical/biochemical analytical systems in the early nineties, much of the effort has been devoted to the development of μTAS [micro-Total (Chemical) Analysis Systems], the concept introduced by Manz.[1] These devices, also known as 'lab-on-a-chip' devices, are easy to use, compact and portable. A built-in network of channels with cross-sectional dimensions ranging from 20 to few hundreds of microns makes them capable of integrating many reactions and operations such as electrophoresis, separation and detection on a single chip. Very small amounts (in picoliters) of reagents can be handled in these devices with the added advantages of larger surface-to-volume ratios and faster response times.[2, 3] The fluidic manipulations in these devices generally rely on electrokinetic transport due to the inherent difficulties involved in controlling flow by mechanical means.[4]

The μTAS are of vital importance for their application in the field of biomedical diagnostics and analysis, for example, their application to on-chip DNA separations would lend advances in sequencing of genomes, DNA fingerprinting, and disease identification.[5]

As the word 'Total' suggests, an ideal μTAS system should accomplish manipulation, recognition and analysis of a real-world sample. It should be able to accept a sample in its raw form, investigate and qualitatively/quantitatively describe the system in terms of an electrical signal. However, most of the recent advances in this

direction address the analysis step (chemical or biological sensing, electrophoresis, separation) only and their application is still limited due to the restrictions in direct handling of real-world samples in these microfluidic devices. In fact the sample pretreatment, that is, making a real-world sample appropriate for the chip-based analysis imposes a major challenge to the practicality of μTAS and requires a greater attention.[4, 6]

1.2.2 Sample Pretreatment

In general, on-line sample pretreatment can be divided into four main categories:[4] separation of sample from sample matrix, derivatization, biochemical sample pretreatment, and sample preconcentration. The separation step deals with the purification of real-world samples making them suitable for the chip-based manipulations. Derivatization includes labeling or complexation of the sample molecules to make them detectable. Bioprocess sample treatment is necessary considering the importance of sample analysis in genomic and proteomic studies. Finally, preconcentration implies on-chip compaction or concentration enrichment of the sample for superior detection.[4]

In microfluidic analytical systems, fluorescence detection is the most popular technique, due to its high sensitivity. However, many samples do not exhibit fluorescence and expensive derivatization methods are required to tag these species with compatible fluorescent markers. Hence, one has to regard other detection techniques such as UV-visible spectroscopy or electrochemical methods.[4, 6] However, the detection limits of these methods are much higher than fluorescence. In particular, for UV-visible

absorption, the signal strength (absorbance = molar absorptivity × length of optical path × sample concentration) depends upon optical path length dictated by the channel depth, but the microscale channel dimensions coupled with low concentrations result in poor detection sensitivity.

Though expensive, one way to solve this problem is to considerably improve the detection instrumentation and methodology. These efforts include multiplexing of the signal to enhance signal to noise ratio, employing laser-induced Raman microscopy and integrating optical elements such as organic light emitting diodes (OLEDs), vertical cavity surface emitting lasers (VCSELs), semiconductor photodetectors, microlenses and planar waveguides in microfluidic systems.[7] A rather cost-effective approach to tackle this problem is to increase concentration of sample molecules in the detection volume using on-chip sample preconcentration methods.

1.2.3 Sample Preconcentration

Various techniques have been employed for preconcentration in microfluidic channels. Field-amplified sample stacking (FASS)[8-11] is based on generating an abrupt change in the electrophoretic velocity of the sample ions near the boundary between low buffer concentration and high buffer concentration regions. The method is simple and can achieve high enrichment factors up to 1000-fold, but consumes two buffer solutions and considerable chip area. Solid-phase extraction (SPE)[12, 13] involves flow of sample solution over a treated surface or a bed of treated solids and preconcentration by subsequent attachment of the analyte to the immobilized phase. It can yield enrichment

factors of >500, but entails the complexity of incorporating an appropriate immobilized phase inside a microchannel. In isotachophoresis (ITP),[14-16] the sample solution is placed between a leading and a trailing buffer. The sample constituents separate into sharp zones based on their electrophoretic mobility and the extent of preconcentration is defined by the concentration of the leading electrolyte. Thus, choosing proper electrolytes for a given sample sometimes poses a serious challenge. Temperature gradient focusing (TGF)[17] presents an interesting approach for simultaneous preconcentration and separation of charged analytes by balancing their electrophoretic velocity with the bulk velocity of the buffer. The basic principle is similar to the electric field gradient focusing (EFGF)[18, 19] with the exception that a temperature gradient rather than an arrangement of electrodes is used to generate an electric field gradient, which in turn generates a velocity gradient. Enrichment factors > 10,000 can be achieved with TGF, but the technique requires a strongly temperature-dependent buffer, high operating voltages (~1000 V) and precise temperature control. A similar technique is isoelectric focusing (IEF)[20] in which a pH gradient is introduced in the system to allow focusing and separation of proteins based upon their isoelectric points (pIs). Recently, a method using laser-patterned nanoporous membranes as electrokinetic filtration media was reported to achieve preconcentration factors of > 1000-fold in less than 5 minutes for proteins.[21, 22] Ramsey and co-workers have reported a similar size-exclusion method using a thin polysilicate membrane.[23, 24] Other notable preconcentration techniques include electrokinetic micellar sweeping,[25, 26] entropic trapping,[27] and evaporation.[28] However, a highly reproducible convenient technique with less microfabrication

discrepancies, greater control over system variables and efficient performance is still awaited.

The previous studies in our group demonstrated an unusual approach for trapping and concentrating ssDNA inside a microfluidic channel by gaining spatial control over the electrokinetic velocity of the target analyte.[29] The three-dimensional (3D) microfluidic channel (see Figure 1(a)) was assembled by sandwiching a 10 μm thick polyester nanoporous membrane (PETE, 200 nm pores, 3×10^8 pores/cm^2) between two poly(dimethylsiloxane) (PDMS) monoliths. Each monolith incorporated a 5 mm long microchannel (100 μm wide and 25 μm deep) terminating in a cylindrical port (3 mm in diameter) for fluid delivery. Such 3D microfluidic architectures have also been used by Bohn and Sweedler[30-32] for controlled sample manipulation between non-planar microchannels and Whitesides[33] for simultaneous analysis of multiple chemical and biochemical interactions.

An electrical bias of 100 V between the waste reservoir (containing 1× TBE buffer, pH 8.4) and the source reservoir (containing 20-mer ssDNA solution prepared in the TBE buffer) revealed the possibility of generating a balance between electrophoretic velocity of the DNA and the electroosmotic velocity of the solvent (see Figure 1.1(b)). In the absence of similitude,[34] the local electroosmotic velocity inside the nanoporous membrane exceeded the electrophoretic velocity of the DNA in the microchannel resulting in a net zero velocity of the analyte near the nanoporous membrane. The approach was efficient yielding concentration enrichment factors up to 800 for 0.1 μg/mL DNA solution as a target analyte.

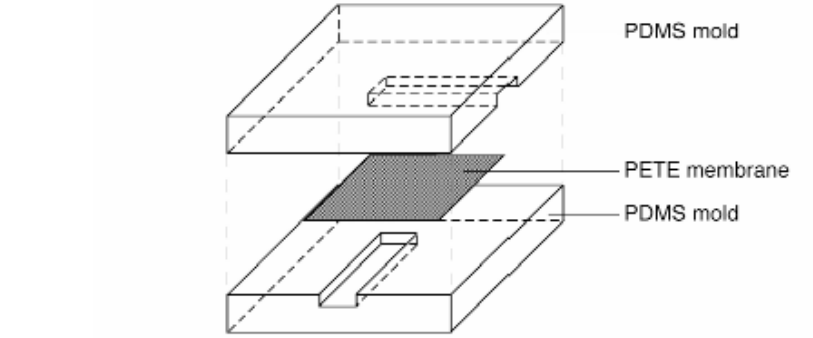

Disassembled View of a Fluidic Device Used in This Study

An optical photo of the device

a

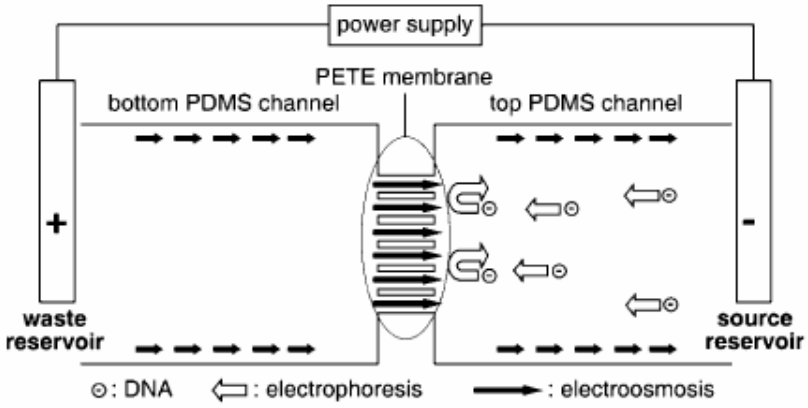

b

Figure 1.1. (a) The three-dimensional microfluidic device, and (b) the principle of operation for trapping and concentration of ssDNA. (Reprinted with permission from Dai et al.[29] Copyright © 2003 by the American Chemical Society.)

However, we discarded this preconcentration approach as it was difficult to reproducibly seal the polyester nanoporous membrane between the two PDMS monoliths. While exploring the materials and methods suitable for a potential replacement, we realized that the pores within a nanoporous track-etched polymeric membrane in many ways resemble those found within a hydrogel. This implies that a hydrogel plug should be able to modulate the electrokinetic transport in a similar fashion to achieve the concentration enrichment of charged analytes. In addition, these hydrogels follow simple microfabrication procedures and are perfectly suited to two-dimensional microfluidic assemblies allowing greater design flexibility, thus, becoming a core element of this research.[35]

1.3 Microfabricated Hydrogel Microstructures

1.3.1 Hydrogels

Hydrogels are insoluble networks of polymer chains with water as a dispersion medium. These cross-linked polymeric networks can absorb large amount of water and are susceptible to swelling. The cross-linking can take place in two ways, chemical or physical cross-linking. Chemical cross-linking results from covalent bonding and is permanent, while physical cross-linking can be a combination of entanglements, weak van der Waals interactions or hydrogel bonding and is reversible. The cross-linking can be controlled depending upon various factors to obtain a microporous or nanoporous architecture. These hydrogels can be simply uncharged or made electrostatically active by introducing ionizable functional groups on their backbone.[36, 37]

The ability of hydrogels to hold large percentage of water, their elastic nature and good biocompatibility gives them a structure similar to natural tissues. Hydrogels are also permeable to the essential components of living systems such as oxygen, nutrients and metabolic wastes making them a promising candidate for various biomedical and bioengineering applications.[38, 39] In addition, the photopolymerized hydrogels offer the advantage of *in-situ* fabrication thus targeting specific tissues. These hydrogels have been used in localized drug delivery systems for regulated release of proteins. Tissue-adherent hydrogels have been employed as barriers against thrombosis and restenosis to reduce postoperative cell adhesions and thickening of the arterial intima.[38, 40, 41] The chemical and mechanical stability of the hydrogels makes them usable as cell entrapment scaffolds for the reconstruction and regeneration of soft tissues, for example, cartilage regeneration,[42] vascular cell growth[43] etc. The hydrogels can host molecules responsive to local environments and hence have been employed in a wide range of biosensing applications such as detection of glucose and urea based on an array of hydrogel-entrapped enzymes,[44, 45] functional cell-based assay using 3D collagen hydrogels,[46] monitoring of cell populations using hydrogel bacterial microchip, [47] and agarose hydrogel based immunosensing for ferritin – a key element of iron metabolism in organisms.[48] These hydrogels can even produce extremely soft but durable structures ideal for the use as a contact lens material[36] and have become an integral part of human life.

1.3.2 Physiochemical Properties of Hydrogels

Swelling Behavior. The water-absorbing capacity of a hydrogel and the corresponding swelling behavior is a thermodynamic phenomenon, which plays a key role in determining the permeability of the gel for different species. In general, this swelling behavior can be described in three parts.[37] First, the water in contact with the polymerized gel network will ionize and hydrate the hydrophilic, polar groups of the gel. After this initial swelling, the water molecules will be utilized for hydrophobic interactions within the gel inducing further swelling of the gel. Finally, some additional water will enter the gel network by osmotic pressure. However, the osmotic swelling induces a counterbalancing force due to the elasticity of polymeric cross-links eventually leading to an equilibrium swelling condition. This equilibrium swelling response of hydrogels to their environment can be affected by different factors such as pH, ionic strength, temperature or electric field.[36, 49]

Effect of pH and ionic strength on equilibrium swelling

In hydrogels carrying anionic or cationic functional groups on their backbone, swelling is mainly due to the ionization of these charged groups and the osmotic pressure developed due to the differences in the ionic concentrations between the gel and its surroundings. The pH and ionic strength of the solution determine the ionic composition of the surroundings, therefore affecting the equilibrium swelling behavior.[49] For anionic hydrogels, at a pH less than the gel pK_a, the functional groups (e.g., -COOH, $-SO_3H$) fail to ionize resulting in only a small degree of swelling, which is almost independent of the ionic strength of the solution. With increase in pH above the pK_a

value, the ionization of anionic groups drives the swelling to a greater extent eventually restricted by the retraction force of the polymer cross-links. At a fixed pH, the degree of swelling can be increased by lowering the ionic strength of the solution. On the other hand, cationic hydrogels (e.g., -NH_2 functional group) show a converse behavior. Swelling is observed with a decrease in pH below the pK_b values.[49, 50]

Hydrogel Permeability and Donnan Exclusion. The porous structure in a polymerized hydrogel is basically due to the diffusion pathways available in a 3D mesh formed after cross-linking. The pore size, also called as the mesh size, in such polymeric structures is dictated by their composition (% cross-linker, % solvent, presence of co-monomer) as well as the environment (for example, pH dependent swelling).[36, 37] The permeation of a solute in the hydrogel porous structure depends on the solute geometry and its chemical interaction with the gel. In general, the permeability (P_i) of a solute 'i' in a gel is expressed as,

$$P_i = K_i D_{i,gel} \tag{1.1}$$

where $$K_i = \frac{C_{i,gel}}{C_i} \text{ at equilibrium} \tag{1.2}$$

K_i is gel partition coefficient for the particular solute, $D_{i,gel}$ is the diffusivity of the solute in the gel calculated by multiplying the diffusivity (D_i) of the solute in the solution with a ratio of gel porosity and tortuosity.[37]

The presence of fixed charges on hydrogel backbone also influences the permeation of solute ions. The gel strongly attracts counterions to its interior creating a chemical potential difference with respect to the surrounding solution phase.

Consequently, coionic species are selectively excluded from the hydrogel interior. This is called as the Donnan exclusion. The system is thermodynamically driven to achieve the electroneutrality condition at the equilibrium termed as Donnan equilibrium. The electroneutrality condition holds in both the hydrogel and solution phases. Effectively, Donnan exclusion of coions is contributed by the condition of electroneutrality on top of the electrostatic repulsion. This exclusion effect is more pronounced with higher % of fixed charges on the hydrogel, smaller pore size and greater valence of the solute coions.[37, 49]

Mechanical Properties of Hydrogels. As described previously, the polymerized hydrogel networks have been used in a vast number of applications, most of which are related to the biomedical and bioengineering field. Correspondingly, one can find many studies focused towards the functional characteristics such as responsive behavior and biocompatibility of the hydrogels. However, while employing these hydrogels in fluidic manipulations inside miniaturized architectures, it becomes necessary to gain information about their mechanical properties. The hydrogels should be able to withstand high pressures resulting from the moderate flow rates in the microchannels.[51] This could determined by carrying out tensile strength studies and measuring the Young's modulus (modulus of elasticity, G), given by,

$$G = \frac{(tensile)stress}{(tensile)strain} = \frac{\sigma}{\Delta l / l_0} \tag{1.3}$$

and the ultimate tensile strength (σ_U) defined as the maximum stress a material can withstand.[51, 52] The tensile properties of a hydrogel vary with the degree of equilibrium

swelling and hence are affected by factors such as pH, the extent of cross-linking, amount of solvent. Presence of solvent in the hydrogel precursor can lead to a higher degree of swelling, thus lowering the modulus of elasticity.[49] Nevertheless, a detailed knowledge of the mechanical properties and their interrelation with different factors essentially helps in choosing an appropriate hydrogel for a particular microfluidic application.

1.3.3 HEMA Hydrogels

HEMA hydrogels are formulated with poly(2-hydroxyethyl methacrylate) [HEMA] as a monomer. Their first application, which dates as back to the 1960s, was in the development of contact lenses and synthetic arteries.[53] HEMA hydrogels represent a typical example of hydrogels having a high water-absorbing capacity. Additionally, these hydrophilic gels have a very good biocompatibility and can be easily fabricated *in situ* inside microfluidic channels. Over the years, HEMA has been complexed with different polymeric components, poly(vinyl alcohol) [VA] and poly-HEMA as artificial skin, poly-HEMA and methacrylic acid [MAA] commonly as a contact lens material, poly-HEMA and poly(ethylene terephthlate) [PTFE] as artificial tendons and numerous others, depending upon the end application especially in the medical field.[36, 54] Further, Beebe and co-workers[54] utilized HEMA hydrogels complexed with acrylic acid [AA] or 2-(dimehylamino)ethyl methacylate (DMAEMA) as valves for autonomous flow control inside microfluidic channels highlighting the good mechanical properties of these hydrogels and thus made them a primary candidate for our preconcentration studies.

Two types of highly cross-linked HEMA hydrogel were under consideration: one, neutral hydrogel with HEMA as the only monomer and the other, anionic hydrogel in which HEMA was copolymerized with AA (HEMA-co-AA). The latter carrying fixed carboxylic acid groups (-COOH) on its backbone is a pH-responsive hydrogel and has a tendency to swell in basic buffer environments. Upon contact, H^+ is released due to the ionization of the acidic groups. This H^+ combines with OH^- from the solution allowing the influx of solution cations for charge compensation, which creates an osmotic pressure against the elasticity of the polymer network driving hydrogel swelling.[49, 50] The maximum hydrogel expansion in a microfluidic channel can be allowed only in longitudinal direction as the channel walls restrict the transverse swelling. The neutral HEMA hydrogel is subject to comparatively less swelling under similar conditions. This swelling is a consequence of the free energy of polymer-buffer mixing opposing the elastic restoring force of the network.[49] Interestingly, the swelling will be advantageous to our study as it will ensure that the hydrogel completely fills the space in the channel without allowing any leak path between the gel and the channel walls.

The tensile properties of HEMA-co-AA were studied by Johnson *et al.*[51] Completely hydrated HEMA hydrogels at a fixed pH were observed to obey Hooke's law, a linear relationship between the stress and strain yielding a constant modulus of elasticity (G). However, with increase in pH, the corresponding swelling caused a drop in σ_U values (Figure 1.2(a)). By preparing HEMA hydrogels with increasing percentage (0.2 to 20 wt.%) of the cross-linker ethylene glycol dimethacrylate [EGDMA], more rigid hydrogel structures were obtained. The loss of elasticity resulted in higher values of

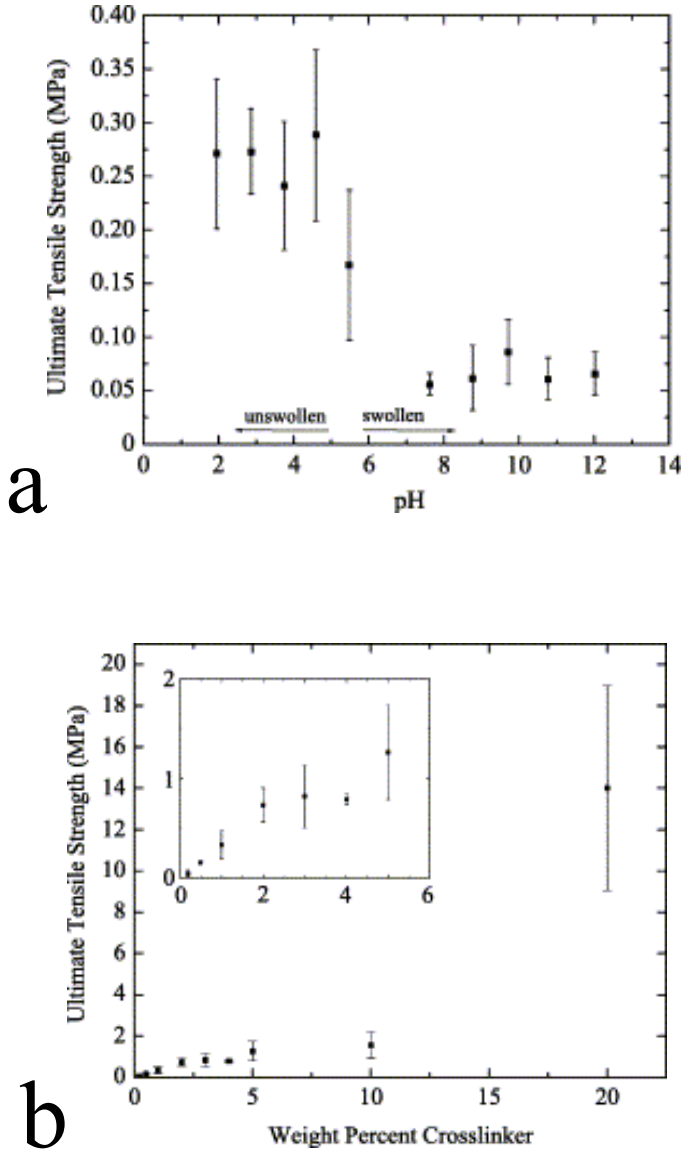

Figure 1.2. Ultimate tensile strength (σ_U) of HEMA hydrogel as a function of (a) pH, and (b) wt% cross-linker. (Reprinted with permission from Johnson et al.[51] Copyright © 2004 by Elsevier.)

σ_U (Figure 1.2(b)). In addition, the authors reported the effect of UV photopolymerization time on the mechanical properties of the hydrogel. The modulus of elasticity was observed to increase by increasing the polymerization time from 1 to 4 min. Further increase in the polymerization time (6 to 10 min) resulted in a decrease in the modulus of elasticity. This decrease was attributed to the breaking of cross-links due to the presence of oxygen radicals formed as a consequence of oxygen to ozone conversion at extended UV exposures. Based upon these findings, UV photopolymerized HEMA hydrogels with 3-10 wt% of cross-linker EGDMA were believed to serve as an excellent choice as a rigid nanoporous membranes in the microfluidic preconcentration studies.

1.4 Electro-hydro-dynamics in Miniaturized Systems

Miniaturization of chemical and bioanalytical systems to micro and nano scale offers many physical advantages, however, it gives rise to a completely different set of fluid dynamics conditions. The principles of flow dynamics at macro-scale are no longer applicable to micro- or nano-scale. At macro-scale, the volumetric forces (body forces) dictate the flow dynamics; while at miniaturized scale, the surface forces become important. [55] As a simple example, the surface to volume ratios obtained at micro-scale could be million times greater than that at macro-scale.[56] A detailed description of such changes in the fluid dynamics is followed.

1.4.1 Microchannels

Pressure Driven Flow (PDF). In general, pressure driven flow in a conduit is described by a dimensionless quantity Reynolds number (N_{Re}),[57, 58] which is a ratio of viscous forces to the inertial forces, given by

$$N_{\mathrm{Re}} = \frac{d\bar{v}\rho}{\eta} \tag{1.4}$$

where d is the diameter of the conduit, $\bar{v}$ is the flow velocity, ρ is the liquid density and η is the viscosity. The microchannels are characterized by a low N_{Re} indicating essentially laminar flow behavior. That means the fluid flows in the form of streamlines along the channel and mixing in the lateral direction can be achieved via diffusion only. Applying a non-slip condition ($\bar{v} = 0$) at the microchannel walls, the PDF can be described by Hagen-Poiseuille equation,[55, 57, 58]

$$\Delta p = \frac{32\Delta L\bar{v}\eta}{d^2} \tag{1.5}$$

where Δp is the pressure drop over a length of ΔL . The velocity profile for PDF is thus parabolic. Equation (1.5) also suggests that for a given flow rate, microchannel flows result in a higher pressure drop, which could be detrimental to the mechanical stability of microfluidic devices. The PDF is easy to generate inside microchannels and is not affected by the chemical properties of solutions such as pH or ionic strength.[59] But, the parabolic velocity profile creates an unequal distribution of sample species across the channel leading to wide dispersion zones reducing the detection sensitivity of analytical

systems.[59, 60] These problems can be reduced by switching to electrokinetic transport means.

Electrokinetics. The basic principles of electrokinetics are described in detail by Probstein[61] and Devasenathipathy.[60] The electrokinetic phenomena can de divided into four categories:

(1) Electroosmosis, the movement of bulk liquid originating from a charged surface under the influence of an enforced electric field.

(2) Electrophoresis, the movement of charged species in a solution towards opposite electrodes under the influence of an enforced electric field.

(3) Streaming potential, the electric field developed along a charged surface due to a pressure driven flow of liquid.

(4) Sedimentation potential, the electric field developed due to the movement of charged species in a stationary liquid phase.

The streaming potential is thus a reverse of electroosmosis; while the sedimentation potential is a reverse of electrophoresis. The first two electrokinetic effects, electroosmosis and electrophoresis, are vital for the understanding of the fluidic manipulations in microchannels used in this project and have been explained below.

Theory of Electric Double Layer (EDL) and Electroosmosis

Whenever a solid surface (stationary phase) comes in contact with an electrolyte (mobile phase), the fixed surface charges drive the reorganization of mobile ions in the vicinity. The charged surface attracts the counterions or the ions in the mobile phase carrying an opposite charge while the coions are pushed away. This leads to a surplus of

counterions in a region termed as an 'electric double layer' (EDL) near the charged surface. In the classical Gouy-Chapman model, the ions were considered as point charges capable of approaching the surface within infinitesimal distance. However, the ions have finite size and are hydrated in the mobile phase. From a realistic point of view, they can only approach the surface within a distance limited by their hydrated radius. This modification to the Gouy-Chapman theory is known as the Stern modification.[57] Accordingly, the EDL layer is comprised of two layers (see Figure 1.3(a)), a layer of immobile counterions adsorbed on the surface called as the 'Stern layer' and an outer layer of diffused mobile counterions called as the 'Gouy-Chapman diffuse layer' or simply the 'diffuse layer'. The hydrated ions in the diffuse layer can flow past the Stern layer at an arbitrary plane called the 'shear plane'.[60, 61] Due to the Stern layer, the potential at this plane is much lower in magnitude and is called the 'zeta potential' (ζ). Applying a statistical mechanics approach, the diffuse layer is considered as a series of energy states with equivalent degeneracies in thermal equilibrium to obtain a potential (ϕ) profile as shown in Figure 1.3(b).

The numbers of species in any two energy states are related by a Boltzmann factor. Hence, the concentration distribution for ionic species 'i' ($C_i(y)$) in the diffuse layer can be given in terms of the bulk concentration ($C_{i,bulk}$) as,[60-62]

$$C_i(y) = C_{i,bulk} \exp\left(-\frac{z_i e \phi(y)}{k_B T}\right) \tag{1.6}$$

where z_i is the ionic charge number, e is the charge on an electron, k_B is the Boltzmann constant and T is the solution temperature. The total charge density (ρ_E) is then the sum

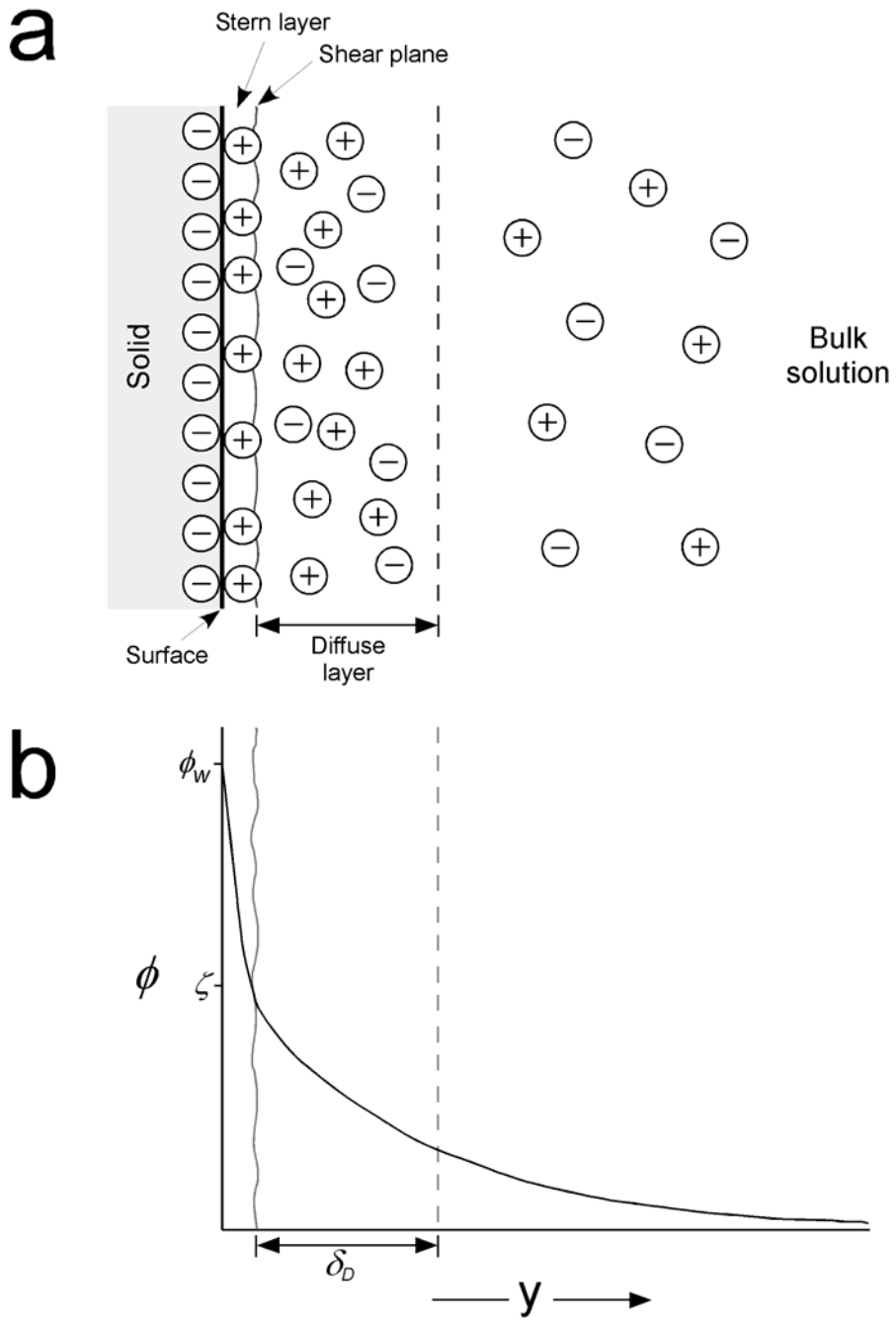

Figure 1.3. (a) EDL structure. (b) Potential profile across the EDL. (adapted with permission from Shaw.[63] Copyright © 1980 by Elsevier.)

of the ionic charges per unit volumes in all the energy states.[60-62]

$$\rho_E = F\sum_i z_i C_i(y) \tag{1.7}$$

where F is the Faraday constant.

From electrostatics, the Poisson equation can be written as,[60-62]

$$\frac{d^2\phi}{dy^2} = -\frac{\rho_E}{\varepsilon} \tag{1.8}$$

where ε is the permittivity of the medium.

Substituting equation (1.7) into equation (1.8) and simplifying for a system of symmetric electrolyte (with charge magnitude z),[60, 61]

$$\frac{d^2\phi}{dy^2} = \frac{2FzC_{bulk}}{\varepsilon}\sinh\left(\frac{ze\phi(y)}{k_BT}\right) \tag{1.9}$$

Rearranging equation (1.9) and integrating over the diffuse layer with boundary conditions:

$$\phi(y) = \phi_w \qquad \text{at } y = 0 \text{ (at the shear plane)}$$

$$\text{and} \qquad \phi(y) = \phi \qquad \text{at } y = y$$

we obtain a general expression for the potential profile in the diffuse layer,[62]

$$\frac{\tanh\left(\frac{ze\phi}{4k_BT}\right)}{\tanh\left(\frac{ze\phi_w}{4k_BT}\right)} = \exp\left(-y/\delta_D\right) \tag{1.10}$$

where

$$\delta_D = \left(\frac{\varepsilon RT}{2F^2z^2C_{bulk}}\right)^{1/2} \tag{1.11}$$

δ_D is the thickness of the EDL, commonly known as the Debye length. At large ϕ_w, the surface is highly charged implying a compact diffuse layer characterized by a sharp drop in the potential across the EDL. For small values of ϕ_w, that is, $zF\phi << RT$ (Debye-Hückel approximation), equation (1.10) reduces to

$$\phi = \phi_w \exp\left(- y / \delta_D \right) \tag{1.12}$$

indicating an exponential drop in the potential across the diffuse layer.[61, 62]

The microfluidic devices used in this project are hybrid PDMS (polydimethyl siloxane) /glass fabricated using rapid prototyping technique.[64] Both PDMS and glass microchannel walls constitute negative surface charges upon contact with aqueous solution. As a result, there is an excess of positively charged ions in the EDL. If an electric field is applied along the surface as shown in Figure 1.4, the mobile positive ions in the diffuse layer are set in motion towards the cathode. These ions also drag water molecules along with due to viscous resistance leading to a net flow of the bulk liquid, from anode to cathode, called the electroosmotic flow (EOF).

Estimation of the electroosmotic velocity ($\overline{v}_{eo}$)

Consider an incompressible, Newtonian liquid subjected to an external electric field ($\overline{E}$) in a microchannel of uniform cross-section (Figure 1.4). In the absence of pressure gradients and neglecting the gravitational effects, the basic momentum balance equation can be written as,[57, 61]

$$\eta \nabla^2 \overline{v}_{eo} = - f_E = - \rho_E \overline{E} \tag{1.13}$$

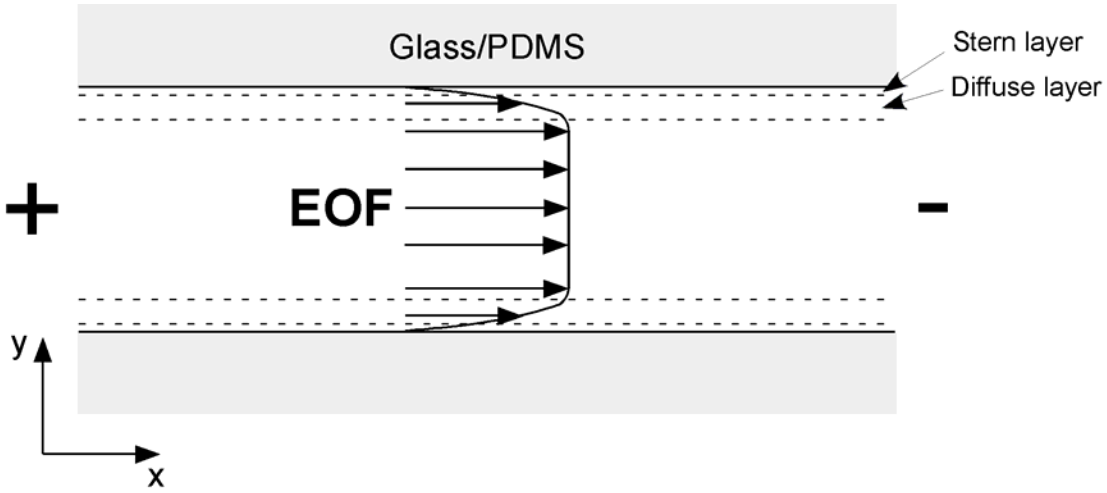

Figure 1.4. Schematic of electroosmotic flow.

where η is the liquid viscosity and f_E is the Lorentz body force. Introducing Poisson equation (1.8) into above equation and solving for a two-dimensional (2D) x-y system (x: along and y: normal to the channel axis), we obtain

$$\overline{v}_{eo}(y) = -\frac{\varepsilon \overline{E} \zeta}{\eta}\left[1 - \frac{\phi(y)}{\zeta}\right] \tag{1.14}$$

In case of a thin EDL (small δ_D) compared to the microchannel dimensions, $\phi(y) \approx 0$ over the entire cross-section of the microchannel simplifying equation (1.14) to

$$v_{eo} = -\frac{\varepsilon E \zeta}{\eta} = -\mu_{eo} E \tag{1.15}$$

This equation is known as the Helmholtz-Smoluchowski equation and is applicable to most microfluidic systems as the channel dimensions are usually four orders of magnitude greater than δ_D.[61] The equation suggests a 'plug flow' profile for the EOF. This property of the microchannel EOF is of utmost importance as it ensures a uniform distribution of sample species across the channel with minimal dispersion zone widening improving the detection sensitivity of analytical systems. μ_{eo} is called the electroosmotic mobility and is a characteristic of a particular channel surface - solution combination.

For microfluidic systems with simultaneous pressure driven and electroosmotic flows, solutions obtained for the velocity field for different cross-sectional geometries can be found in literature. Burgreen and Nakache[65] have presented an elegant solution for the electrokinetic flow in very fine slits with small values of microchannel dimension to the Debye length ratio. Rice and Whitehead[66] applied the electrokinetic theory to

evaluate the flows in a narrow cylindrical capillary. Patankar and Hu[67] have attempted the numerical simulation of electroosmotic flows in complex geometries. Herr and Santiago[68] have studied the effect of step changes in zeta potential (ζ), the parameter which leads to the electroosmotic flow, on electroosmotic flow in cylindrical channels. Brotherton and Davis[69] have analyzed the effect of step changes in ζ and channel cross-section on the electroosmotic flow in channels of arbitrary cross-section. In addition, a detailed summary on zeta potential of different microfluidic substrates and factors affecting its value has been presented by Kirby and Hasselbrink.[70, 71]

In a channel, the volumetric flow rate of a liquid due to pressure driven flow is proportional to the fourth power of its characteristic dimensions while the electroosmotic flow rate to the second power. This implies that as the channel dimensions go down, electroosmotic flow becomes prominent, typically when the channel dimensions are of the order of the Debye length.[61]

Electrophoresis

When an electric field is applied to an ionic solution, the cations and anions move towards the opposite electrode cathode and anode, respectively. This charge dependent migration of ions is called 'electrophoresis' (EP). This movement due to the electric field is countered by a frictional drag.

Electrostatic force: $\bar{f}_e = q\bar{E}$ (1.16)

Frictional drag: $\bar{f}_f = 6\pi\eta r\bar{v}_{ep}$ (1.17)

where q is the ionic charge, $\overline{E}$ is the external electric field, r is the ionic radius and $\overline{v}_{ep}$ is the electrophoretic velocity of the ion.

By balancing the two forces, we can obtain an expression for the electrophoretic velocity of an ion as,

$$\overline{v}_{ep} = \mu_{ep}\overline{E} \tag{1.18}$$

where $$\mu_{ep} = \frac{q}{6\pi\eta r} \tag{1.19}$$

μ_{ep} is the electrophoretic mobility of the ion. It is a characteristic property of an ion in a particular solution.

In an infinitely dilute solution, the electrophoretic mobility of a charged particle can be related to its diffusivity (D) by Nernst-Einstein equation,[61]

$$D = \mu_{ep}RT \tag{1.20}$$

Migration of charged species under applied electric field. Consider a dilute ionic solution under the influence of an external electric field. The charged species in the solution are thus subjected to three transport processes: (i) electrophoretic migration, (ii) diffusion defined by Fick's law, and (iii) convection, which includes a combined effect of external pressure gradients, electroosmotic flow generated due to the surface EDL, and flow due to thermal gradients resulted from Joule heating.[72] In the absence of external pressure gradients and the Joule heating, one can write the molar flux equation for a charged species 'i' in the solution as,

$$J_i = -\mu_{ep,i} z_i F C_i \nabla\phi - D_i \nabla C_i + C_i \nu_{eo} \tag{1.21}$$

This equation is called as the Nernst-Planck equation[61] and used in general for describing the electrokinetic migration of charged species.

1.4.2 Nanochannels

As mentioned earlier, the reduction in channel dimensions from macro to micro leads to the prominence of electroosmotic flow over pressure driven flow. If the channel dimensions are reduced even further to nano-scale, it becomes almost impossible to force the liquid through the channels by reasonable pressure gradients and hence the effects of PDF can be neglected. On the other hand, as the characteristic channel dimension (a) approaches the Debye length, there is a possibility of overlap of the EDL originating from the opposite walls of the channel. Unlike the microchannel cases where $a >> \delta_D$, the approximation of plug flow profile is no longer applicable as the EOF assumes Poiseuille form.[66] The magnitude of this EOF is affected by the degree of EDL overlap. Greater degrees of EDL overlap result in the reduction of the EOF. For $a = \delta_D$, the EOF velocity could be as low as 20% of the maximum possible EOF velocity (at $a >> \delta_D$).[66] Yet it could have a significant effect on the transport phenomena inside the nanochannels and hence cannot be neglected.[73]

The nanoscale geometries also give rise to Donnan exclusion effects. Due to the excess of counterions in the EDL, coions are selectively excluded from entering the nanochannels. In fact, this behavior is critically important in the application of charged nanochannel membranes as ion exchange membrane. Rubinstein and coworkers have studied ion-exchange membranes used in electrodialysis and put forth theories of electric

field distribution and electrokinetic instabilities around the membrane.[74-76] Tallarek's group has applied these ideas for explaining concentration polarization (CP) and nonequilibrium electrokinetic effects in porous ion-permselective glass particles packed in a capillary.[77-79] The studies included the analysis of loading and unloading characteristics of different tracers (neutral, counterionic, and coionic) in a glass capillary (300 μm square cross-section) packed with ~2 mm long bed of spherical glass beads with mean diameter of 175 μm. The glass beads contained a porous structure (average pore diameter of 20 nm) called the mesopore region surrounded by inter-particle voids called the macropore region.

To elaborate the basics of Tallarek's studies, consider a single mesopore in contact with the macroporous space as shown in Figure 1.5. In aqueous solution, the glass surface assumes a negative charge and leads to the formation of (primary) EDL. If the mesopore size is of the order of the EDL thickness (the Debye length, δ_D), there is a strong EDL overlap which results in an excess of counterions (cations) and selective exclusion of coions (anions) inside the mesopore. In the absence of an external chemical or electric potential gradient, a Donnan equilibrium is established between the meso and macroporous regions (Figure 1.5(a)). Upon application of the external electric field (Figure 1.5(b)), the mesopore acts as a cation-exchange membrane allowing preferential permeation of the cations. As a result, concentration polarization (CP) zones are developed at the anodic and cathodic interfaces of the mesopore. The anodic interface is characterized by depletion of ions (The concentration depletion zone is defined by the diffusion boundary layer (DBL) as shown in Figure 1.5(b).) while there is an enrichment

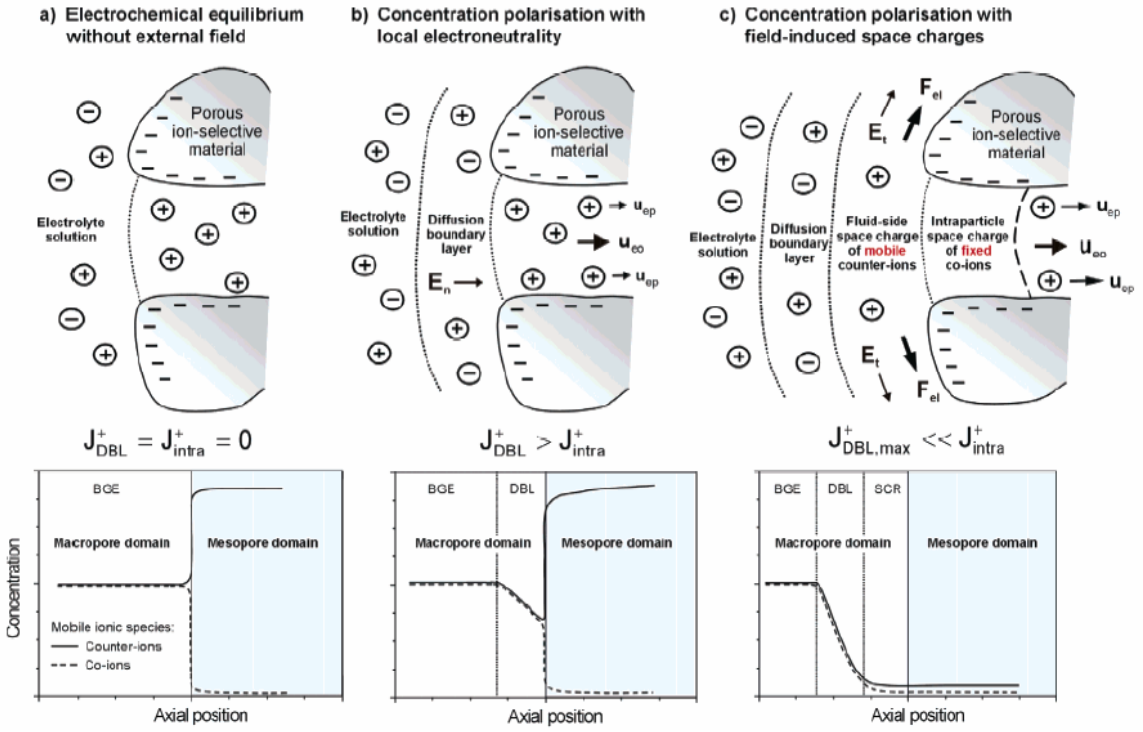

Figure 1.5. The basics of concentration polarization (CP) and nonequilibrium electrokinetic effects. (Reprinted with permission from Leinweber et al.[77] Copyright © 2004 by the American Chemical Society.)

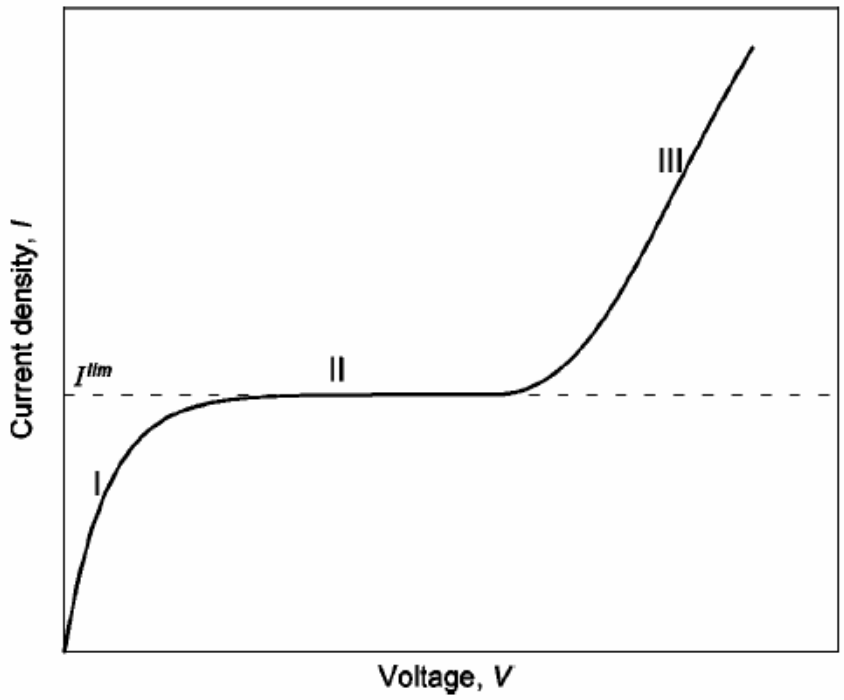

Figure 1.6. Typical current-voltage relationship for a cation-exchange membrane. (Reprinted with permission from Rubinstein et al.[76] Copyright © 2000 by the American Physical Society.)

of ions at the cathodic interface. Due to the depletion of ions in the DBL, the corresponding ionic flux becomes diffusion limited. However, the current through the pore remains Ohmic at low electric fields (region I in Figure 1.6) and the condition of electroneutrality is obeyed locally. By increasing the electric field, the concentration of ions in the DBL is virtually reduced to zero. The DBL offers maximum diffusional resistance to the transport of ions. The additional electric field is then dropped across this depleted DBL rather than the entire system and the current reaches a limiting value (limiting current density, $I^{\lim}$) (region II in Figure 1.6). The electric field at which this deviation from linearity takes place is called the critical electric field, E_{crit}. A further increase in the applied electric field results in a normal component of the applied electric field and generates a nonequilibrium space charge region of fixed surface charges of the mesopore and mobile cations in the macropore at the anodic interface as shown in Figure 1.5(c). This space charge region is called the secondary or nonequilibrium EDL and leads to the secondary electroosmotic fluctuations at the anodic interface. These nonequilibrium convective flows destroy the depleted DBL allowing overlimiting currents ($I > I^{\lim}$) through the mesopore (region III in Figure 1.6). With the help of confocal laser scanning microscopy, Tallarek and coworkers were able to investigate in detail electro-hydrodynamics of the nonequilibrium electroosmotic flows in capillaries immobilized with porous glass beads.

Figure 1.7 describes the nonequilibrium electrokinetic effects identified by Tallarek over a single porous glass bead using three different tracers: rhodamine 6G (charge = +1, counterionic), BODIPY 493/503 (neutral) and BODIPY disulfonate

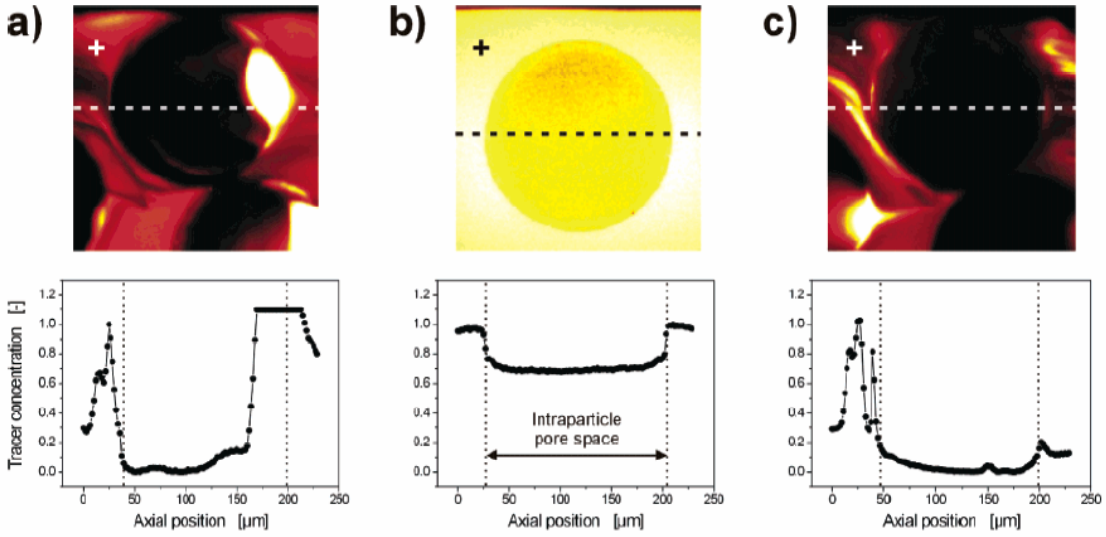

Figure 1.7. Effect of secondary EOF (at $E > E_{crit}$) on the intra-bead concentration distribution of (a) counterionic rhodamine 6G, (b) neutral BODIPY 493/503, and (c) coionic BODIPY disulfonate tracers. (Reprinted with permission from Leinweber et al.[77] Copyright © 2004 by the American Chemical Society.)

(charge = -2, coionic). With a laminar pressure driven flow (PDF) superimposed with an electric field E ($> E_{crit}$), the generation of space charge region in the bead mesopore resulted in the emptying of rhodamine 6G (Figure 1.7(a)) from the bead interior and showed strong lateral convective flow patterns in the extra-bead space indicating the existence of secondary EOF. Similar flow patterns were observed in the macropore space with BODIPY disulfonate (Figure 1.7(c)) while an experiment with uncharged BODIPY (Figure 1.7(b)) did not show any effect of the nonequilibrium electrokinetic flows on the steady-state concentration distributions in the mesopore.

In addition, a nonlinear electrokinetic behavior of simple ionic systems with hydrogel and their application as electrolyte diodes and transistors has been well examined by Marek *et al*.[80] Ion-enrichment and depletion effects in a nano-slit considering the analyte fluxes due electrophoresis in nano- and micro-channels have been reports by Liu.[81] Similar studies have been carried out by Plecis *et al*. by applying a concentration gradient across a Pyrex nanoslit in the absence of electric field.[82] Lopez and coworkers have found that by adjusting the widths of nanochannels, it is possible to achieve variation in the electrokinetic velocities of a negatively charged dye Alexa 488 and a neutral dye rhodamine B facilitating their separation.[83]

The HEMA-co-AA acid hydrogel microplug fabricated inside a microchannel in this research behaves as a cation-ion exchange membrane and has been studied in detail for the concentration polarization and the subsequent electrokinetic effects.

CHAPTER II

EXPERIMENTAL

2.1 Materials

Precursors for preparing poly(dimethylsiloxane) (PDMS, Sylgard® 184) microfluidic devices were obtained from Krayden, Inc. (Denver, CO) or K. R. Anderson, Inc. (Morgan Hill, CA). Fluorescein disodium salt (98+%, Avocado, Heysham, England), 5'-carboxyfluorescein-labeled 22-mer and 50-mer ssDNAs (IDT, Coralville, IA) and fluorescent markers such as BODIPY® 493/503 (4,4-difluoro-1,3,5,7,8-pentamethyl-4-bora-3a,4a-diaza-s-indacence), BODIPY® 492/515 disulfonate (4,4-difluoro-1,3,5,7,8-pentamethyl-4-bora-3a,4a-diaza-s-indacence-2,6-disulfonic acid, disodium salt) and bovine serum albumin tagged with Alexa Fluor® 488 from Molecular Probes, Inc. (Eugene, OR) were used in the electrokinetic concentration enrichment studies. TRIS base and its hydrochloride salt (TRIZMA brand), acrylic acid (AA), 2-hydroxyethyl methacrylate (HEMA), ethylene glycol dimethacrylate (EGDMA), and 2,2-dimethoxy-2-phenyl-acetophenone (Irgacure 651) were received from Sigma-Aldrich, St. Louis, MO. All buffer solutions contained 5.0 mM TRIS and 5.0 mM TRIS•HCl (pH 8.1-8.3) and were prepared with deionized water (18 MΩ•cm, Milli-Q® Gradient System, Millipore) unless and otherwise mentioned.

Cover glass (25 mm × 25 mm or 24 mm × 60 mm, No. 1, 0.13 – 0.17 mm thick) used for the fabrication of PDMS/glass hybrid microfluidic device was obtained from VWR Scientific.

2.2 Techniques

2.2.1 Photolithography

The word ‘lithography’, originated from ancient Greek word ‘lithos’ (i.e. stone), means a technique of transferring a pattern onto a smooth surface and was invented by Alois Senefelder in late 1790s. The pattern transfer process carried out using optical means is referred to as ‘photolithography’ – most commonly used lithographic technique. The basic steps of photolithography include transferring a printed photomask design onto a photoresist layer (on a substrate) by exposure to ultraviolet (UV) light or laser, followed by an etching or deposition step to transfer the subsequent photoresist pattern to the substrate underneath. The advances in photolithographic techniques have imparted the capability of creating extremely small features onto substrates and thus rendered an immense importance in the area of MicroElectroMechanical Systems (MEMS).[84-86] However, the photolithography may not always serve as the best approach for various microfabrication applications. These techniques are inherently expensive requiring clean-room facilities. They are not suitable for creating three-dimensional (3D) patterns. The surface chemistries of substrates cannot be controlled by photolithography, plus, the number of photoresists that could be used for these techniques is limited. Recently developed soft lithographic techniques serve as a promising alternative under such implications.[87]

2.2.2 Soft Lithography

Soft lithography is a microfabrication technique in which patterns are physically transferred to a substrate through self assembly or replica molding. The technique uses a rigid master such as a mold or stamp for imprinting a pattern on elastomeric substrates, for example, polymethylmethacrylate (PMMA), poly(dimethylsiloxane) (PDMS), polyimides, polyurethanes etc. Soft lithographic techniques are inexpensive. They can be applied to a wide range of materials as well as offer the advantage of controlling the surface chemistries. They allow the development of non-planar structures and can be used for structural features as small as 30 nm. Most importantly, the simple nature of soft lithography allows for rapid prototyping of the structures. All the steps starting from the design to the final micro- or nano-fabricated structure can be completed within 12 hours.[84, 87]

Different soft lithography techniques include replica molding, micro-contact printing, micro-transfer molding, micromolding in capillaries and solvent-assisted micromolding.[84, 87] For the course of this project, replica molding was the most suitable and used in conjunction with PDMS elastomer.

Fabrication of Masters for PDMS Replica Molding. Precleaned glass microscope slides were used as substrate for the fabrication of masters. The procedure included following steps (see Figure 2.1) performed in a cleanroom.

1. Spin coating: a thin uniform layer of positive photoresist P4620 was spin coated on a clean glass slide (25 mm × 25 mm × 1 mm) at a speed of 1300 rpm for 1 min.
2. Soft baking: The slide was then soft baked on a hotplate at 90^0C for 2 min. to

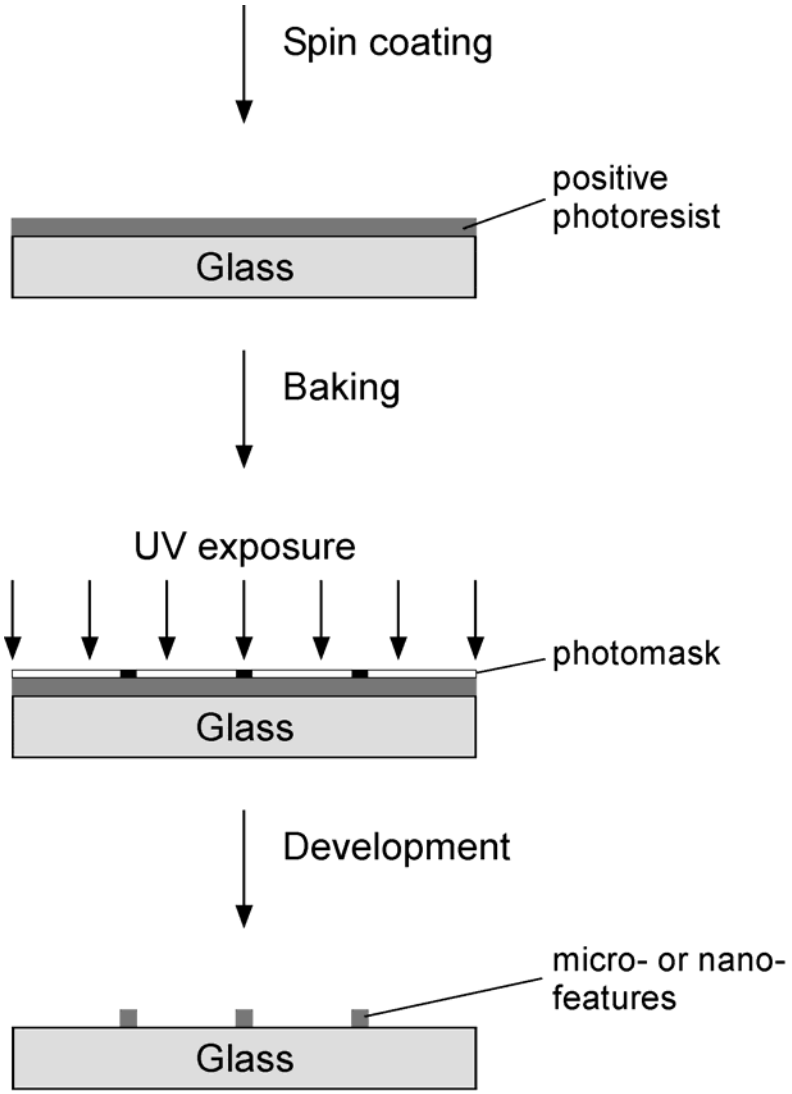

Figure 2.1. Fabrication of masters for replica molding.

solidify and facilitate the adhesion of the photoresist to the glass slide.

3. Hard baking: Soft baking was followed by hard baking at 110^0C for 3 min. to enhance the rigidity of the photoresist layer.
4. Steps 1 to 3 result in a ~ 10 μm thick photoresist layer. However, the required thickness for microchannel structural features was about 20-25 μm. Hence, steps 1 to 3 were repeated to double the thickness of the photoresist layer.
5. UV exposure: The photoresist layer was exposed to UV light (365 nm) through a photomask incorporating the microchannel design for 90 s using a mask aligner (Quintel Q4000 MA, Morgan Hill, CA). The light exposure increases the solubility of the exposed positive photoresist.
6. Development: The development process dissolves the UV exposed photoresist leaving behind photoresist features equivalent to the microchannel design on the photomask. This step was carried out using the potassium based AZ 421K developer (Clariant Corp., Somerville, NJ)) for a development time of 2 min. followed by rinsing with deionized water and drying under N_2.

The thickness of microchannel features on the resultant glass masters was measured using Dektak 3 stylus profilometer (Veeco, Woodbury, NY). The measured thickness was ~ 20 μm.

Before using these glass masters for PDMS replica molding, the masters were silanized by exposing to the vapors of (tridecafluoro-1,1,2,2-tetrahydrooctyl)-1-trichlorosilane for 20 min. The silanization step passivates the surface allowing easy release of PDMS elastomer from the master without damaging the master. Such

silanized glass masters can be used for more than 50 PDMS replications.[87]

PDMS Replica Molding. We prefer PDMS elastomer for replica molding as it offers many features necessary for the preconcentration studies of this project. Its optical transparency down to ~300 nm makes it a very good candidate for carrying out microscopic fluorescence detection studies. PDMS is capable of making a conformal contact with surface features on the sub-micron scale. It has a decent chemical stability, thus can be used with a variety of chemical species. PDMS is also stable thermally up to 186^0C in air and its surface properties can be altered easily according to specific requirements. At the same time, PDMS can raise some concerns. It is liable swelling to following interaction with nonpolar organic solvent hexane. It also shows marginal shrinking (~1%) during curing. The elastomer is soft in nature limiting the aspect ratio (thickness to width ratio of the molded features) from 0.2 to 2.0 for features without deformation.[87] Nevertheless, it was difficult to overlook the advantages of using PDMS elastomer and was chosen for the studies.

The schematic of PDMS replica molding is shown in Figure 2.2. The Sylgard® 184 silicone elastomer kit consisting of a polymeric base and a curing agent was used for making PDMS precursor. Typically, the base was thoroughly mixed with the curing agent in a proportion 10:1 by weight, degassed under vacuum and then poured over the master in a plastic petri-dish. The mixture was cured in a gravity oven at ~70^0C for 2 hours. The heat treatment accelerates the cross-linking (hydrosilation) between vinyl ($SiCH=CH_2$) groups with hydrosilane (SiH) groups forming $Si-CH_2-CH_2-Si$ linkages and solidifies.[87, 88] The cured PDMS monolith was let cool down to room temperature and

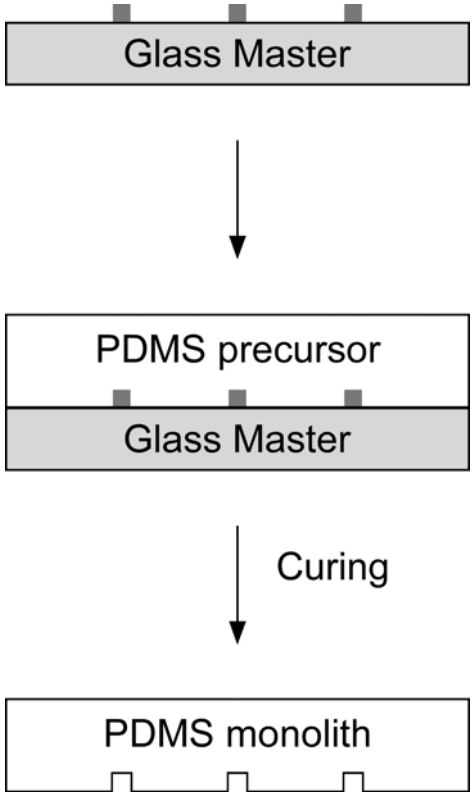

Figure 2.2. Schematic of PDMS replica molding.

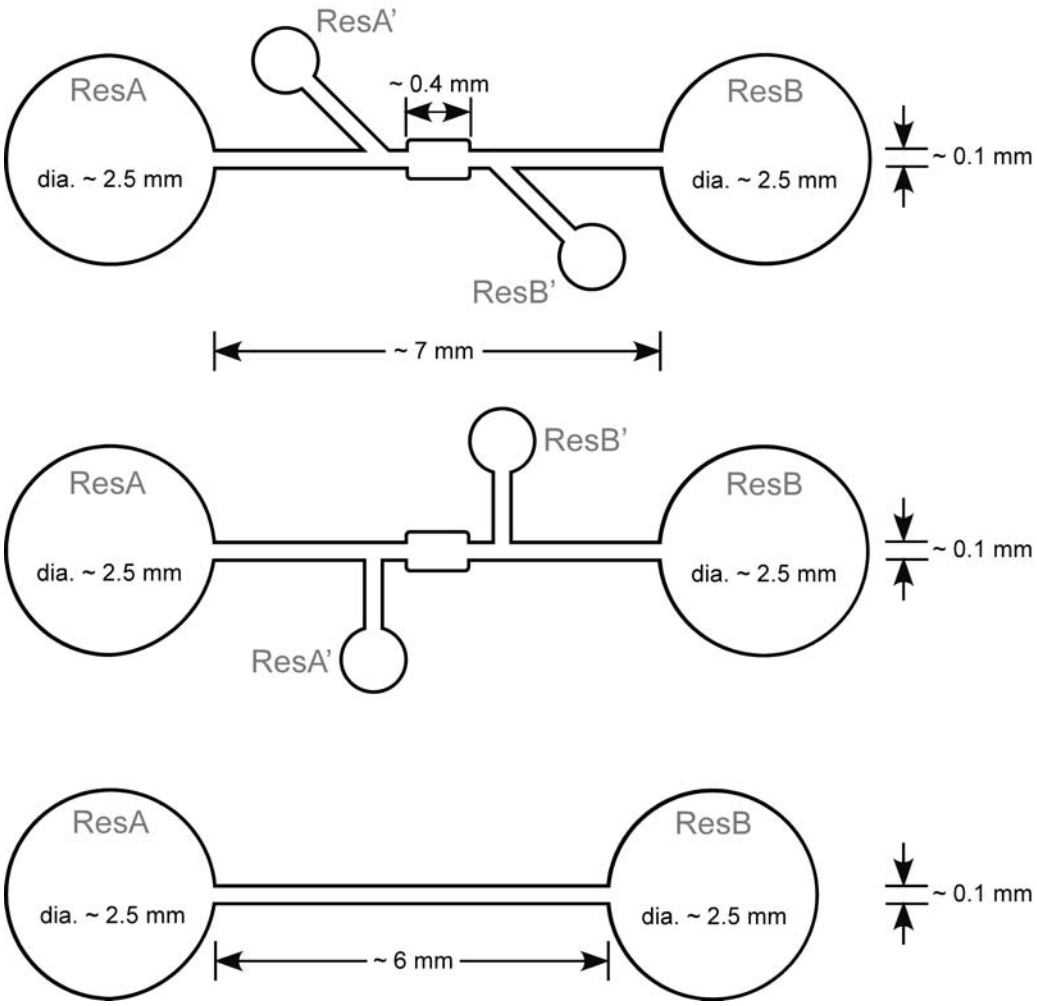

Figure 2.3. Layouts of different microfluidic channel architectures employed.

then peeled off from the glass master.

2.2.3 PDMS/Glass Hybrid Microfluidic Device

Microfluidic channels (20-25 μm in height) were fabricated following a literature procedure.[89] First, reservoirs or ports for fluidic delivery were created by punching holes into the PDMS monolith (4-6 mm thick) featuring the microchannel architecture. The monolith was then washed with ethanol and dried under a stream of N_2 gas. It was then bonded irreversibly to a pre-cleaned cover glass (25 mm × 25 mm, 0.13 – 0.17 mm thick) after both were treated with an O_2 plasma (60 W, model PDC-32G, Harrick Scientific, Ossining, NY) for 15 s. The plasma treatment of PDMS converts the –$OSi(CH_3)_2O$- groups into $–O_nSi(OH)_{4-n}$ groups.[64] This induces formation of a strong covalent Si-O-Si association between PDMS and glass substrates. The bonding was allowed for 2 min. followed by a heating step at 75^0C for 15-20 s to enhance the quality of irreversible bonding. Different layouts of the micochannels used in the experimentation are shown in Figure 2.3. All the microchannels were 90-100 μm wide unless specified otherwise. Some microchannel included a wider channel-section (190-200 μm wide and 400 μm long) designed to house a hydrogel microplug. The punched reservoirs were 2.5-3.0 mm in diameter. The liquid manipulation in these microfluidic devices was achieved using pressure driven flows (hydrostatic pressure and syringe pump) and/or electrokinetic flows.

The most important electrokinetic parameter in such PDMS/glass microchannels is the surface zeta potential, which leads to an electroosmotic flow. The zeta potential

can be expressed in terms of electroosmotic mobility as shown by equation (1.15). In an aqueous medium, the electrokinetic character of the PDMS surface can be considered close to that of glass due to the similarities between the electroosmotic mobility (μ_{eo}) values obtained in plasma oxidized PDMS/PDMS and PDMS/glass channels.[90] The electroosmotic mobility values of ~ 5×10^{-4} $cm^2/V \cdot s$ were measured in the irreversibly bonded PDMS/glass microchannels employed in this project.

The wetting characteristic of PDMS is another crucial factor. Untreated (native) PDMS surface is essentially hydrophobic with a stable contact angle of 102^0-108^0.[64, 90, 91] The high contact angles lead to difficulties in introducing aqueous solutions into the channel.[90] The O_2 plasma treatment can reduce the contact angles to 30^0 facilitating smooth manipulations of aqueous solutions.[64]

2.2.4 *In-situ* Hydrogel Microfabrication

Following the fabrication of PDMS/glass microfluidic device, hydrogel microplug was incorporated into the microchannel using UV photopolymerization technique.[54] First, a hydrogel precursor solution was introduced into the microchannel by capillary action. Next, UV light (365 nm, 200 s, 300 mW/cm^2, EFOS Lite E3000, Ontario, Canada) was projected onto the required part of the channel from the side port of a microscope (DIAPHOT 300, Nikon) through a 10x objective lens as shown in Figure 2.4. Unpolymerized precursor solution was removed by either pumping (for designs with side-channels) 10.0 mM TRIS buffer through side-channels at a flow rate of 10.0 μL/min for > 10 min using a syringe pump (Harvard Apparatus, Holliston, MA)

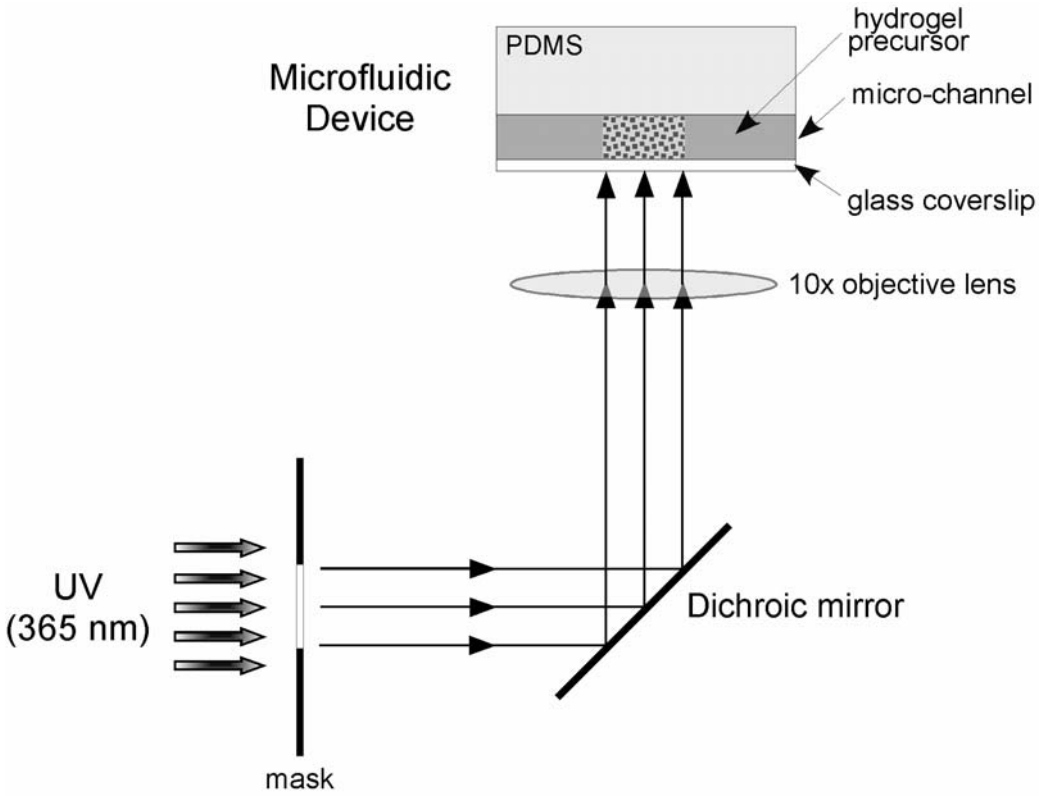

Figure 2.4. Schematic of UV photopolymerization.

or electrokinetic conditioning (for designs without side-channels) of the channel using an electrical bias ranging from 50 to 400 V.

2.2.5 Electrical Set-up for Experimentation

Figure 2.5 shows a general circuit layout for the electrokinetic preconcentration experiments. The necessary electrical bias was accomplished through a laboratory-made unit for high voltage power supply (range 0 – 1067 V) using a single output module (High Power "C" Series, Ultra Volt, Ronkonkoma, NY). The bias voltage was applied between two coil electrodes (90% Pt/10% Ir, 0.25 mm in diameter and 50.0 mm in length) immersed in two different reservoirs. A photograph of the experimental set-up is included in Figure 2.6. The voltage could be switched with a time resolution of 100 ms using a computer and custom software. Before each experiment, the microchannel was filled with 10.0 mM TRIS buffer, and then the hydrogel microplug was conditioned by applying an appropriate bias. The conditioning step removes unpolymerized precursor solution from within the hydrogel. Following the conditioning step, the reservoirs were rinsed with the TRIS buffer multiple times and a fluorescent target analyte solution prepared in the TRIS buffer was introduced in ResA or Res B or both depending upon the objectives of the particular experiment. The experiments were conducted by applying a programmed sequence of bias voltages to the electrodes.

The current through the microfluidic channel was calculated by measuring voltage drop across the external resistor R_{ext} (510 KΩ) at different time intervals and using the ohm's relation.

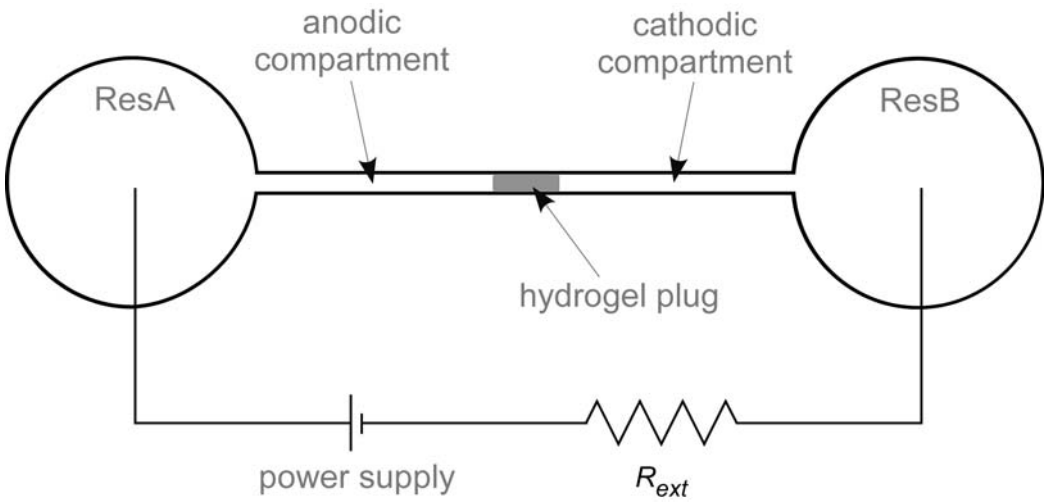

Figure 2.5. Schematic of electrical set-up for preconcentration experiment.

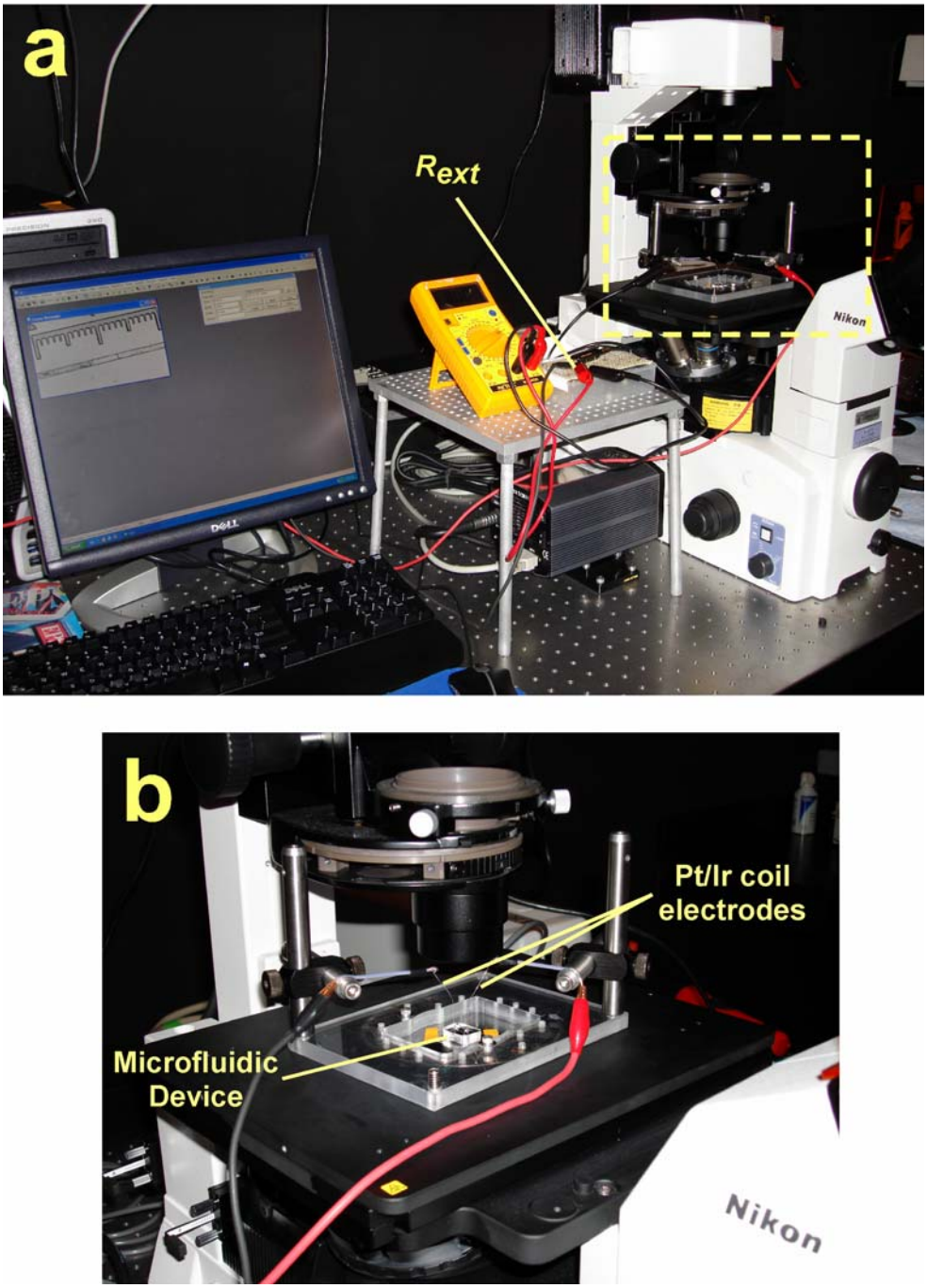

Figure 2.6. Photographs of (a) electrical set-up for a typical preconcentration experiment, and (b) the microfluidic device (inset of (a)).

2.2.6 Fluorescence Microscopy and Imaging

During each preconcentration experiment, a set of fluorescence micrographs was obtained from the region near the hydrogel/open-channel interface using the V++ microscopy imaging software (Digital Optics, New Zealand).

The initial phase experiments were captured using the inverted epifluorescence microscope TE 300 (Nikon, Japan) equipped with a CCD camera SenSys 1410E (Photometrics, Tucson, AZ). Typically, a total of 360 frames (8 × 8 binning, 163 × 128 pixels) were captured at a rate 1 s/frame (exposure time = 400 ms) through a 4x objective lens. For latter experiments, a more advanced system comprised of the inverted epifluorescence microscope Eclipse TE 2000-U (Nikon, Japan) attached with a powerful CCD camera Cascade 512B (Photometrics, Tucson, AZ) was employed. Typical capture sequence included 541 frames (1 × 1 binning, 512 × 290 pixels) at a rate 2 s/frame (exposure time = 100 ms) through a 4x objective lens. For enhanced visual quality, the images were modified to an appropriate grayscale and in some cases with a false color scheme (brightness decreasing in the order white-green-blue-black).

2.2.7 Data Analysis Procedure

The procedures for quantification of the fluorescent intensity data and determination of the concentration enrichment factors varied depending upon the objectives of the analysis.

In the initial phase experiments, to quantify the enrichment factor near the hydrogel-solution interface, the average fluorescence intensity (counts per second per

pixel) was calculated by first integrating all fluorescent photons over a particular region of interest (ROI) in the channel and then dividing the result by the total number of pixels in the ROI. The same calculation was also performed over a second ROI located within the reference channel. All average fluorescence intensity values were corrected by subtracting the background (dark count), which was obtained using a ROI outside the channel at t = 0 s. The concentration enrichment factor is then the ratio of the two corrected average fluorescence intensities obtained according to the above procedure.

In the latter experiments, the entire channel section under the microscopic view was chosen as the ROI. The width-averaged (averaged in y-direction) fluorescence intensity profile was obtained along the channel length over the entire ROI. The corresponding concentration enrichment factors were then calculated by comparing the peak heights in the fluorescence intensity profiles obtained at different times or at different voltages to the average fluorescence intensity data obtained in a channel (without hydrogel microplug) containing the original fluorescent marker solution flowing at a rate 0.1 μL/s. All fluorescence intensity values were corrected by subtracting the background count and normalized before obtaining the fluorescence intensity profiles. The effect of photobleaching was not corrected in any reported data.

The recorded currents were also plotted against time (or applied voltages if the experiment was carried out at varying applied electric field.).

A detailed explanation of the data analysis procedures is included in the succeeding chapters.

CHAPTER III

ELECTROKINETIC CONCENTRATION ENRICHMENT WITHIN A MICROFLUIDIC DEVICE USING A HYDROGEL MICROPLUG*

3.1 Synopsis

A simple and efficient approach for concentration of charged molecules in microfluidic devices is described. The functional component of the system is a hydrogel microplug photopolymerized within the main channel of a microfluidic device. When an appropriately biased voltage is applied across the hydrogel, charged analyte molecules move from the source well toward the hydrogel. Transport of the analyte through the hydrogel is slow compared to its velocity in the microfluidic channel, however, and therefore it concentrates at the hydrogel/solution interface. For an uncharged hydrogel, a bias of 100 V leads to a ~500-fold enrichment of the DNA concentration within 150 s, while the same conditions result in an enrichment of only 50-fold for fluorescein. Somewhat lower enrichment factors are observed when a negatively charged hydrogel is used. A qualitative model is proposed to account for the observed behavior.

3.2 Introduction

Here we describe a new approach for concentrating charged molecules within a microfluidic device. The key finding is that a hydrogel microplug photopolymerized within the channel is able to modulate mass transport. The chemical composition of the

* Reprinted with permission from Dhopeshwarkar, R. R.; Sun, Li; Crooks, R. M. *LabChip* **2005**, *5*, 1148-1154. Copyright © 2005 by the Royal Society of Chemistry.

hydrogel, including its charge and extent of crosslinking, determines the mechanism of concentration for a particular analyte. The trivial case occurs when the pore size of the hydrogel is smaller than the cross-sectional area of the analyte; then the hydrogel acts as a simple size-exclusion filter (we do not consider that case here).[22, 23] If the pore size is slightly larger than the analyte, then the hydrogel exerts a dramatic effect on the electrophoretic velocity of the analyte (Part (a) of Figure 3.1). If the hydrogel backbone bears fixed charges, then transport is affected by additional mechanisms including Donnan exclusion[37, 49, 92] and electroosmosis (Part (b) of Figure 3.1).[29] We report findings for the concentration of negatively charged analytes (single-stranded DNA and fluorescein) using highly cross-linked neutral and anionic hydrogels. These materials can lead to analyte enrichment factors of ~500 in just 150 s. Moreover, the approach is simple and compatible with routine microfabrication techniques.

Microfluidic devices offer numerous advantages as chemical analysis platforms; among these is the ability to handle very small volumes of reagents. However, the correspondingly small number of molecules often results in a considerable loss of detection sensitivity. The importance of lowering on-chip detection limits by concentrating the analyte is underscored by the large number of methods that have been developed to address this problem.[4, 93] These include: field-amplified sample stacking (FASS),[8-11] solid-phase extraction (SPE),[12, 13, 94, 95] isotachophoresis (ITP),[14-16] size-exclusion filtration,[22, 23] electrokinetic micellar sweeping,[25, 26] isoelectric focusing (IEF),[20] temperature-gradient focusing (TGF),[17] entropic trapping,[96] and evaporation.[28] However, a highly reproducible, and efficient (fast and with a high enrichment factor)

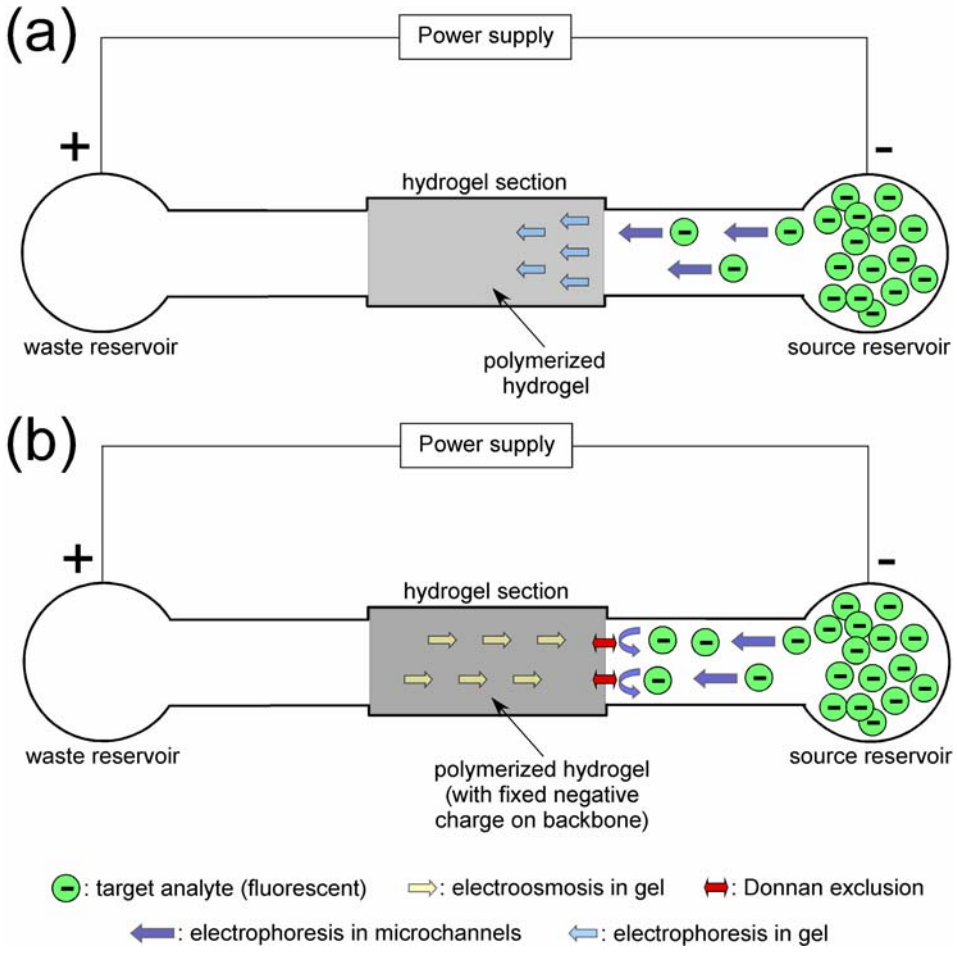

Figure 3.1. Schematic of microfluidic concentration enrichment using hydrogel.

concentration method with minimal microfabrication complexities has been elusive. For example, field-amplified sample stacking is one of the simplest enrichment methods and can achieve up to 1000-fold enrichment, but requires at least two buffer solutions and a relatively large amount of chip space. Solid-phase extraction techniques can yield concentration factors of >500, but they involve the complexity of incorporating appropriate capture and release chemistries inside a microchannel. TGF is capable of achieving extremely high enrichment factors (>10,000 in 40 min), but it requires special buffers, a high operating voltages (~1000 V), and precise temperature control.

The results described here are an extension of a previous study in which we showed that a nanoporous polyester membrane could be used to concentrate DNA in a three-dimensional microfluidic architecture.[29] Specifically, the results of this earlier study showed that in the absence of similitude,[34] it was possible to achieve a balance between the electrophoretic velocity of a charged analyte and the electroosmotic velocity of the solvent. This resulted in a net zero velocity of the analyte near the nanoporous membrane. However, we abandoned this analyte-concentration approach, because it was difficult to reproducibly seal the 10 μm-thick nanoporous membrane between the two fluidic channels. The insight that led to the present findings is that the pores within a track-etched polymeric membrane are similar in some important ways to those found within a hydrogel. This means that the same type of concentration effect we observed in the more complicated three-dimensional system is exhibited by a simple, two-dimensional microfluidic device incorporating a microfabricated hydrogel plug. In

addition to simplifying the fabrication process, the hydrogel microplug approach provides more design flexibility.

There have been a number of previous studies focusing on the integration of hydrogels into microfluidic devices. For example, pH-responsive hydrogels have been used as microfluidic valves by the Beebe, Moore, and coworkers.[54, 97, 98] Likewise, poly(ethylene glycol)-based hydrogel microstructures have been shown to function as passive switches in DNA hybridization arrays.[99] Cells, such as *E. coli*, have been immobilized within hydrogels and used as sensors.[100] Finally, Tarlov and coworkers reported an interesting approach for label-free detection of DNA using hydrogel plugs in microfluidic channels.[94, 101, 102]

Here, we show that two different negatively charged analytes, single-stranded DNA (ssDNA) and fluorescein, can be concentrated using both neutral and anionic hydrogel transport modulators. Within 150 s the neutral hydrogel concentrates ssDNA and fluorescein by factors of 500 and 50, respectively. The corresponding enrichment factors for the anionic hydrogel are 240 and 15, respectively. Although this approach is not optimized, these enrichment factors are comparable to those obtained using most of the more experimentally challenging methods for concentrating analytes mentioned previously. We interpret the results of this study in terms of a qualitative hypothesis. A quantitative analysis, which is presently underway, awaits accurate experimental measurements of some difficult-to-determine electrokinetic parameters and then validation of the hypothesis using appropriate fluid-dynamics simulations.

3.3 Experimental Section

Chemicals. Precursors for preparing poly(dimethylsiloxane) (PDMS, Sylgard 184) microfluidic devices were obtained from Krayden, Inc. (Denver, CO). Fluorescein disodium salt (98+%, Avocado, Heysham, England), 5'-fluorescein-labeled ssDNA (a 22-mer, IDT, Coralville, IA), TRIS base and its hydrochloride salt (TRIZMA brand), acrylic acid (AA), 2-hydroxyethyl methacrylate (HEMA), ethylene glycol dimethacrylate (EGDM), and Irgacure 651 (Sigma-Aldrich, St. Louis, MO) were used as received. All buffer solutions contained 5.0 mM TRIS and 5.0 mM TRIS•HCl (pH 8.3) and were prepared with deionized water (18 MΩ•cm, Milli-Q, Millipore).

Device Fabrication and Layout. Microfluidic channels (20-25 μm in height) were fabricated following a literature procedure.[89] The PDMS monolith (about 6 mm thick) containing the channel was bonded irreversibly to a cover glass (24 mm x 60 mm, 0.13 – 0.17 mm thick, VWR Scientific) after both were treated with an O_2 plasma (60 W, model PDC-32G, Harrick Scientific, Ossining, NY) for 30 s. The layouts of the channels in the resulting devices are shown in Figure. 3.2. The primary microchannel is 90-100 μm wide and 7-7.5 mm long. A wider section of channel (190-200 μm wide and 400 μm long) designed to house the hydrogel microplug is located in the middle of the primary microchannel. The primary microchannel terminates in two 3 mm-diameter reservoirs (ResA and ResB), and it intersects side channels SCh-A and SCh-B. The latter terminate in reservoirs A' and B' (ResA' and ResB'). ResA' and ResB' are necessary to remove the hydrogel precursor from the primary channel following photopolymerization. Two slightly different device designs were used for these studies.

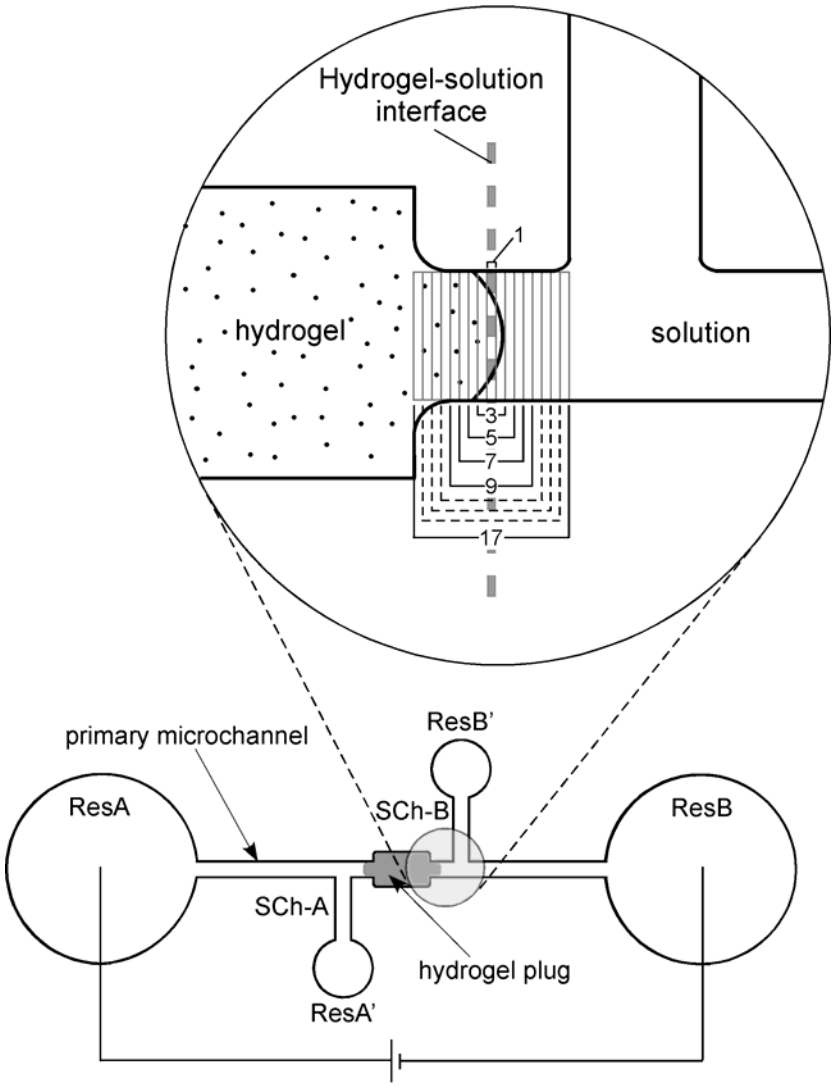

Figure 3.2. Schematic illustration of the microfluidic device used for concentration of ssDNA. The enlarged view shows how the channel cross-sections were defined for quantifying the enrichment factors. A region of interest (ROI) of 1 pixel width (smallest possible area at the selected resolution) was chosen to be as close as possible to the hydrogel-solution interface and other ROIs of increasing widths (denoted by the corresponding numerical values in the enlarged view) were also centered at the hydrogel-solution interface.

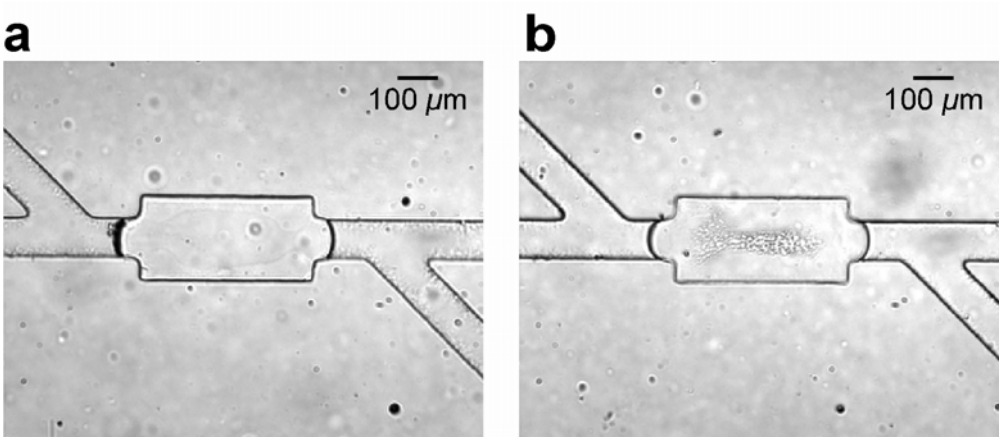

Figure 3.3. Optical micrographs of the microfabricated (a) neutral and (b) anionic hydrogel plugs used for fluorescein concentration experiments after conditioning the hydrogel by applying a bias voltage (100-300 V) between ResA and ResB.

The design shown in Figure 3.2, in which the angle between the primary and secondary channels is 90^{o}, was used for DNA concentration, and another design (see Figure 3.3) having the side channels at 45^{o} relative to the main channel, was used for the fluorescein concentration experiments. This aspect of the device design resulted from an attempt to optimize the side channel configuration, but in fact, the performance arising from both designs was indistinguishable.

Hydrogel Microplug Fabrication. The hydrogel microplugs were fabricated as follows. First, a hydrogel precursor solution was introduced into the primary microchannel by capillary action. Second, UV light (365 nm, 200 s, 300 mW/cm^2, EFOS Lite E3000, Ontario, Canada) was projected onto wide part of the central channel from the side port of a microscope (DIAPHOT 300, Nikon) through a 10x objective lens. Unpolymerized precursor solution was removed by pumping 10.0 mM TRIS buffer (pH = 8.3) through the primary and secondary channels at a flow rate of 10.0 μL/min for > 10 min using a syringe pump (Harvard Apparatus, Holliston, MA).

Procedures and Data Analysis. The electric field inside the primary microchannel was introduced by applying a bias voltage between two coil electrodes (90% Pt/10% Ir, 0.25 mm in diameter and 50.0 mm in length) immersed in ResA and ResB. The bias voltage (range 0 – 1067 V, Ultra Volt, Ronkonkoma, NY) could be switched with a time resolution of 100 ms using a computer and custom software. Before each experiment, the primary microchannel was filled with 10.0 mM TRIS buffer (pH 8.3), and then the hydrogel microplug was conditioned by applying a 100-300 V bias. The conditioning step removes unpolymerized precursor solution from within the

hydrogel. After conditioning, 10.0 mM TRIS buffer was pumped into the left side of the microfluidic system (Figure 3.2) from ResA'. In addition, 10.0 mM TRIS buffer containing the fluorescent analyte (5.0 μM fluorescein or 5.0 μM fluorescein-labeled DNA) was pumped into the right side from ResB' and also into an isolated reference channel for calibration purpose. The syringe pump was disconnected after ensuring that the solutions in all the reservoirs were at the same height (to eliminate pressure-driven flow within the channels). Finally, a programmed sequence of bias voltages (Table 3.1) was applied to the electrodes, and simultaneously a set of fluorescence micrographs were obtained from the region near the hydrogel/open-channel interface (V++ software, Digital Optics, New Zealand, 1 frame/s) using an inverted microscope (TE 300, Nikon, Japan) equipped with a CCD camera (SenSys 1410E, Photometrics, Tucson, AZ). Typically, a total of 360 frames (8 x 8 binning, or 163 x 128 pixels) were captured through a 4x objective lens.

To quantify the enrichment factor near the hydrogel-solution interface, the average fluorescence intensity (counts per second per pixel) was calculated by first integrating all fluorescent photons over a particular region of interest (ROI) and then dividing the result by the total number of pixels in the ROI. The same calculation was also performed over a second ROI located within the reference channel. The enhancement factor is the ratio of the two fluorescence intensities obtained according to the above procedure. Because the fluorescence intensity has a non-uniform distribution, successively larger ROIs were chosen to calculate the enrichment factors. The inset of Figure 3.2 shows that the smallest ROI has a width of 1 pixel and is centered at the

Table 3.1. Programmed Switching of the Bias Voltage Between Reservoirs A and B (ResA and ResB, Figure 3.2).

Time (s)	**Program Action**
<0	0 V bias
0	100 V forward bias (ResA positive)
150	0 V bias
170	100 V reverse bias (ResB positive)
320	0 V bias

hydrogel-solution interface. Other ROIs having increasing widths (3, 5...17 pixels) are centered at this same location. All fluorescence intensity values were corrected by subtracting the background (dark count), which was obtained using a ROI outside the channel at t = 0 s. The effect of photobleaching was not corrected in any reported data. However, control experiments using fluorescein indicated that the decrease in fluorescence intensity due to photobleaching was less than 6% over a period of 400 s of illumination.

3.4 Results and Discussion

Properties of the Hydrogel Microplugs. The hydrogels were photopolymerized as highly cross-linked microplugs within the primary channels of the microfluidic devices using projected UV light.[54] The anionic poly(HEMA-co-AA) hydrogel has a tendency to swell in basic buffers because of the negative charge on its backbone.[49, 98] As depicted schematically in the inset of Figure 3.2, this leads to a slight bulging of the hydrogel along the long axis of the primary channel. Less swelling was observed for the neutral hydrogel. This swelling is advantageous, because it helps to seal the microplug against the channel wall thereby preventing analyte transport through macroscopic leaks that might otherwise develop at these interfaces. Swelling also ensures that the hydrogel microplug remains stationary even under the influence of high electric fields and the pressure-driven flow used during device fabrication. Covalent attachment of the microplug to the walls of the primary channel was thus not required.[103]

The type of highly cross-linked HEMA hydrogel microplugs used in this study have a nanoporous structure with an average pore size of 1.6 nm to 1.9 nm.[104] This dimension can be compared to those estimated for the analytes: the 22-mer ssDNA (MW ~7.252 kDa) has a mean diameter of ~1.3 nm and a length of ~10 nm,[105, 106] and fluorescein can be approximated as a disk having a diameter of ~0.7 nm (calculated using the known bond length data).[107] The important point is that the analytes have a limiting dimension smaller than that of the hydrogel pore size. This excludes the possibility of concentration arising from simple size exclusion.

Analyte Concentration Using Neutral Hydrogel Microplugs. Figure 3.4 is a series of four fluorescence micrographs that demonstrate concentration of ssDNA by a neutral hydrogel microplug. The complete movie from which these individual frames were extracted is provided in the Supplementary Information. Note that the device layout incorporates an isolated reference channel, present in the upper-left corner of each micrograph, which contains a known concentration of fluorescently labeled DNA. This is used for calibration purposes.

The micrograph in Figure 3.4(a) was obtained prior to the application of a bias voltage. Figure 3.4(b) was obtained after applying a 100 V forward bias (ResA at positive potential, Table 1) for 50 s. During this time negatively charged DNA migrates from right to left, but the neutral hydrogel acts as a barrier that greatly reduces its electrophoretic velocity. This results in concentration of DNA near the hydrogel-solution interface. Indeed, an enrichment factor of ~500 is achieved after 150 s (Figure 3.4(c)). This micrograph also shows that some DNA moves into the hydrogel. When the

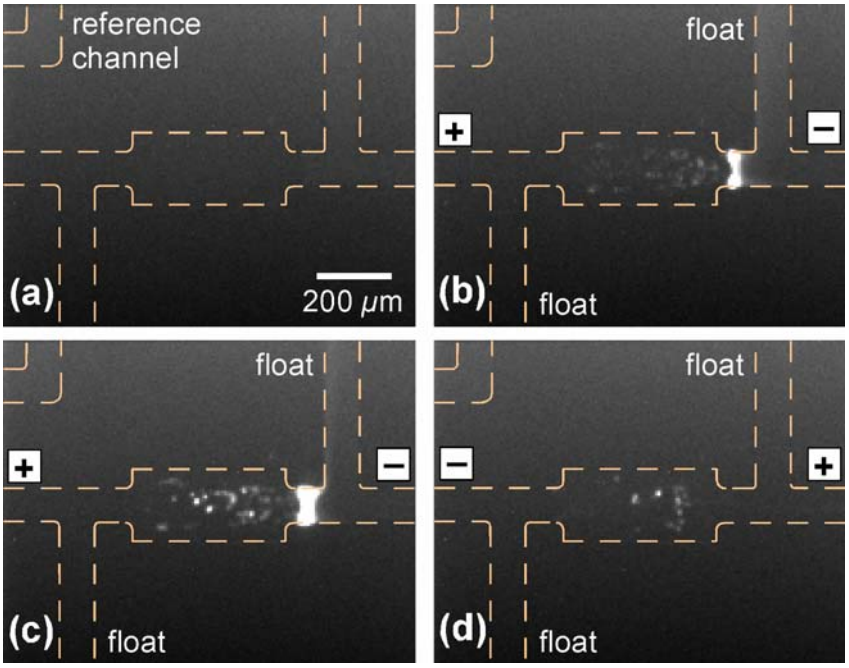

Figure 3.4. Fluorescence micrographs obtained during concentration of ssDNA using the neutral hydrogel in the microfluidic device layout shown in Figure 3.2. (a) Before applying a potential bias. After applying a forward bias of 100 V for (b) 50 s and (c) 150 s. (d) 50 s after applying a reverse bias of 100 V (total elapsed time = 220 s). No bias voltage was applied to the side channels labeled "float". The image size was 163 pixels × 128 pixels, and the full-scale intensity range was 160 to 4095 counts per pixel.

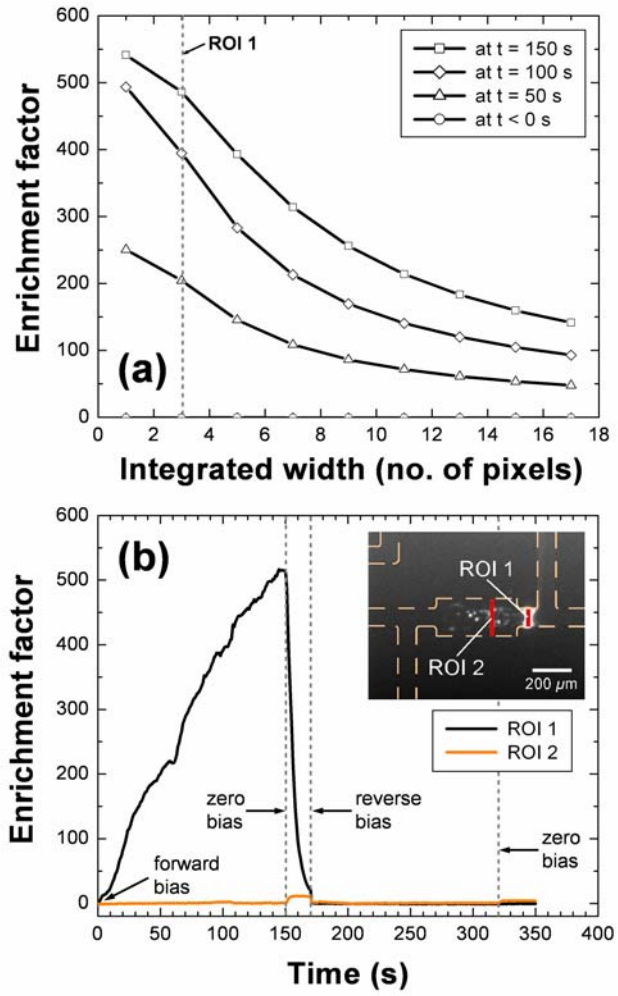

Figure 3.5. Data derived from the micrographs shown in Figure 3.4 for concentration of ssDNA using the neutral hydrogel. (a) Enrichment factors calculated using ROIs having different pixel widths (see the inset of Figure 3.2). (b) Enrichment factor as a function of time for a 3 pixel-wide ROI centered at the hydrogel-solution interface (solid line, ROI 1) and in the hydrogel interior (orange line, ROI 2). The red areas indicated in the inset define the location of ROI 1 and ROI 2.

bias voltage is reversed (Figure 3.4(d)), DNA is rapidly transported away from the concentrated region and back toward ResB. However, some of the DNA trapped within the hydrogel remains.

Figure 3.5(a) shows how the enrichment factor varies as a function of the width of the region of interest (ROI, see Experimental Section and the inset of Figure 3.2) over which the fluorescent signal is averaged. Data are provided prior to the experiment ($t < 0$ s) and at three different times (50, 100, and 150 s) following application of the bias voltage. The maximum enrichment factor is obtained when the ROI has the minimum width (1 pixel). As the width of the ROI increases, the enrichment factor decreases. However, an ROI width of 3 pixels was selected for quantitative analysis, because these data were less subject to slight variations in the alignment of the microscope with the hydrogel-solution interface; that is, they were easily reproduced.

Figure 3.5(b) is a plot of the enrichment factor near the hydrogel surface (ROI 1, which is 3 pixels wide and corresponds to the dashed line in Figure 3.5(a) as a function of time following application of a 100 V bias (solid line). The enrichment factor increased approximately linearly with time until 150 s when the bias was switched to 0 V. Under these conditions the concentration of the enriched DNA band gradually decreased because of steady loss of DNA through the side channel, and the enrichment factor decreased to ~21 at $t = 170$ s. The reason for leakage of the concentrated band through the side channel under these conditions is not clear at present. After 20 s at 0 V bias, a reverse bias of 100 V was applied and the remaining DNA was driven back to ResB. The enrichment factor as a function of time is also shown for ROI 2 inside the

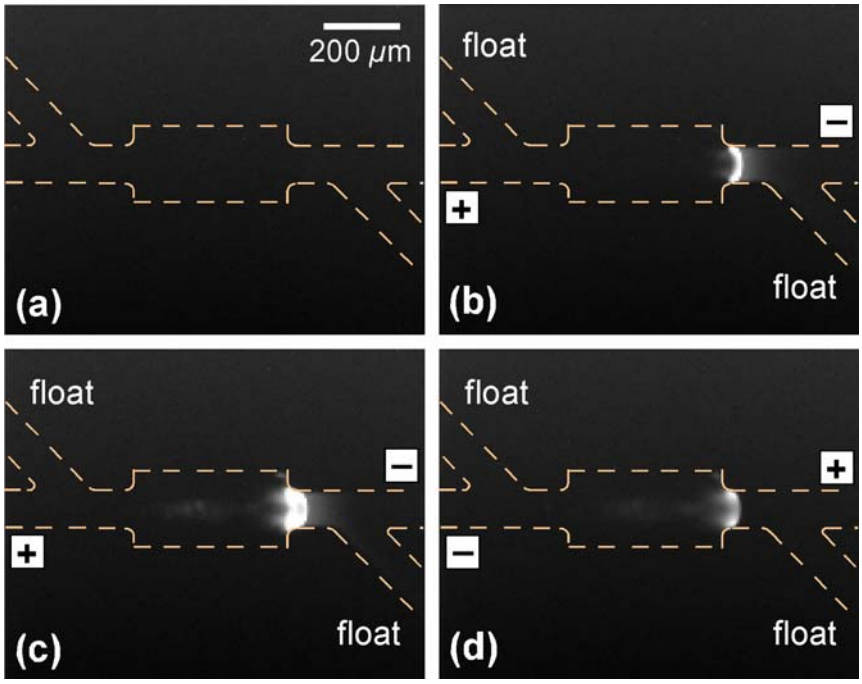

Figure 3.6. Fluorescence micrographs obtained during concentration of fluorescein using the neutral hydrogel in the microfluidic device layout shown in Figure 3.3. (a) Before applying a potential bias. After applying a forward bias of 100 V for (b) 50 s and (c) 150 s. (d) 50 s after applying a reverse bias of 100 V (total elapsed time = 220 s). No bias voltage was applied to the side channels labeled "float". The image size was 163 pixels × 128 pixels, and the full-scale intensity range was 135 to 4095 counts per pixel.

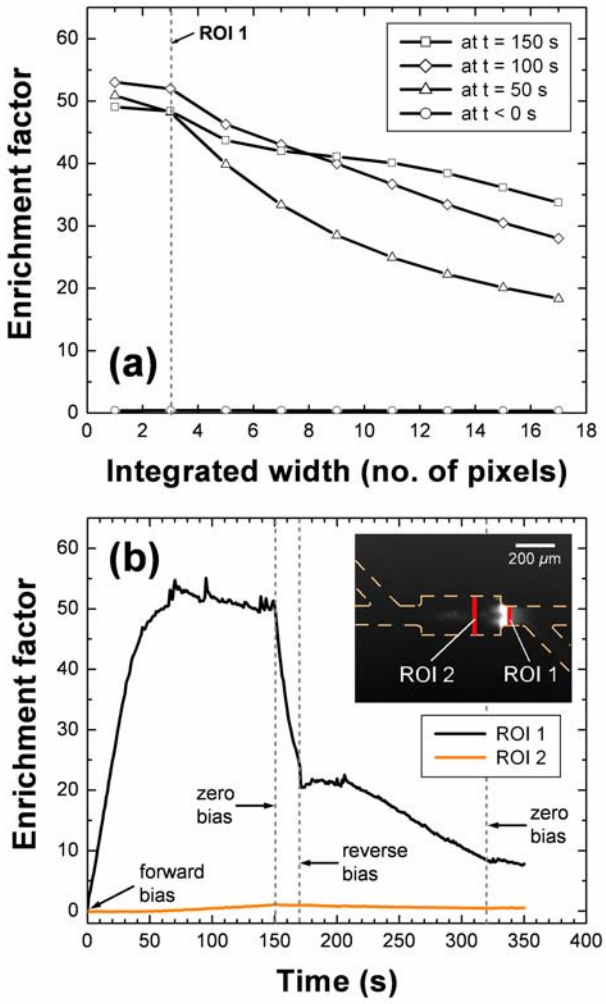

Figure 3.7. Data derived from the micrographs shown in Figure 3.6 for concentration of fluorescein using the neutral hydrogel. (a) Enrichment factors calculated using ROIs having different pixel widths (see the inset in Figure 3.2). (b) Enrichment factor as a function of time for a 3 pixel-wide ROI centered at the hydrogel-solution interface (solid line, ROI 1) and in the hydrogel interior (orange line, ROI 2). The red areas indicated in the inset define the location of ROI 1 and ROI 2.

hydrogel (orange line). The amount of ssDNA that is able to penetrate the hydrogel interior is clearly insignificant compared to the amount concentrated at the hydrogel-solution interface.

Experiments similar to those described for DNA were carried out using fluorescein, which is a small dye molecule carrying two negative charges at the pH used for these experiments.[108] The results (four individual frames as shown in Figure 3.6) are qualitatively similar to those for DNA. However, as shown in Figure 3.7(a), the initial enrichment factors are about an order of magnitude smaller than for DNA (50 vs. 500, respectively). Additionally, the enriched fluorescein band is much broader than for DNA (compare the rate at which the enrichment factor decreases as a function of the integrated pixel width in Figures 3.5(a) and 3.7(a)). Figure 3.7(b) shows that the maximum enrichment factor for fluorescein is achieved within 70 to 80 s, and that further application of the bias voltage actually results in a slight decrease. When the bias is switched to 0 V at t = 150 s, the enriched fluorescein band disperses at a slower rate than ssDNA (compare Figure 3.5(b)). When the bias is reversed at t = 170 s, the fluorescence intensity in ROI 1 remains constant for about 40 s, and then decreases gradually. Recall that the concentration of ssDNA approached zero upon bias reversal (Figure 3.5(b)). We interpret these results in terms of a greater extent of penetration of fluorescein into the hydrogel microplug during application of the forward bias, followed by slow release upon bias reversal.

Although we are not prepared to offer a quantitative explanation for the concentration results shown in Figures 3.4-3.7, we have developed a simple qualitative

model that accounts for the observations reported thus far. We believe that the highly cross-linked hydrogel matrix provides a resistance to ionic mass transfer. This of course increases the magnitude of the electric field inside the hydrogel microplug,[30, 31] which should in turn increase the electrophoretic velocity of charged molecules within the microplug. However, the inhomogeneous nature of the hydrogel results in formation of dead ends and tortuous paths,[37] and therefore the resistance presented by the hydrogel is ion selective: smaller ions, such as those comprising the buffer, carry a higher percentage of the current in the hydrogel than they do in the open channel. Accordingly, the larger analytes carry a smaller percentage of the current in the hydrogel, and this results in their being concentrated at the hydrogel-solution interface. Another way of saying this is that the electrophoretic mobilities of the 22-mer ssDNA (MW ~7.252 kDa) and fluorescein (MW ~0.376 kDa) inside the hydrogel are much smaller than in the open channel. In contrast, the buffer ions are sufficiently small that their mobility is not as medium-dependent. This same argument accounts for the much higher enrichment factor for ssDNA compared to fluorescein. The situation is directly analogous to the differential mobility of different molecular weight DNA oligos observed in gel electrophoresis.

Concentration Using Anionic Hydrogel Microplugs. We thought it might be possible to eliminate analyte penetration into the hydrogel, and thus increase the enrichment factor, by using negatively charged microplugs. Accordingly, we co-polymerized acrylic acid and 2-hydroxyethyl methacrylate to introduce fixed negative

charges onto the hydrogel backbone, and then carried out experiments identical to those described for the neutral hydrogel microplugs.

Figure 3.8 is a series of four fluorescence micrographs obtained before and during application of a 100 V bias voltage to a solution containing 22-mer ssDNA. Prior to application of the bias voltage the fluorescence intensity of the DNA-containing solution is below the detection limit of the measurement system (Figure 3.8(a)). However, when a 100 V forward bias is applied ssDNA begins to concentrate in the vicinity of hydrogel surface (Figures 3.8(b) and 3.8(c)). An enrichment factor of ~240 is obtained within 150 s. When the bias is reversed, the enriched DNA band moves rapidly back toward ResB (Figure 3.8(d)).

Figure 3.9 provides an analysis of the concentration data for ssDNA that is analogous to that previously discussed for the neutral hydrogel. There are four important observations that can be made from the data in Figures 3.8 and 3.9. First, concentration of DNA at ROI 1 increases linearly as a function of time until the bias is switched to 0 V, just as it did for the neutral hydrogel. Second, a maximum enrichment factor is not attained during the 150 s allotted for the experiment. Third, and most surprising, the enrichment factor is lower for the anionic hydrogel than for the analogous neutral gel. Fourth, no DNA can be detected in the hydrogel interior during either the period of the forward or reverse bias.

Data for the concentration of fluorescein using the anionic hydrogel are shown in Figures 3.10 and 3.11. As for ssDNA, the maximum enrichment factor for fluorescein is

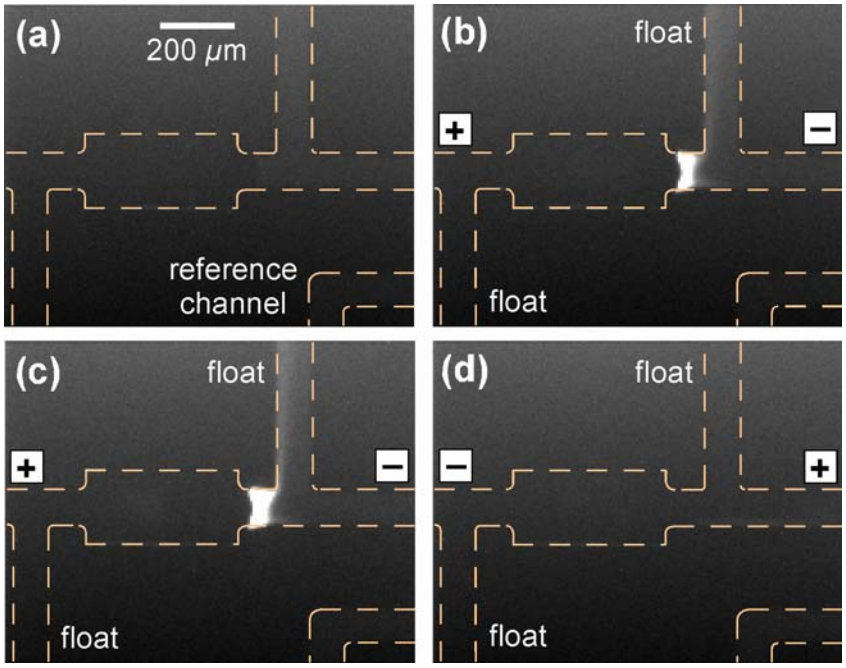

Figure 3.8. Fluorescence micrographs obtained during concentration of ssDNA using the anionic hydrogel in the microfluidic device layout shown in Figure 3.2. (a) Before applying a potential bias. After applying a forward bias of 100 V for (b) 50 s and (c) 150 s. (d) 50 s after applying a reverse bias of 100 V (total elapsed time = 220 s). No bias voltage was applied to the side channels labeled "float". The image size was 163 pixels × 128 pixels, and the full-scale intensity range was 154 to 4024 counts per pixel.

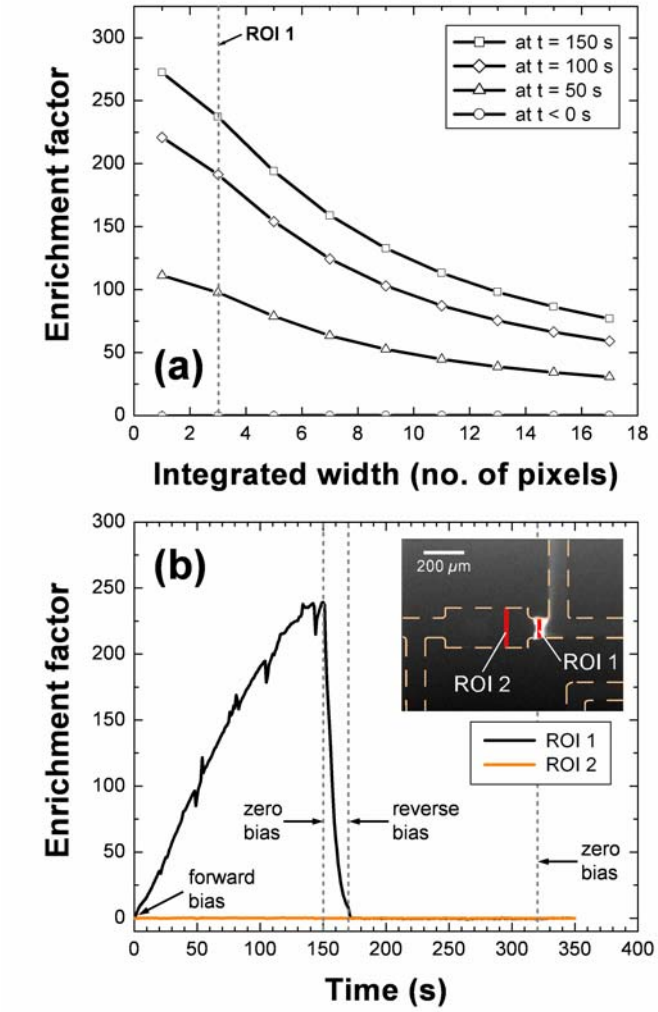

Figure 3.9. Data derived from the micrographs shown in Figure 3.8 for concentration of ssDNA using the anionic hydrogel. (a) Enrichment factors calculated using ROIs having different pixel widths (see the inset of Figure 3.2). (b) Enrichment factor as a function of time for a 3 pixel-wide ROI centered at the hydrogel-solution interface (solid line, ROI 1) and in the hydrogel interior (orange line, ROI 2). The red areas indicated in the inset define the location of ROI 1 and ROI 2.

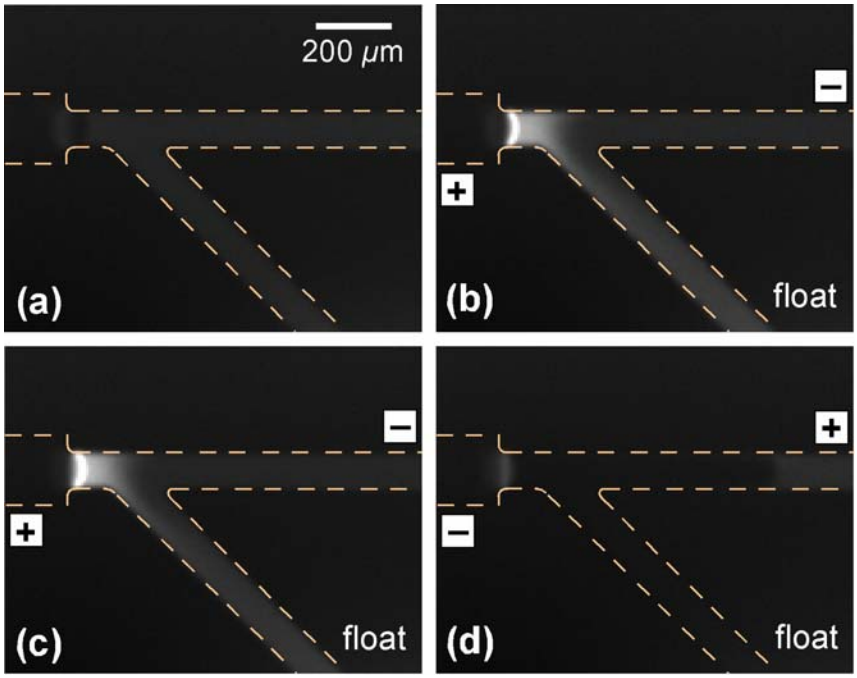

Figure 3.10. Fluorescence micrographs obtained during concentration of fluorescein using the anionic hydrogel in the microfluidic device layout shown in Figure 3.3. (a) Before applying a potential bias. After applying a forward bias of 100 V for (b) 50 s and (c) 150 s. (d) 50 s after applying a reverse bias of 100 V (total elapsed time = 220 s). No bias voltage was applied to the side channels labeled "float". The image size was 163 pixels × 128 pixels, and the full-scale intensity range was 193 to 1978 counts per pixel.

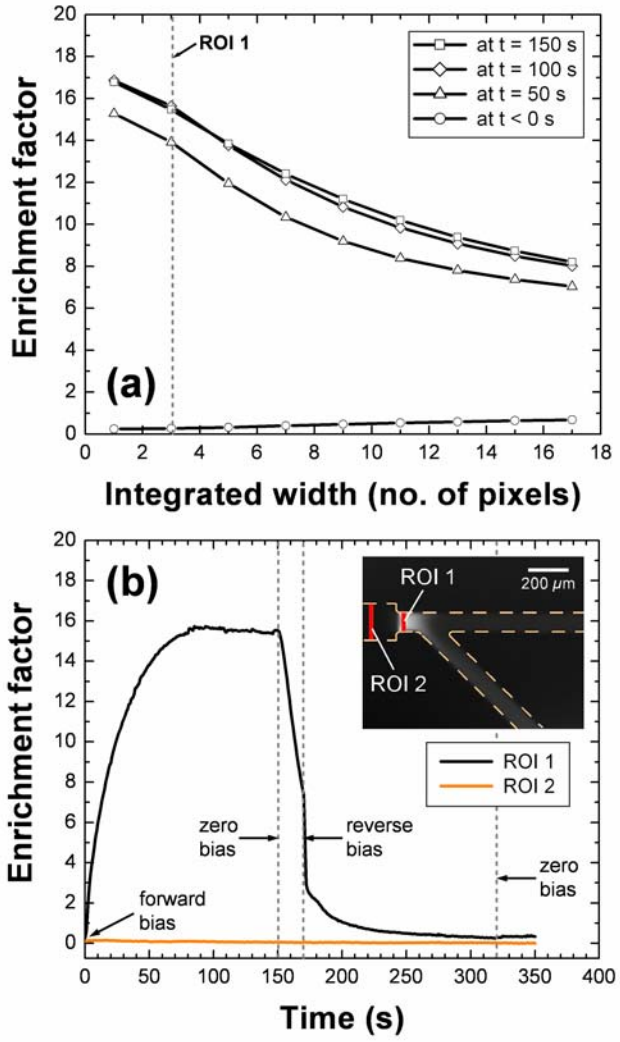

Figure 3.11. Data derived from the micrographs shown in Figure 3.10 for concentration of fluorescein using the anionic hydrogel. (a) Enrichment factors calculated using ROIs having different pixel widths (see the inset of Figure 3.2). (b) Enrichment factor as a function of time for a 3 pixel-wide ROI centered at the hydrogel-solution interface (solid line, ROI 1) and in the hydrogel interior (orange line, ROI 2). The red areas indicated in the inset define the location of ROI 1 and ROI 2.

substantially lower for the anionic hydrogel compared to the neutral gel: 15 vs. 50, respectively. Also, there is no detectable penetration of fluorescein into the anionic microplug. For the anionic hydrogel, a maximum steady-state enrichment factor for fluorescein is attained within about 100 s.

In addition to the ion-size-based differential resistance of the neutral hydrogel discussed earlier, the anionic hydrogel imposes two additional barriers to penetration by negatively charged ions. The first of these arises from Donnan exclusion.[37, 49, 92] Donnan exclusion is operative when the polymer backbone contains fixed charges and the size of the pores within the gel are smaller than the Debye length (that is, the double-layer thickness). Both of these conditions are met for the anionic hydrogels. For example, the average pore size is 1.6 to 1.9 nm,[104] and the calculated Debye length for a 10.0 mM 1:1 electrolyte solution is 3.0 nm.[62] Donnan exclusion ensures that the number of negatively charged analyte molecules will be greatly reduced in the hydrogel interior, and this prediction is in accord with the experimental observations shown in Figures 3.8 - 3.11: both ssDNA and fluorescein are undetectable in the hydrogel interior.

The second difference between the neutral and charged hydrogels relates to the existence of electroosmotic flow (EOF) generated within the pores of the latter. Because the Debye length (3.0 nm) is larger than the average pore size (1.6 to 1.9 nm) the EOF velocity will be reduced,[66, 73] but a careful examination of the data in Figures 3.8 and 3.10 reveals that EOF still exerts a detectable effect on analyte transport. Specifically, there is clear visual evidence that EOF generated by the anionic hydrogel results in streaming of ssDNA and fluorescein from the analyte-enriched band near the gel-

solution interface down the side channel leading to ResB'. We believe this phenomenon is responsible for the lower enrichment factor for the anionic hydrogel compared to the neutral hydrogel.[30]

3.5 Summary and Conclusions

We have demonstrated a new approach for electrokinetic concentration of charged analytes inside microfluidic channels containing a microfabricated hydrogel microplug. The approach is very simple and compatible with standard microfabrication methodologies. Concentration is most effective for large, highly charged molecules like DNA, and enrichment factors of 500 can be obtained within 150 s using low bias voltages (100 V). This method has not been optimized yet, but it seems likely that significantly higher enrichment factors will be obtainable when the system is better understood. Likewise, there is a clear incentive to devise a means for eliminating the side channels from the device layout, because in their absence the EOF may not limit the enrichment factors attainable using anionic hydrogel microplugs. Studies intended to address these experimental issues are presently underway. Simulation and modeling studies are also underway to develop a better theoretical understanding of the results presented herein. We envision that when this concentration methodology is fully developed it will be useful for lowering the detection limit for a variety of on-chip bioassays.

CHAPTER IV

HYDROGEL MICROPLUG AS AN ELECTROKINETIC TRANSPORT MODULATOR

4.1 Synopsis

The functional characteristics of nanoporous hydrogel microplugs in modulating the electrokinetic transport during concentration enrichment of charged analytes within microfluidic devices are described. The physicochemical properties of the hydrogel play an important role in determining the mode of concentration enrichment. A neutral hydrogel plug acts as a physical barrier to the electrophoretic transport of charged analytes resulting in size-based concentration enrichment. However, an anionic hydrogel plug introduces concentration polarization effects ensuing a size and charge-based concentration enrichment. The concentration polarization effects result in redistribution of the local electric field lowering the extent of concentration enrichment. In addition, an electroosmotic flow originating inside the pores of the anionic hydrogel influences the location of concentration enrichment. A theoretical model qualitatively consistent with the observed behavior is provided.

4.2 Introduction

In this paper we describe how nanoscopic pores within a hydrogel microplug situated within a microfluidic channel can be used to control electrokinetic transport generally and analyte preconcentration specifically. The integrated micro-nano fluidic

system provides an interesting case of complex electrokinetic events occurring at phase boundaries between the hydrogel and the buffer solution within the fluidic channel. Specifically, we find that concentration enrichment and depletion are a strong function of the physicochemical properties of the hydrogel, including its internal pore size, charge, and extent of crosslinking. For example, a hydrogel microplug bearing fixed negative charges on its backbone and having a pore diameter on the order of the length of the electric double layer (EDL) behaves as a permselective cation-exchange membrane (Figure 4.1). Under the influence of an electric field, an imbalance between the molar fluxes of co-ions within the hydrogel and the microchannel results in concentration enrichment at interface between the hydrogel and the solution in the cathodic compartment of the microfluidic device (inset of Figure 4.1). The magnitude of this enrichment and its location, however, is determined by the extent of concentration depletion in the anodic compartment and electroosmotic flow (EOF) originating inside the hydrogel pores.

The study presented here complements previous related reports from our group.[29, 35] Specifically, we showed that a three-dimensional microfluidic system, consisting of a thin nanoporous polyester membrane sandwiched between two microfluidic channels, could be used to concentrate DNA.[29] However, this type of device was difficult to reproducibly fabricate, and therefore we adopted an analogous two-dimensional system for subsequent studies. The two-dimensional device consisted of a single microfluidic channel divided into two compartments by a photopolymerized hydrogel microplug.[35, 54] In this configuration, the nanoscopic pores within the hydrogel

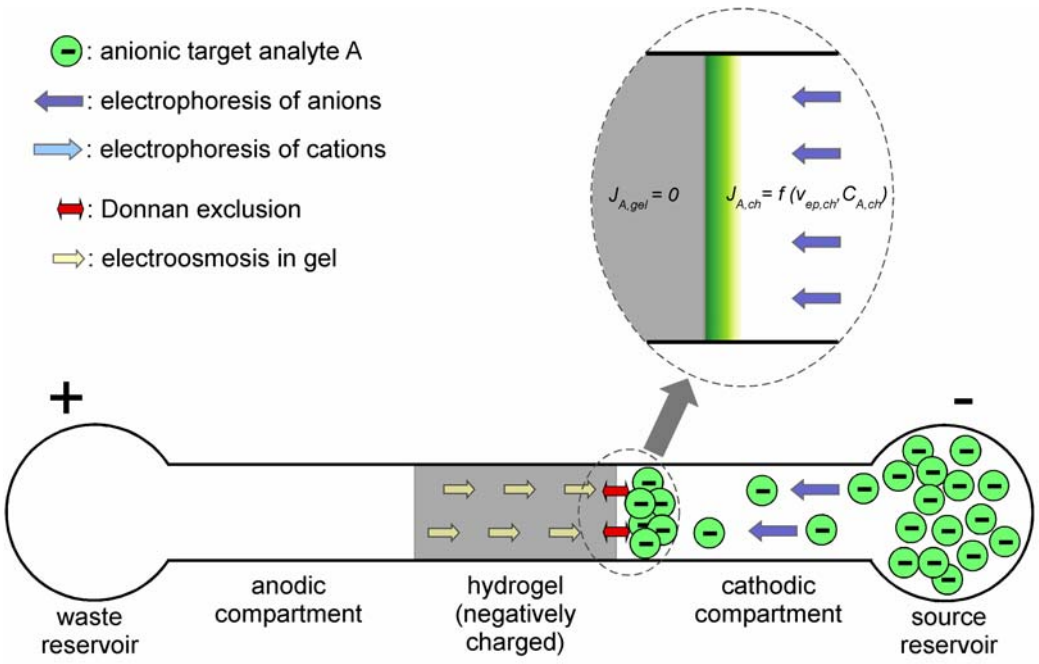

Figure 4.1. Schematic of hydrogel microplug as an electrokinetic transport modulator.

act as fluidic transport modulators. This design was much easier to fabricate than the three-dimensional system and resulted in concentration enrichment of negatively charged analytes, such as single-stranded DNA (ssDNA) and fluorescein. For example, we achieved a ~500-fold enrichment of ssDNA in just 150 s using potentials on the order of ~100 V. In the present study we have further simplified the microfluidic system in an effort to reduce experimental variables and thus better understand the factors governing analyte concentration.

A decade after its advent, the field of microfluidics has established the advantages of small sample volumes, rapid-response times, and portability and is showing a great promise for practical applications in analytical technologies.[109] As a next step, a number of research groups have started focusing on further miniaturization, and the field of nanofluidics has emerged.[110, 111] However, rules that govern the transport of fluids in micron-scale channels may not be appropriate for channels having critical dimensions comparable to the size of molecules or polymers. For example, Rubinstein and coworkers have studied ion-exchange membranes of the type used for electrodialysis and provided theories of electric field distribution and electrokinetic instabilities around the membrane.[74-76] Tallarek's group has used these ideas to explain concentration polarization and nonequilibrium electrokinetic effects in nanoporous glass beads packed in capillaries.[77-79] In related work, the nonlinear electrokinetic behavior of simple ionic systems with hydrogels, and their application as electrolyte diodes and transistors, has been described by Marek *et al*.[80] A qualitative discussion of the ion-enrichment and depletion effect of nanoslits due to the EDL overlap has been reported by Liu.[81] Similar

studies have been carried out by Plecis *et al*., who studied a concentration gradient across a Pyrex nanoslit in the absence of an electric field.[82] Lopez and coworkers have found that by adjusting the widths of nanochannels it is possible to achieve variation in the electrokinetic velocities of dye molecules having different chemical properties.[83]

Here, we explore the fundamental properties of neutral and anionic 2-hydroxyethyl methacrylate (HEMA) hydrogel microplugs and demonstrate how these can be manipulated to control electrokinetic transport inside microfluidic channels. Under the influence of electric field, a neutral hydrogel acts as a physical barrier to electrophoretic migration of a negatively charged analyte resulting in concentration enrichment at the interface between the hydrogel microplug and the buffer solution within the channel. However, when a negatively charged hydrogel is used, the behavior of the system is more complex. Specifically, the extent and location of the analyte-enriched zone is dictated by the magnitude of the local electric field near and within the hydrogel. Here, we provide a simple theoretical model that is qualitatively consistent with experimental observations of analyte enrichment in the vicinity of negatively charged HEMA hydrogel microplugs contained within poly(dimethylsiloxane) (PDMS)/glass microfluidic channels. Specifically, the model is consistent with the behavior observed for analytes having different sizes, charge, and physicochemical properties.

4.3 Experimental Section

Chemicals. Precursors for preparing PDMS (Sylgard® 184) microfluidic devices were obtained from K. R. Anderson, Inc. (Morgan Hill, CA). Fluorescein disodium salt (98+%, Avocado, Heysham, England), 5'-carboxyfluorescein-labeled 22-mer and 50-mer ssDNA (IDT, Coralville, IA), and bovine serum albumin (BSA) tagged with Alexa Fluor® 488 from Molecular Probes, Inc., Eugene, OR) were used as fluorescent analytes. Acrylic acid (AA), 2-hydroxyethyl methacrylate (HEMA), ethylene glycol dimethacrylate (EGDMA), and Irgacure 651 (Sigma-Aldrich, St. Louis, MO) were used as received. The 10.0 mM TRIS-HCl buffer (pH 8.1) used in all experiments was obtained by diluting molecular biology grade 1 M TRIS-HCl buffer (Fisher Biotech, Fair Lawn, NJ) with deionized water (18 MΩ•cm, Milli-Q® Gradient System, Millipore).

Microfluidic Device Fabrication. The fabrication of PDMS/glass hybrid microfluidic devices employed for the concentration enrichment experiments followed a literature replica molding procedure.[89] First, reservoirs or ports for fluidic delivery were created by punching holes (~ 2.5 mm in diameter) into a PDMS monolith (~5 mm thick) containing the microchannel layout. The monolith was then washed with ethanol and dried under a stream of N_2 gas. It was then bonded irreversibly to a pre-cleaned cover glass (25 mm × 25 mm, 0.13 – 0.17 mm thick, VWR Scientific) after both were treated with an O_2 plasma (60 W, model PDC-32G, Harrick Scientific, Ossining, NY) for 15 s. Bonding was carried out for at least 2 min before introducing liquids into the microchannel. The resulting microfluidic architecture (Figure 4.2) included a straight microchannel (approximately 100 μm wide, 20 μm deep, and 6 mm long) terminating in

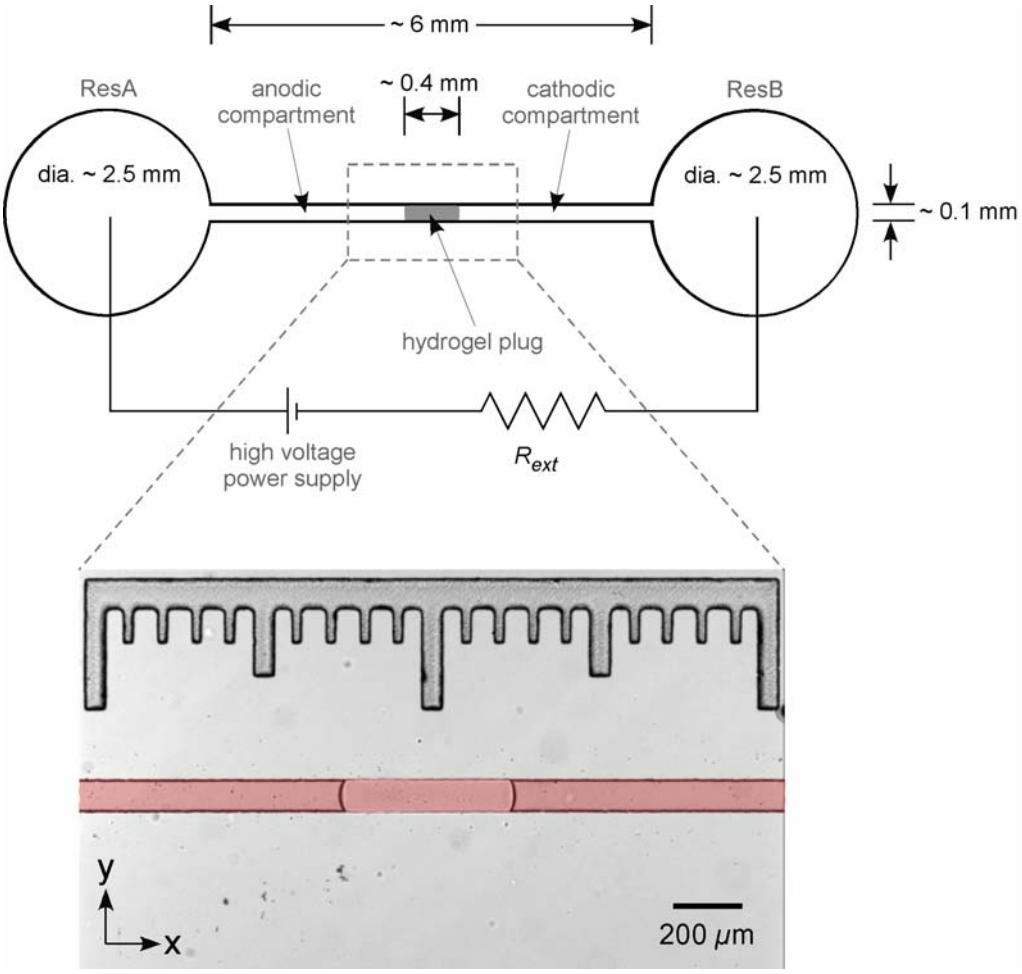

Figure 4.2. Schematic illustration of the microfluidic device used for the electrokinetic studies reported here. The enlarged view is a microscopic optical image (4x objective lens) of a channel section incorporating a hydrogel microplug. A 2 mm internal scale bar was also embedded in the microfluidic design as a reference for hydrogel polymerization. The enlarged view demonstrates how the region of interest (ROI, red color) was defined for obtaining the fluorescence intensity profiles along the channel.

the two punched reservoirs (ResA and ResB). In contrast to the microfluidic device used in our previous studies,[35] this design does not incorporate the sidechannels used to remove the unwanted hydrogel precursor from the channel following photopolymerization. This new design, which greatly simplifies modeling, was enabled by the development of an electrokinetic strategy for removing unpolymerized hydrogel precursor (vide infra).

Hydrogel Microplug Fabrication. The hydrogel microplug was incorporated into the microchannel by photopolymerization of appropriate precurors. First, a hydrogel precursor solution was introduced into the microchannel by capillary action. Next, UV light (365 nm, 200 s, 300 mW/cm^2, EFOS Lite E3000, Ontario, Canada) was projected onto the central part (~400 μm long) of the channel from the side port of a microscope (DIAPHOT 300, Nikon) through a 10x objective lens. This resulted in polymerization of the precursors in the illuminated region. To remove the unpolymerized precursor solution, ResA and ResB were filled with 10.0 mM TRIS-HCl buffer (pH 8.1), which was allowed to diffuse into the microchannel for about 90 min. A range of voltages from 50 to 400 V was applied between two coil electrodes (90% Pt/10% Ir, 0.25 mm in diameter and 50.0 mm in length) immersed in ResA and ResB. The necessary electrical bias was applied using a custom-built, high-voltage (range 0-1067 V) power supply unit using a single output module of high power C series voltage source (Ultra Volt, Ronkonkoma, NY). The applied voltages could be changed with 100 ms time resolution using custom software. The conditioning step removes unwanted precursor from the vicinity of the polymerized hydrogel. In case of anionic hydrogels, the residues

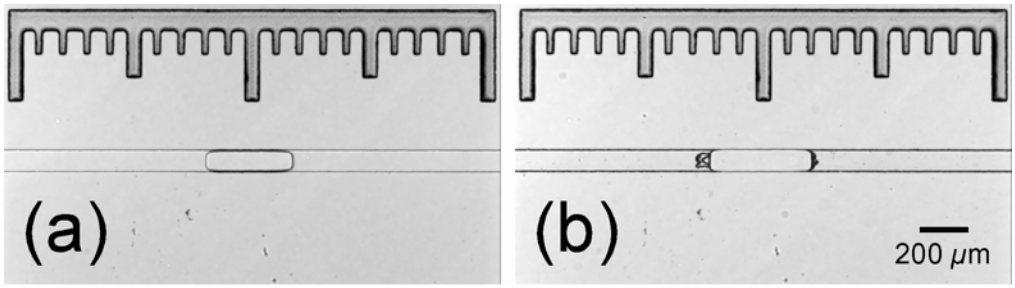

Figure 4.3. Optical micrographs of a neutral hydrogel microplug after (a) photopolymerization and (b) conditioning by applying a bias voltage (50-400 V) between ResA and ResB (Figure 4.2). Sometimes however, the removal of unwanted precursor residues from the vicinity of hydrogel microplug (during conditioning) resulted in the attachment of the residues to the original hydrogel plug.

remaining in the channel after photopolymerization of the hydrogel microplugs carry negative charges, and therefore they can be electrophoretically transported to the reservoirs and then removed using biases of 50-150 V. The neutral hydrogels cannot be removed electrophoretically, but it was possible to remove these residues using electroosmotic flow induced by biases of up to 400 V. Sometimes however, this treatment resulted in attachment of the residues to the original hydrogel plug (see Figure 4.3). These small residues had no significant effect on the electrokinetic transport phenomena inside the microfluidic device.

Data Acquisition and Analysis. After conditioning, ResA and ResB were rinsed with 10.0 mM TRIS-HCl buffer and 25 μL of the fluorescent analyte (5.0 μM fluorescein, 500.0 nM of BSA – Alexa Fluor conjugate or fluorescein labeled ssDNA (5.0 μM of 22-mer or 500.0 nM of 50-mer) in 10.0 mM TRIS-HCl buffer) was introduced into each reservoir. A bias voltage was established between the electrodes in the two reservoirs, and simultaneously a set of fluorescence micrographs was captured (V++ microscopy imaging, Digital Optics, New Zealand) from the channel region near the hydrogel using an inverted epifluorescence microscope (Eclipse TE 2000-U, Nikon, Japan) equipped with a CCD camera (Cascade 512B, Photometrics, Tuscon, AZ). A typical capture sequence included 541 frames (4x objective lens, 1 × 1 binning, 512 × 290 pixels) at a rate 2 s/frame (exposure time 100 ms) spanned over 1080 s. For enhanced visual quality, the images were modified to an appropriate grayscale and a false color scheme was applied (brightness decreasing in the order white-green-blue-black). During the application of the electrical bias, the voltage drop across an external

resistor R_{ext} (510 KΩ) connected in series with the microfluidic channel (Figure 4.2) was recorded every 60 s using a multimeter.

To analyze the fluorescence intensities and corresponding enrichment factors in the microfluidic system, the entire channel section under the microscopic view was chosen as a region of interest (ROI) (red colored region in the inset of Figure 4.2). The width-averaged (averaged along the y-axis) fluorescence intensity profiles were obtained along the channel (x-axis) over the entire ROI at different time intervals. The corresponding enrichment factors were calculated by dividing the peak heights in the fluorescence intensity profiles to the average fluorescence intensity obtained in a reference channel containing just the original fluorescent analyte. All fluorescence intensity values were corrected by subtracting the background count and normalized before obtaining the fluorescence intensity profiles.

The current flowing through the microchannel was calculated from the recorded values of the voltage drop across R_{ext} using Ohm's relation and was plotted as a function of time.

4.4 Results and Discussion

Theory. The microfluidic system shown in Figure 4.2 can be divided into three parts: (1) the anodic compartment connected to a reservoir containing a positive electrode; (2) a nanoporous hydrogel microplug; and (3) a cathodic compartment connected to the other reservoir and containing a grounded electrode. The highly cross-linked hydrogel has a nanoporous structure with an estimated average pore size of a few

nanometers (~1.6 nm in this study).[35, 104] This nanoporous structure greatly increases the electrical resistance of the channel. For example, the electrical resistance of a microfluidic channel, in which acrylic acid (AA) is copolymerized with HEMA (AA-co-HEMA hydrogel) over the entire length of the channel, is ~14 GΩ/cm, and this value can be compared to an otherwise identical open channel, which has a resistance of ~72 MΩ/cm. The hydrogel microplug also increases the resistance to pressure-driven fluid flow to such a high degree that it can be neglected in comparison to the velocity of electrokinetic flow.

In open (that is, no hydrogel microplug) O_2 plasma-treated PDMS/glass hybrid microchannels, deprotonated surface hydroxyl groups give rise to electroosmotic flow (EOF). The magnitude of this EOF in terms of the electroosmotic mobility ($\mu_{eo,ch} \sim 4.5 \times 10^{-4}$ cm^2/V·s at pH 8.1) exceeds the electrophoretic mobility (μ_{ep}) for negatively charged analytes such as fluorescein ($\mu_{ep,Fl} = -3 \times 10^{-4}$ cm^2/V·s) and hence no net electrophoretic migration towards anode is possible. However, in the presence of a hydrogel microplug bearing fixed negative charges on its backbone, the steady-state EOF ($Q_{eo,gel}$) in the system is controlled by the EOF existing inside the hydrogel, which is given by equations (4.1) and (4.2).

$$Q_{eo,gel} = \bar{v}_{eo,gel} \cdot A_{gel} \tag{4.1}$$

$$\bar{v}_{eo,gel} = \frac{1}{2a}\int_{2a} v_{eo,gel}\, dy\,, \qquad v_{eo,gel} = \mu_{eo,gel} E_{gel}\left(1 - \frac{\phi(y)}{\zeta_{gel}}\right) \tag{4.2}$$

Here, $\bar{v}_{eo,gel}$ is the average electroosmotic velocity inside the gel, A_{gel} is the cross-sectional area available for flow inside the gel, a is the average pore radius, E_{gel} is the electric field strength across the hydrogel plug, $\phi(y)$ is the potential field inside a hydrogel pore, and ζ_{gel} is the zeta potential of the nanopore surface. For the 10 mM TRIS-HCl buffer used in the experiments reported here, the calculated Debye length (δ_D = 3.0 nm) is of the order of the average pore size.[35] In fact, because the ratio $a/\delta_D <$ 1 there will be a high degree of electric double layer (EDL) overlap, and therefore the magnitude of the electroosmotic velocity is reduced well below the maximum possible velocity: $v_{eo,gel(\max)} = \mu_{eo,gel} E_{gel}$ for $a \gg \delta_D$.[66, 73] At steady-state, the EOF inside the hydrogel equals the EOF in the microchannel (equation (4.3)),

$$Q_{eo,ch} = \bar{v}_{eo,ch}^{eff} \cdot A_{ch} \tag{4.3}$$

where $\bar{v}_{eo,ch}^{eff}$ is the effective average electroosmotic velocity in the microchannel and A_{ch} is the microchannel cross-sectional area. Because the intra-hydrogel flow area, A_{gel}, is only a fraction of A_{ch} ($A_{gel} = \varepsilon_p A_{ch}$, $\varepsilon_p < 1$ where ε_p is the hydrogel porosity), $\bar{v}_{eo,ch}^{eff}$ is much lower than $\bar{v}_{eo,gel}$. This $\bar{v}_{eo,ch}^{eff}$ term is in turn lower in magnitude than the electrophoretic velocity, $v_{ep,ch} = \mu_{ep} E_{ch}$, which facilitates a net electrophoretic migration of the analyte toward anode in the microchannel.

For the migration of negatively charged species in the microchannel under the influence of the applied electric field, a molar flux equation can be written as a

combination of electromigration, and diffusive and convective fluxes (e.g., the Nernst-Planck equation, equation (4.4)),[61]

$$J_{A,ch} = -\mu_{ep,A} z_A F C_{A,ch} \nabla \phi_{ch} - D_{A,ch} \nabla C_{A,ch} + C_{A,ch} \bar{v}_{eo,ch}^{eff} \tag{4.4}$$

where subscript A represents anions, z_A is the signed charge number (negative for anions), F is the Faraday constant, $D_{A,ch}$ is the diffusivity, and $C_{A,ch}$ is the concentration of anions in the channel, and ϕ_{ch} is the local electric potential. In the microchannel, electrophoretic migration is considerably stronger than electroosmotic convection ($C_A \bar{v}_{eo,ch}^{eff}$) in the opposite direction. Hence, equation (4.4) reduces to equation (4.5).

$$J_{A,ch} = -\mu_{ep,A,ch} z_A F C_{A,ch} \nabla \phi_{ch} - D_{A,ch} \nabla C_{A,ch} \tag{4.5}$$

A similar molar flux equation can be written for the anionic species across the nanoporous hydrogel section (equation (4.6)),

$$J_{A,gel} = -\mu_{ep,A,gel} z_A F C_{A,gel} \nabla \phi_{gel} - D_{A,gel} \nabla C_{A,gel} + C_{A,gel} v_{eo,gel} \tag{4.6}$$

where $C_{A,gel}$ is the concentration of anions in the hydrogel and ϕ_{gel} is the local electric potential in the gel. $D_{A,gel}$ is the effective diffusivity of anions within the hydrogel.

The hydrogel has a fixed negative charge on its backbone and hence behaves as a permselective cation-exchange membrane. Depending on the surface density of these fixed negative charges, the pore size and the subsequent degree of EDL overlap, co-ionic species (anions in this case) are restricted from entering the hydrogel by Donnan exclusion.[37, 49, 92] This can be represented simply in terms of an equilibrium gel partition

coefficient, $K_A = C_{A,gel} / C_{A,ch}$ at equilibrium. A high degree of EDL overlap and significant negative charge density on the hydrogel backbone means K_A«1, which corresponds to a negligible flux of anions through the hydrogel (equation (4.7)).

$$J_{A,gel} \approx 0 \tag{4.7}$$

Thus, an imbalance between $J_{A,ch}$ and $J_{A,gel}$, as indicated by equations (4.5) and (4.7), results in concentration enrichment of anions near the interface between the hydrogel and the solution in the cathodic compartment. Simultaneously, this gives rise to a concentration gradient at this interface and the diffusive flux term in equation (4.5) gains importance, resulting in the diffusion of anions away from the hydrogel and broadening of the enriched band.

At the same time, a rather complex sequence of electrokinetic events takes place near the boundary between the hydrogel and the solution in the anodic compartment. Upon application of the electric field, there is a depletion of ions in the diffusion layer between the hydrogel and the solution in the anodic compartment. Anions in this diffusion layer diffuse into the bulk solution and are readily transported toward the anode, while cations diffuse toward the hydrogel surface and rapidly migrate through the cation-exchange hydrogel toward the cathodic compartment. This concentration depletion near the interface between the hydrogel and the anodic compartment, in conjunction with the concentration enrichment near the other hydrogel interface, is called concentration polarization.[74-80] The depletion of ions in the diffusion layer between the hydrogel and the solution in the anodic compartment leads to a higher potential drop in the anodic compartment. This redistribution of the applied electric field

reduces the local electric field in the cathodic compartment, thus limiting the extent of concentration enrichment.

It is also important to note that a transient increase in the magnitude of $\overline{v}_{eo,gel}$ may cause a substantial $\overline{v}_{eo,ch}^{eff}$ displacing the enriched zone of anions near the hydrogel-solution cathodic interface away from the hydrogel.

Neutral Hydrogel Microplug as a Physical Barrier. The fluorescence micrographs shown in Figure 4.4 demonstrate the role of a neutral hydrogel microplug in impeding the electrophoretic migration of two negatively charged species having different sizes: fluorescein (Figure 4.4(a) and (b)) and BSA (Figure 4.4(c) and (d)). Figure 4.4(a) is a micrograph obtained for fluorescein before application of an electric field, and Figure 4.4(b) was obtained after applying a forward bias (ResA at positive potential and ResB grounded) of 100 V for 480 s. The voltage bias induces electrophoretic migration of fluorescein in ResB toward the anodic compartment (ResA). However, the nanoporous hydrogel imposes a physical limitation on the electrophoretic velocity of fluorescein inside the microplug. Although fluorescein is smaller (MW ~0.376 kDa, < 1.0 nm in size) than the estimated pore size (~1.6 nm) of the hydrogel,[35, 104] the high cross-linking density and tortuous nature of nanoporous network considerably decreases the effective diffusivity ($D_{Fl,gel}$) and hence the electrophoretic mobility ($\mu_{ep,Fl,gel} = D_{Fl,gel} / RT$) of fluorescein within the hydrogel.[37, 61] Subsequent the velocity difference between the electrophoretic migration in the microchannel and within

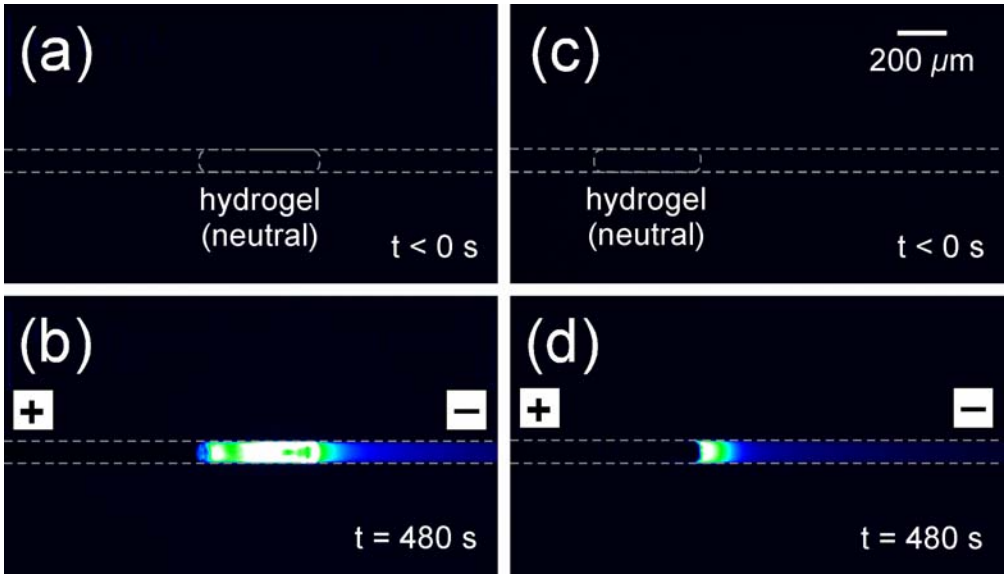

Figure 4.4. Fluorescence micrographs obtained in the microfluidic device (layout shown in Figure 4.2) with the neutral hydrogel microplug for (a) and (b) fluorescein and (c) and (d) BSA, (a) and (c) before and (b) and (d) after applying a forward bias of 100 V for 480 s. The image size was 512 pixels × 290 pixels, and the grayscale applied was 1700 to 12000 counts per pixel. The micrographs were modified using a false color scheme (fluorescence intensity decreasing in the order white-green-blue-black).

the hydrogel results in accumulation of fluorescein at the interface between the hydrogel and the solution in the cathodic compartment, and within the hydrogel interior despite the higher intra-gel electric field.[30, 31, 35]

Experiments analogous to those just described were also carried out using BSA as the probe. BSA (MW ~66.000 kDa, size 4.0 × 14.0 nm),[112] is protein and hence much larger than fluorescein. Figure 4.4(c) and (d) are micrographs obtained before and after the application of a 100 V forward bias for 480 s. In this case, the hydrogel pore size is much smaller than the BSA probe, and therefore the hydrogel microplug acts as a size-exclusion membrane. Accordingly, BSA is concentrated at the cathodic hydrogel interface. This result is qualitatively similar to related experiments carried out previously by others.[21-23, 113]

Figures 4.5 and 4.6 show the fluorescence intensity profiles for fluorescein and BSA, respectively, obtained along the channel at different times during application of the 100 V forward bias. Figure 4.5 indicates a substantial amount of fluorescein accumulated within the hydrogel microplug after applying the bias. The accumulated fluorescein is unevenly distributed due the heterogeneous nature of the nanoporous network. Fluorescein is also concentrated at the interface between the hydrogel and the cathodic compartment.

In contrast to the fluorescein results, no fluorescence intensity is observed within the hydrogel for BSA during application of the forward bias (Figure 4.6), except at the very edge of the microplug. We believe this small amount of concentration is an artifact

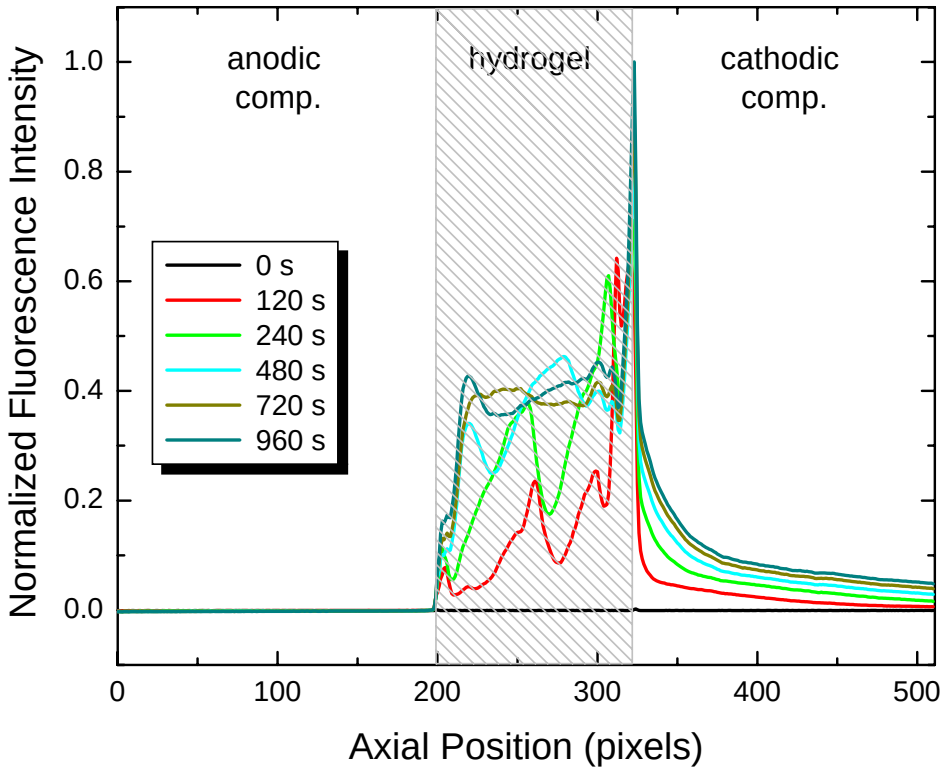

Figure 4.5. Fluorescence intensity profiles for fluorescein obtained parallel to the channel incorporating a neutral hydrogel microplug. All fluorescence intensity values were corrected by subtracting the background count before normalization. Applied potential bias = 100 V (forward).

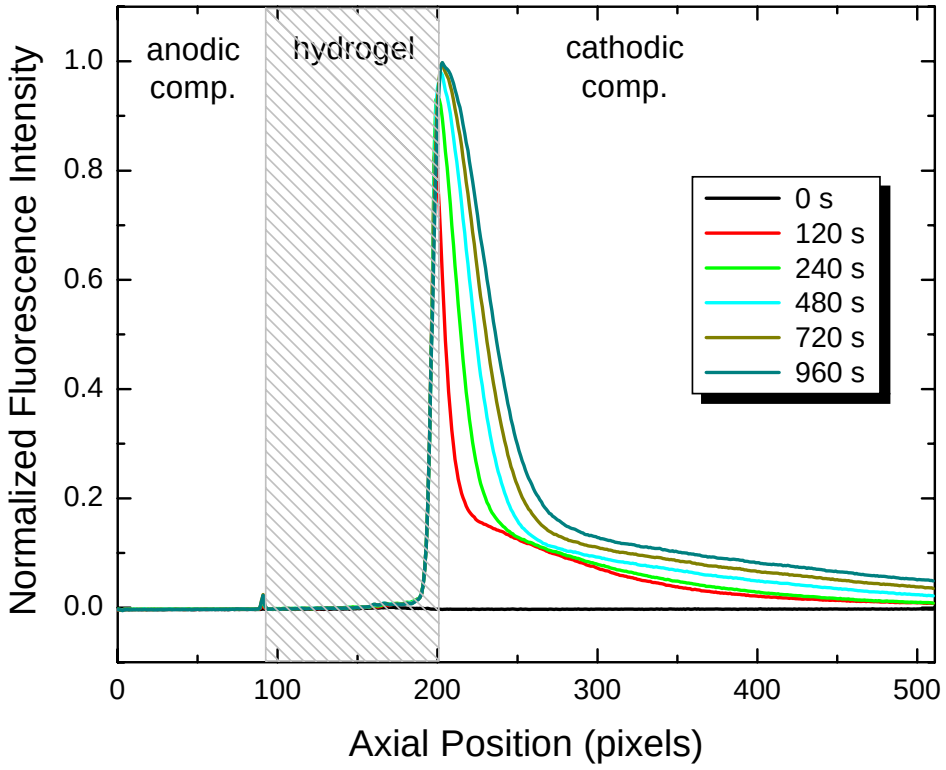

Figure 4.6. Fluorescence intensity profiles for BSA obtained parallel to the channel incorporating a neutral hydrogel microplug. All fluorescence intensity values were corrected by subtracting the background count before normalization. Applied potential bias = 100 V (forward).

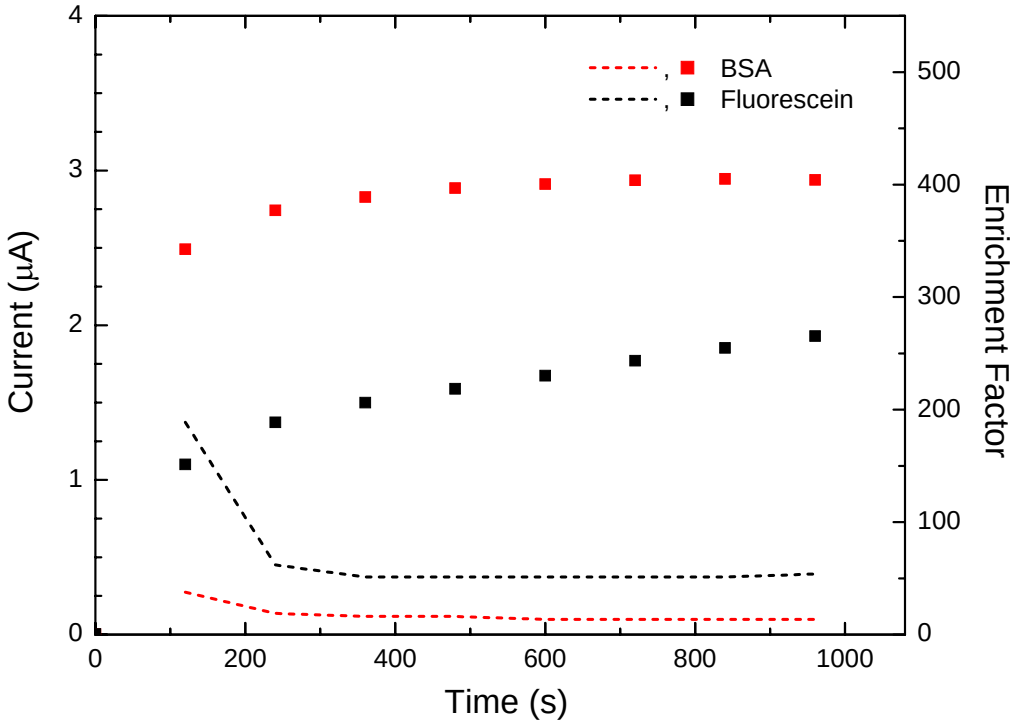

Figure 4.7. Current (dotted lines) flowing through the microfluidic channel and the concentration enrichment factors (solid squares) observed at the interface between the hydrogel microplug and the solution in the cathodic compartment as a function of time for fluorescein and BSA in channels incorporating a neutral hydrogel microplug. The enrichment factors correspond to the respective peak heights in the fluorescence intensity profiles shown in Figures 4.5 and 4.6.

of how the interface between the hydrogel and solution is defined: that is, the actual interface is larger than the resolution of the camera used to obtain images. Clearly, however, BSA is excluded from the hydrogel due to its large size and concentrates at the interface between the hydrogel and the solution in the cathodic compartment.

The current flowing through the microfluidic system and concentration enrichment factors obtained at the hydrogel-solution interface during the 100 V forward bias are compared for fluorescein and BSA in Figure 4.7. In both cases there is a sudden rise in the enrichment factor within 120 s of the application of the electric field. Simultaneously, the current drops quickly after a sharp initial rise (typically during the first 10 s after application of the field, not shown) and then reaches steady state. The enrichment factors for both fluorescein and BSA begin to level-off for $t > 120$ s. The enrichment factor obtained for BSA after 960 s (~400) was much higher than for fluorescein (~250). This difference is mainly a consequence of fluorescein penetration into the hydrogel. The migration of fluorescein through the hydrogel also results in higher current than is observed for BSA.

Anionic Hydrogel Microplug as an Electrochemical Barrier. The presence of negative charges on the hydrogel microplug results in substantially different behavior compared to the neutral hydrogel. Figure 4.8 are fluorescence micrographs obtained for fluorescein (Figure 4.8(a) and (b)) and BSA (Figure 4.8(c) and (d) before (Figure 4.8(a) and (c)) and during (Figure 4.8(b) and (d)) application of an electric field (for 480 s) across a negatively charged AA–co-HEMA hydrogel microplug. Under the influence of an electric bias of 100 V, fluorescein in ResB is electrophoretically transported towards

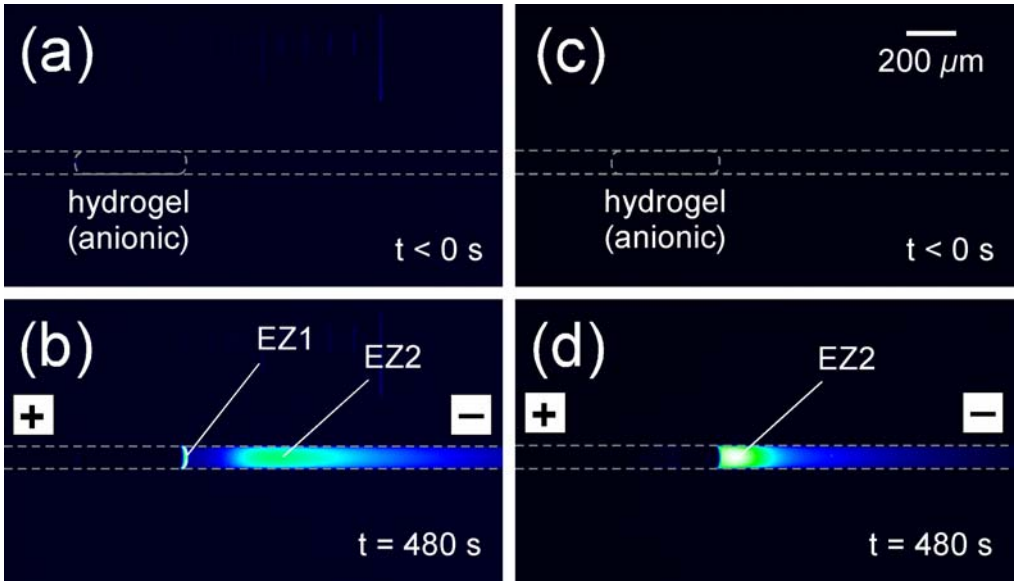

Figure 4.8. Fluorescence micrographs obtained in the microfluidic device (layout shown in Figure 4.2) with the anionic hydrogel microplug for (a) and (b) fluorescein and (c) and (d) for BSA, (a) and (c) before and (b) and (d) after applying a forward bias (100 V for fluorescein and 300 V for BSA) for 480 s. The image size was 512 pixels × 290 pixels, and the grayscale applied was 1700 to 8000 counts per pixel for (a) and (b) while 1700 to 12000 counts per pixel for (c) and (d). The micrographs were modified by using a false color scheme (fluorescence intensity decreasing in the order white-green-blue-black).

the hydrogel microplug. However, the fixed negative charges on the hydrogel backbone give rise to Donnan exclusion effects.[37, 49, 92] Specifically, the hydrogel pore size (~1.6 nm) is on the order of the Debye length (~3.0 nm for a 10 mM 1:1 electrolyte solution),[62] and therefore even the comparatively small co-ionic fluorescein is excluded from the hydrogel interior in this case.[35] This results in concentration enrichment of fluorescein in the vicinity of the hydrogel microplug. Interestingly, however, two enrichment zones are observed: one at the interface between the hydrogel and the solution in the cathodic compartment, and the other a few hundred micrometers away from EZ1 in the cathodic compartment (enrichment zone 2, EZ2).

Figure 4.8(c) and (d) are the micrographs obtained for BSA before and after application of a forward bias of 300 V for 480 s. The local electric field in the cathodic compartment is responsible for transporting BSA towards the hydrogel plug, but it is considerably smaller for the anionic hydrogel compared to the neutral hydrogel because of the concentration polarization effects described earlier. Hence, concentration of BSA by the anionic hydrogel required a higher bias (300 V, see Figure 4.9) compared to fluorescein. Although BSA (pI = 4.9) is size-excluded from the hydrogel, its high negative charge at pH 8.1 also induces electrostatic repulsion from the anionic hydrogel. Consequently, after applying the forward bias, the concentration enrichment peak for BSA is observed near (but not at) the hydrogel-solution interface (Figure 4.8(d)).

Figures 4.10 and 4.11 are fluorescence intensity profiles obtained along the channel for fluorescein and BSA, respectively, at different times following application of the forward bias. The anionic hydrogel acts a cation-exchange membrane and thus

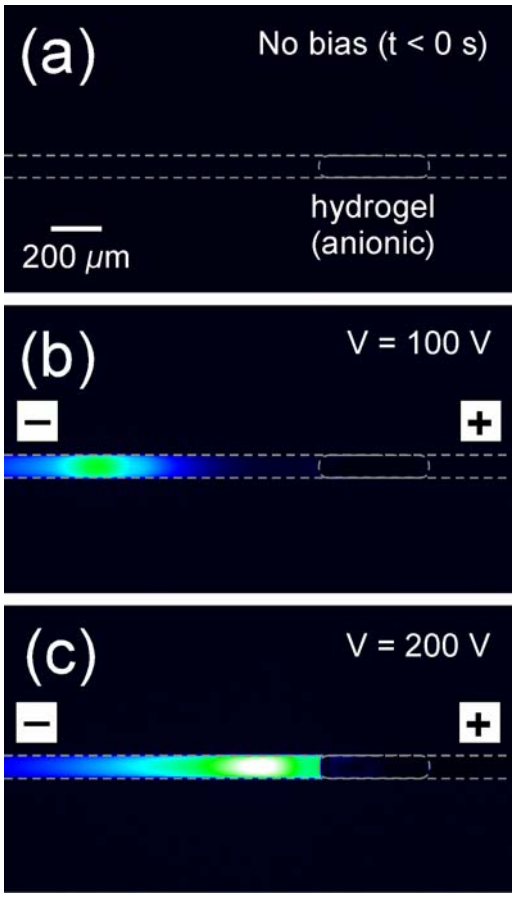

Figure 4.9. Fluorescence micrographs obtained in the microfluidic device (layout shown in Figure 4.2) with an anionic hydrogel microplug for BSA, (a) before applying a bias, and after applying a reverse bias of (b) 100 V and (c) 200 V for 960 s. The image size was 512 pixels × 290 pixels, and the gray scale applied was 1700 to 10000 counts per pixel. The micrographs were modified by using a false color scheme (fluorescence intensity decreasing in the order white-green-blue-black).

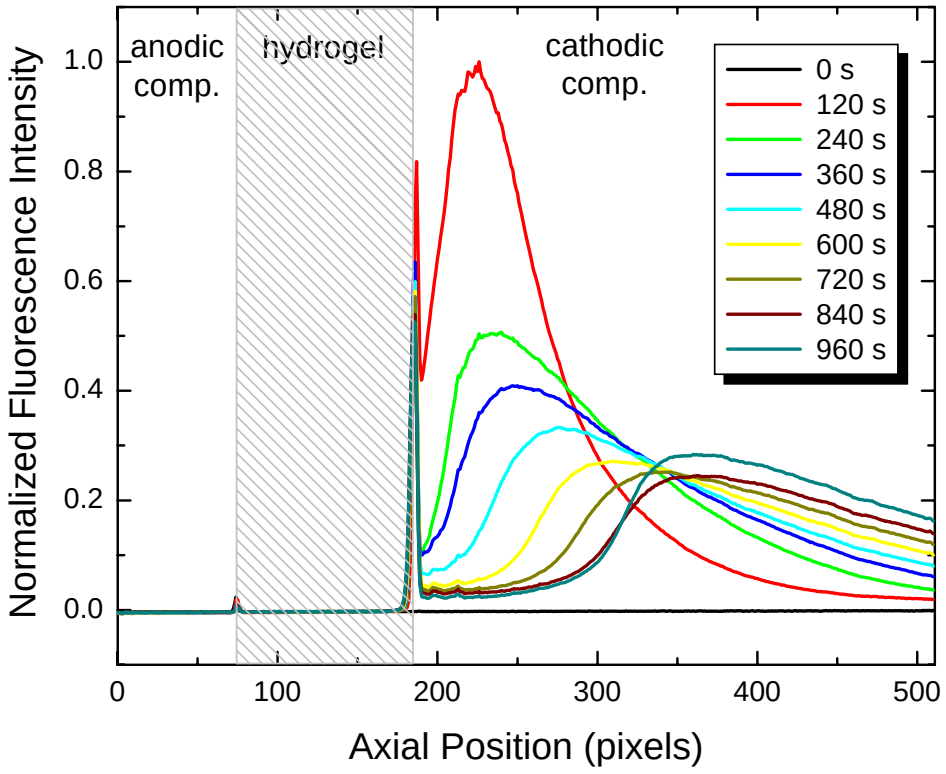

Figure 4.10. Fluorescence intensity profiles for fluorescein obtained parallel to the channel incorporating an anionic hydrogel microplug. All fluorescence intensity values were corrected by subtracting the background count before normalization. Applied potential bias = 100 V (forward).

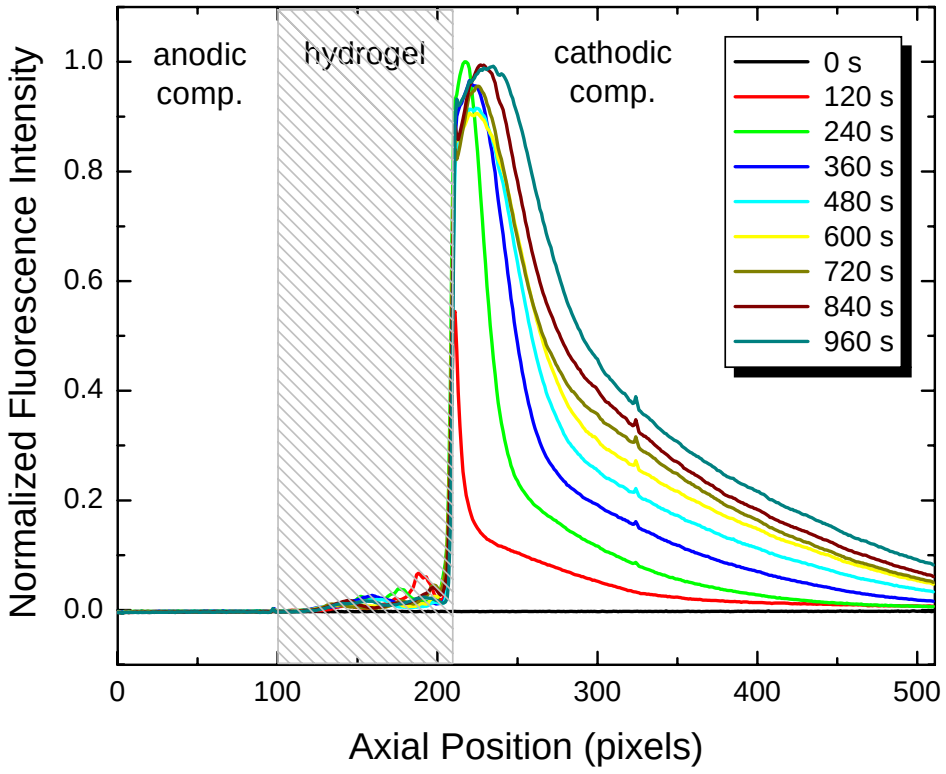

Figure 4.11. Fluorescence intensity profiles for BSA obtained parallel to the channel incorporating an anionic hydrogel microplug. All fluorescence intensity values were corrected by subtracting the background count before normalization. Applied potential bias = 300 V (forward).

preferentially excludes co-ionic species (anions) from the hydrogel matrix by Donnan exclusion. This results in concentration depletion of anions in the anodic compartment and concentration enrichment in the cathodic compartment, that is concentration polarization.[77-79]

As shown in Figure 4.10, when a forward bias is applied across the negatively charged hydrogel microplug, fluorescein molecules in ResB approach the hydrogel in the form of an enriched (concentrated) zone (EZ2, for $t < 120$ s)). Because the hydrogel is impermeable to fluorescein (charge: -2), it acts as a rigid wall to the leading edge of the approaching enriched zone resulting in a sudden rise in the fluorescence intensity and formation of another enriched zone (EZ1) at the hydrogel-solution interface. The fluorescein in EZ1 is partially adsorbed or trapped at the hydrogel-solution interface. At the same time, the presence of fixed charges on the hydrogel generates electroosmotic flow (EOF) inside the hydrogel pores. As discussed earlier, the magnitude of this EOF is smaller than would be possible for larger pores due to overlap of the EDL.[66, 73] Nevertheless, this EOF is strong enough to gradually drive the enriched zone of fluorescein molecules away from the hydrogel. As a result, the fluorescein molecules in EZ1 are slowly removed from the hydrogel surface and EZ2 is displaced away from the hydrogel as a function of time. Similar behavior was observed in experiments carried out using 22-mer and 50-mer single-stranded DNA (ssDNA). The fluorescence intensity profiles obtained along the channel for the two ssDNA oligonucleotides are shown in Figure 4.12 and 4.13.

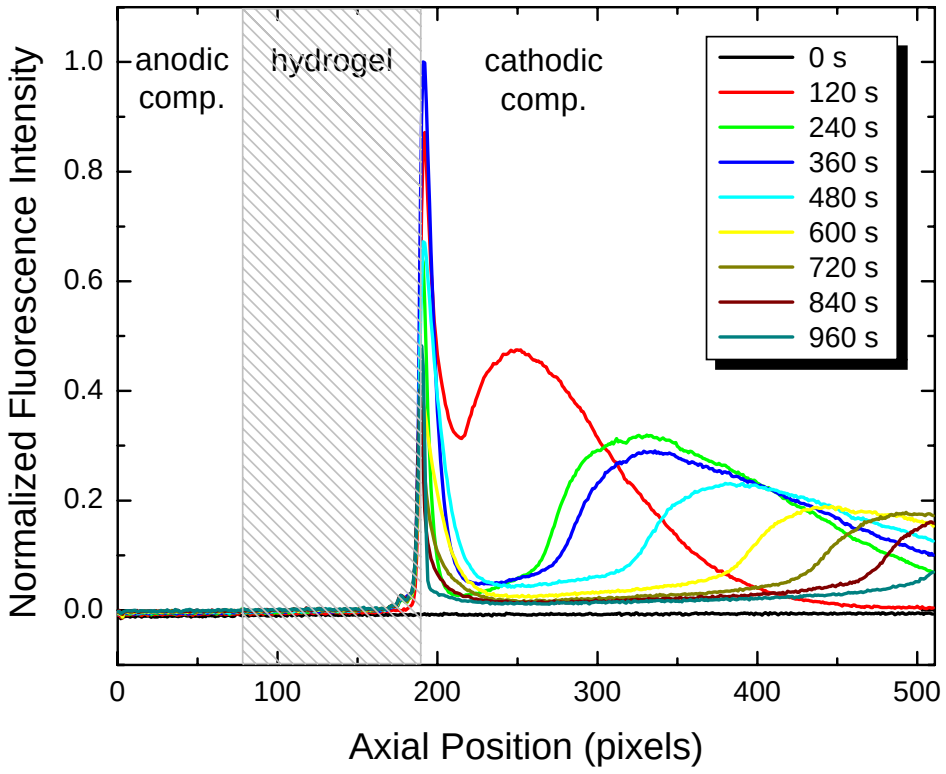

Figure 4.12. The fluorescence intensity profiles for 22-mer ssDNA obtained parallel to the channel incorporating an anionic hydrogel microplug. All fluorescence intensity values were corrected by subtracting the background count before normalization. Applied potential bias = 100 V (forward).

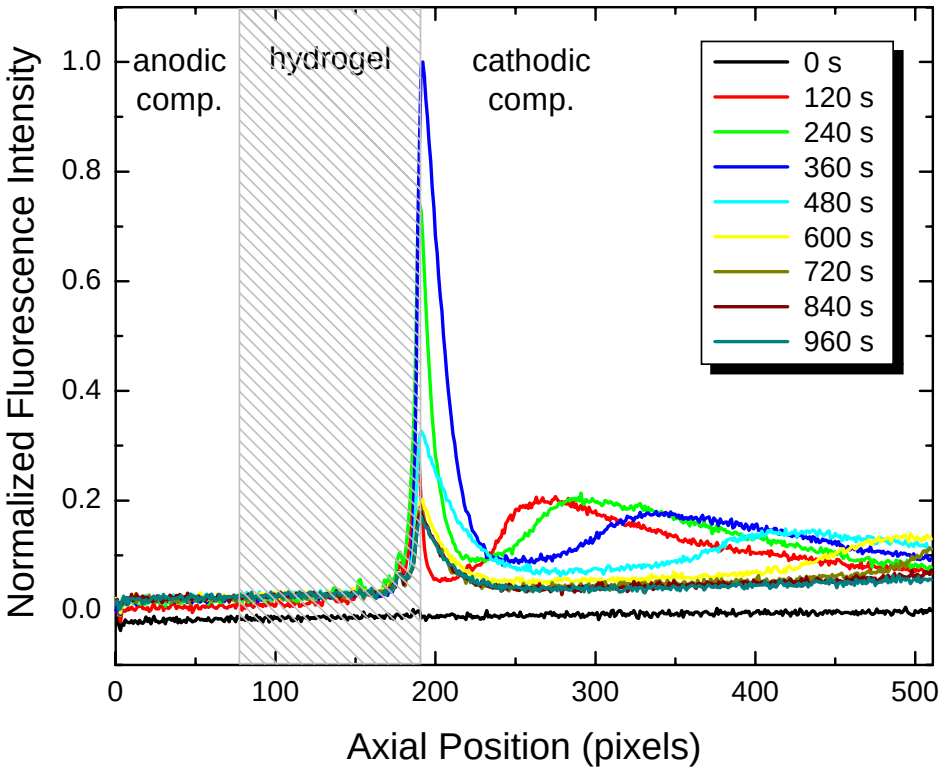

Figure 4.13. The fluorescence intensity profiles for 50-mer ssDNA obtained parallel to the channel incorporating an anionic hydrogel microplug. All fluorescence intensity values were corrected by subtracting the background count before normalization. Applied potential bias = 100 V (forward).

The electrokinetic transport behavior observed for BSA (Figure 4.11) is slightly different than for fluorescein. BSA does not adsorb on the hydrogel surface, and therefore no enrichment zone (EZ1) is observed at the hydrogel-solution interface. However, the simultaneous existence of EOF inside the hydrogel pores was observed to slowly drive the EZ2 away from the hydrogel. This behavior was further verified in a subsequent reverse bias (ResB at positive potential and ResA grounded) carried out at 300 V (Figure 4.14). A small amount of BSA was observed to leak between the hydrogel and the channel walls due to inefficient sealing of the hydrogel plug.

The current flowing through the microfluidic system and concentration enrichment factors obtained during the forward bias are compared for fluorescein and BSA in Figure 4.15. As for the neutral hydrogel case, the current (dotted lines) drops rapidly after an initial rise (during the first 10 s after application of the bias, not shown) and then approaches a steady-state condition. For fluorescein, there is approximately 80 and 100-fold increase in the enrichment factor for EZ2 and EZ1 (black and grey solid squares), respectively, within the first 120 s after application of a 100 V forward bias. Due to the intrahydrogel EOF and lowering of the local electric field due to redistribution of the applied electric field in the cathodic compartment, these enrichment factors decrease for $t > 120$ s reaching a near-steady-state value. For BSA, no concentration enrichment zone is observed at the hydrogel-solution interface (i.e., EZ1 is absent). BSA continues to concentrate in EZ2 for 240 s before attaining a near-constant enrichment factor of ~400. The longer time period (240 s compared to 120 s for fluorescein) of initial increase in the concentration for BSA could be due to the

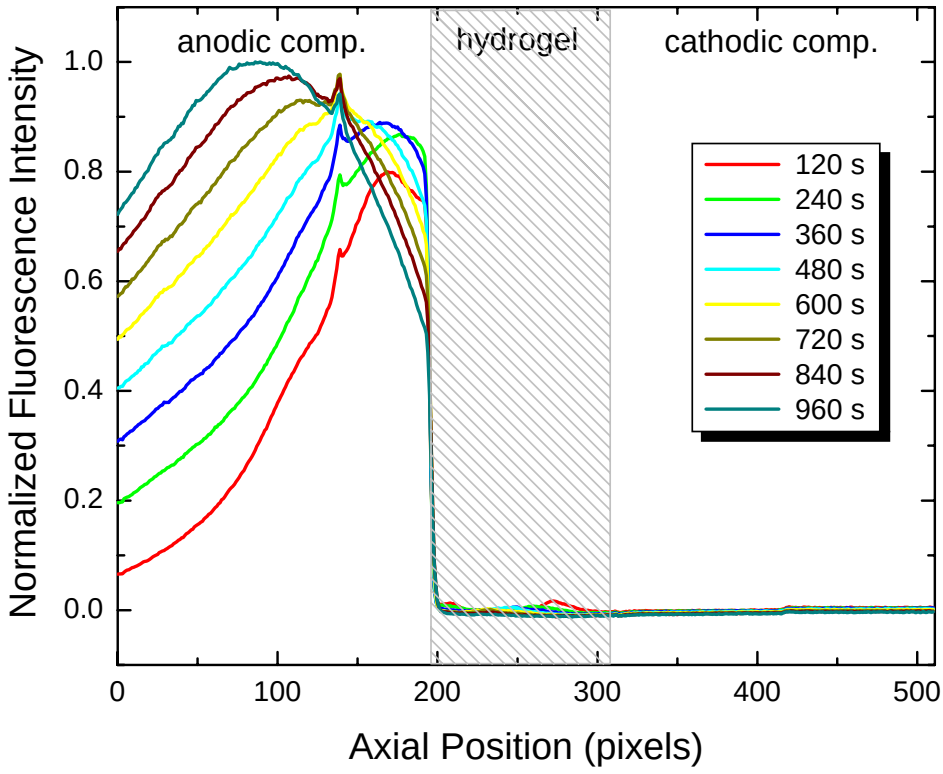

Figure 4.14. The fluorescence intensity profiles for BSA obtained parallel to the channel incorporating an anionic hydrogel microplug. All fluorescence intensity values were corrected by subtracting the background count before normalization. Applied potential bias = 300 V (reverse).

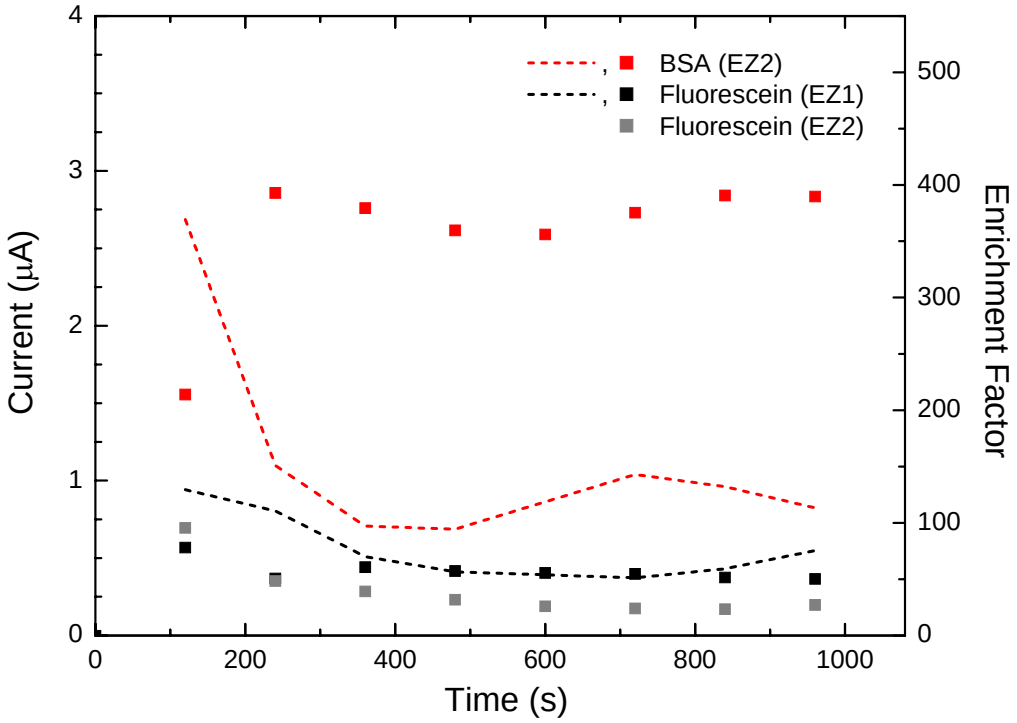

Figure 4.15. Current (dotted lines) flowing through the microfluidic channel and the concentration enrichment factors (solid squares) observed at the interface between the hydrogel microplug and the solution in the cathodic compartment as a function of time for fluorescein and BSA in channels incorporating an anionic hydrogel microplug. The enrichment factors correspond to the respective peak heights in the fluorescence intensity profiles shown in Figures 4.10 and 4.11.

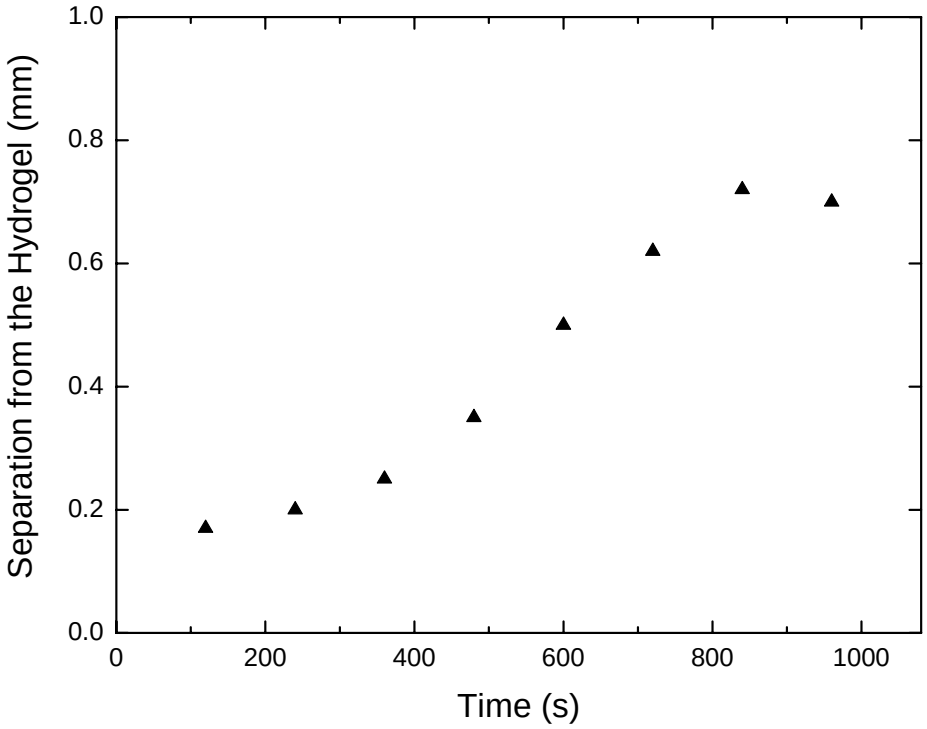

Figure 4.16. Displacement of concentration enrichment zone 2 (EZ2) as a function of time for fluorescein in channels incorporating the anionic hydrogel microplug. Applied potential bias = 100 V (forward).

differences in the local electric field at 300 V bias.

Figure 4.16 shows how the position of EZ2 for fluorescein changes relative to the fixed position of the hydrogel-solution interface as a function of time. Initially, the position of EZ2 is close to the hydrogel, but after about 240 s the EOF generated inside the hydrogel pores displaces EZ2 away from the hydrogel until it is balanced by the electrophoretic flow of fluorescein from the cathode to the anode. For fluorescein, EZ2 was observed to assume a steady location after about 800 s.

On the basis of the behavior described for fluorescein and BSA in the presence of the anionic hydrogel, analyte transport can be roughly divided into two stages: the initial transient stage and the final approach to a steady state. The transient stage ($t < 120$ s for fluorescein and $t < 240$ s for BSA) involves the transport of negatively charged analyte towards the hydrogel in the form of a dispersing zone (EZ2). This could result in an initial overdose (sudden increase in the concentration, for example, EZ1 observed for fluorescein) at the hydrogel-solution interface depending upon the interaction between the analyte and the hydrogel. The concentration enrichment in the cathodic compartment is complemented by a concentration depleted zone in the anodic compartment. In the latter stage, lowering of the local electric field in the cathodic compartment due to the anodic concentration depletion zone reduces the extent of cathodic concentration enrichment. Thus, the concentration enrichment factors obtained for fluorescein (~80 for EZ1 and EZ2 combined, Figure 4.15) are lower than those obtained with the neutral hydrogel (~250, Figure 4.7). For BSA, a higher external electric field (300 V compared to 100 V for fluorescein) is required to obtain enrichment factors (~400) similar to the

neutral hydrogel case. Additionally, the generation of intrahydrogel EOF displaces EZ2 away from the hydrogel. Eventually, the microfluidic system incorporating the nanoporous hydrogel microplug progresses towards a steady-state with respect to the current and the analyte concentration distribution.

4.5 Summary and Conclusions

We have described a simple microfluidic system for concentrating charged analytes using a hydrogel microplug as a transport modulator. The results are interpreted in terms of how the hydrogel interacts with two charged analytes: fluorescein and BSA, which differ mainly in their size. A neutral hydrogel plug can be employed as a physical barrier to the electrophoretic transport of charged analytes resulting in size-based concentration enrichment, while a negatively charged hydrogel plug relies on its physicochemical character for modulation of the electrokinetic transport. Application of an electric field across the anionic hydrogel triggers concentration polarization due to Donnan exclusion effects resulting in size and charge-based concentration enrichment of the charged analytes. However, the enrichment with anionic hydrogel is less efficient compared with the neutral hydrogel owing to the redistribution of the local electric field and simultaneous generation of EOF inside the hydrogel. These experiments and their interpretation provide insight into the fundamental properties of hydrogel microplugs in controlling the transport of charged species inside microfluidic channels.

CHAPTER V

SUMMARY, CONCLUSIONS AND FUTURE OUTLOOK

5.1 Summary and Conclusions

In this dissertation, a simple and efficient approach for concentration of charged molecules in microfluidic devices has been developed. The approach rests on *in-situ* fabrication of hydrogel microplugs using UV projection photopolymerization technique compatible with standard microfabrication methodologies. It has been shown that by subjecting such microfluidic system incorporating a nanoporous hydrogel microplug to an appropriate electric field, electrokinetic concentration enrichment of the charged analyte can be achieved near the hydrogel/solution interface. The initial studies led to concentration enrichment factors as high as 500 within 150 s for negatively charged molecules like ssDNA at low bias voltages of 100 V using an uncharged hydrogel microplug. Parallel studies with a hydrogel carrying fixed negative charges on its backbone, however, presented an unexpected result. A negatively charged hydrogel, although restricted the permeation of negatively charged analyte, resulted in degradation of the concentration enrichment efficiency. Considering the potential of the electrokinetic concentration enrichment approach, it was essential to develop a better theoretical understanding of the intriguing behavior. Further, it was also necessary to modify the microchannel design to eliminate the side channels embedded for the removal of unwanted hydrogel precursor and subsequently prevent the loss of analyte away from the hydrogel microplug.

A microfluidic layout devised without side channels provided a clear incentive in terms of understanding the fundamentals of the electrokinetic enrichment phenomena observed within the microfluidic system by lowering the number of system variable that affect the electrokinetic transport. Correspondingly, a new electrokinetic strategy was developed for the removal of unpolymerized hydrogel precursor.

The electrokinetic studies carried out in the new microfluidic device integrated with a nanoporous hydrogel plug led to some key findings. The microfabricated hydrogel microplug acts as a transport modulator and provides an interesting case of complex electrokinetic events occurring at phase boundaries between the hydrogel and the buffer solution within the microchannel. The physicochemical properties of the hydrogel, including its internal pore size, charge and extent of crosslinking determine the mode of the electrokinetic concentration enrichment. A neutral hydrogel plug acts as a physical barrier to the electrophoretic transport of charged analytes resulting in size-based concentration enrichment. On the other hand, a negatively charged hydrogel plug introduces concentration polarization due to Donnan exclusion effects resulting in size and charge-based concentration enrichment of the charged analytes. However, the enrichment with anionic hydrogel is less efficient compared with the neutral hydrogel owing to the redistribution of the local electric field and simultaneous generation of EOF inside the hydrogel. We have provided a simple theoretical model that is qualitatively consistent with the experimental observations for analytes with different sizes, charge, and physicochemical properties. The experiments and their theoretical interpretation

provide insight into the fundamental properties of hydrogel microplugs in controlling the transport of charged species inside microfluidic channels.

5.2 Future Outlook

The remarkable aspect of the work is the development of integrated micro-nano fluidic system with nanoporous hydrogel microplug as a functional component modulating the electrokinetic transport phenomena such as concentration enrichment. It shows an excellent potential in altering the transport mechanism by controlling the physicochemical properties of the hydrogel. This objective will require a detailed knowledge of all the facets of the integrated micro-nano fluidic system.

Presently, simulation and modeling studies are underway in collaboration with Dr. Ulrich Tallarek (Institut für Verfahrenstechnik, Otto-von-Guericke-Universität Magdeburg, Germany) for elucidating the fundamental information about the system. The preliminary iterations using COMSOL Multiphysics software are in accordance with the work presented. Upon successful implementation of the computer simulations consistent with the experimental studies, it may be possible to optimize the electrokinetic concentration enrichment methodology for lowering the detection limit for a variety of on-chip bio-assays.

REFERENCES

1. Manz, A.; Graber, N.; Widmer, H. M. *Sens. Actuators, B* **1990**, *1*, 244-248.
2. Manz, A. *Chimia* **1996**, *50*, 140-143.
3. Reyes, D. R.; Iossifidis, D.; Auroux, P.-A.; Manz, A. *Anal. Chem.* **2002**, *74*, 2623-2636.
4. Lichtenberg, J.; de Rooij, N. F.; Verpoorte, E. *Talanta* **2002**, *56*, 233-266.
5. Ashton, R.; Padala, C.; Kane, R. S. *Curr. Opin. Biotechnol.* **2003**, *14*, 497-504.
6. de Mello, A. J.; Beard, N. *LabChip* **2003**, *3*, 11N-19N.
7. Mogensen, K. B.; Klank, H.; Kutter, J. P. *Electrophoresis* **2004**, *25*, 3498-3512.
8. Chien, R.-L. *Electrophoresis* **2003**, *24*, 486-497.
9. Jung, B.; Bharadwaj, R.; Santiago, J. G. *Electrophoresis* **2003**, *24*, 3476-3483.
10. Lichtenberg, J.; Verpoorte, E.; de Rooij, N. F. *Electrophoresis* **2001**, *22*, 258-271.
11. Chien, R.-L.; Burgi, D. S. *Anal. Chem.* **1992**, *64*, 1046-1050.
12. Broyles, B. S.; Jacobson, S. C.; Ramsey, J. M. *Anal. Chem.* **2003**, *75*, 2761-2767.
13. Yu, C.; Davey, M. H.; Svec, F.; Frechet, J. M. J. *Anal. Chem.* **2001**, *73*, 5088-5096.
14. Gebauer, P.; Bocek, P. *Electrophoresis* **2000**, *21*, 3898-3904.
15. Walker, P. A., III; Morris, M. D.; Burns, M. A.; Johnson, B. N. *Anal. Chem.* **1998**, *70*, 3766-3769.
16. Beckers, J. L.; Everaerts, F. M. *J. Chromatogr.* **1990**, *508*, 3-17.
17. Ross, D.; Locascio, L. E. *Anal. Chem.* **2002**, *74*, 2556-2564.

18. Koegler, W. S.; Ivory, C. F. *J. Chromatogra., A* **1996**, *726*, 229-236.

19. Huang, Z.; Ivory, C. F. *Anal. Chem.* **1999**, *71*, 1628-1632.

20. Righetti, P. G.; Bossi, A. *Anal. Chim. Acta* **1998**, *372*, 1-19.

21. Hatch, A. V.; Herr, A. E.; Throckmorton, D. J.; Brennan, J. S.; Singh, A. K. *Anal. Chem.* **2006**, *78*, 4976-4984.

22. Song, S.; Singh, A. K.; Kirby, B. J. *Anal. Chem.* **2004**, *76*, 4589-4592.

23. Khandurina, J.; Jacobson, S. C.; Waters, L. C.; Foote, R. S.; Ramsey, J. M. *Anal. Chem.* **1999**, *71*, 1815-1819.

24. Foote, R. S.; Khandurina, J.; Jacobson, S. C.; Ramsey, J. M. *Anal. Chem.* **2005**, *77*, 57-63.

25. Sera, Y.; Matsubara, N.; Otsuka, K.; Terabe, S. *Electrophoresis* **2001**, *22*, 3509-3513.

26. Quirino, J. P.; Terabe, S. *Anal. Chem.* **1999**, *71*, 1638-1644.

27. Han, J. C., H. G. *Science* **2000**, *288*, 1026-1029.

28. Walker, G. M.; Beebe, D. J. *LabChip* **2002**, *2*, 57-61.

29. Dai, J.; Ito, T.; Sun, L.; Crooks, R. M. *J. Am. Chem. Soc.* **2003**, *125*, 13026-13027.

30. Kuo, T.-C.; Cannon, D. M. J.; Chen, Y.; Tulock, J. J.; Shannon, M. A.; Sweedler, J. V.; Bohn, P. W. *Anal. Chem.* **2003**, *75*, 1861-1867.

31. Cannon, D. M. J.; Kuo, T.-C.; Bohn, P. W.; Sweedler, J. V. *Anal. Chem.* **2003**, *75*, 2224-2230.

32. Tulock, J. J.; Shannon, M. A.; Bohn, P. W.; Sweedler, J. V. *Anal. Chem.* **2004**, *76*, 6419-6425.

33. Ismagilov, R. F.; Ng, J. M. K.; Kenis, P. J. A.; Whitesides, G. M. *Anal. Chem.* **2001**, *73*, 5207-5213.

34. Cummings, E. B.; Griffiths, S. K.; Nilson, R. H.; Paul, P. H. *Anal. Chem.* **2000**, *72*, 2526-2532.

35. Dhopeshwarkar, R.; Sun, L.; Crooks, R. M. *LabChip* **2005**, *5*, 1148-1154.

36. Peppas, N. A.; Huang, Y.; Torres-Lugo, M.; Ward, J. H.; Zhang, J. *Annu. Rev. Biomed. Eng.* **2000**, *2*, 9-29.

37. Hoffman, A. S. *Adv. Drug Delivery Rev.* **2002**, *43*, 3-12.

38. Nguyen, K. T.; West, J. L. *Biomaterials* **2002**, *23*, 4307-4314.

39. Jen, A. C.; Wake, M. C.; Mikos, A. G. *Biotechnol. Bioeng.* **1995**, *50*, 357-364.

40. Hubbell, J. A. *J. Control. Release* **1996**, *39*, 305-313.

41. An, Y.; Hubbell, J. A. *J. Control. Release* **2000**, *64*, 205-215.

42. Elisseeff, J.; Anseth, K.; Sims, D.; McIntosh, W.; Randolph, M.; Yaremchuk, M.; Langer, R. *Plast. Reconstr. Surg.* **1999**, *104*, 1014-1022.

43. Mann, B. K.; Gobin, A. S.; Tsai, A. T.; Schmedlen, R. H.; West, J. L. *Biomaterials* **2001**, *22*, 3045-3051.

44. Heo, J.; Crooks, R. M. *Anal. Chem.* **2005**, *77*, 6843-6851.

45. Yadavalli, V. K.; Koh, W.-G.; Lazur, G. J.; Pishko, M. V. *Sens. Actuators, B* **2004**, *97*, 290-297.

46. Mao, C.; Kisaalita, W. S. *Biosens. Bioelectron.* **2004**, *19*, 1075-1088.

47. Fesenko, D. O.; Nasedkina, T. V.; Prokopenko, D. V.; Mirzabekov, A. D. *Biosens. Bioelectron.* **2005**, *20*, 1860-1865.

48. Zhang, X.; Wang, S.; Hu, M.; Xiao, Y. *Biosens. Bioelectron.* **2006**, *21*, 2180-2183.

49. Peppas, N. A.; Khare, A. R. *Adv. Drug Delivery Rev.* **1993**, *11*, 1-35.

50. De, S. K.; Aluru, N. R.; Johnson, B.; Crone, W. C.; Beebe, D. J.; Moore, J. S. *J. Microelectromech. Syst.* **2002**, *11*, 544-555.

51. Johnson, B. D.; Beebe, D. J.; Crone, W. C. *Mater. Sci. Eng., C* **2004**, *24*, 575-581.

52. Khurmi, R. S. *Strength of Materials*; S. Chand & Co. Ltd.: New Delhi, India, 1998.

53. Wichterle, O.; Lim, D. *Nature* **1960**, *185*, 117-118.

54. Beebe, D. J.; Moore, J. S.; Bauer, J. M.; Yu, Q.; Liu, R. H.; Devadoss, C.; Jo, B.-H. *Nature* **2000**, *404*, 588-590.

55. Ho, C.-M.; Tai, T.-C. *Annu. Rev. Fluid Mech.* **1998**, *30*, 579-612.

56. Gad-el-Hak, M. *J. Fluids Eng.* **1999**, *121*, 5-33.

57. Bird, R. B.; Stewart, W. E.; Lightfoot, E. N. *Transport Phenomena*; John Wiley & Sons: Singapore, 1994.

58. McCabe, W. L.; Smith, J. C.; Harriot, P. *Unit Operations of Chemical Engineering*; McGraw-Hill: Singapore, 1993.

59. Kamholz, A. E.; Yager, P. *Biophys. J.* **2001**, *80*, 155-160.

60. Devasenathipathy, S.; Santiago, J. G. *Microscale Diagnostic Techniques: Chapter 3*; Springer Berlin Heidelberg: New York, 2005.

61. Probstein, R. F. *Physiochemical Hydrodynamics: An Introduction*; John Wiley & Sons, Inc.: New York, 1994.

62. Bard, A. J.; Faulkner, L. R. *Electrochemical Methods: Fundamentals and Applications*; John Wiley & Sons, Inc.: New York, 2000.

63. Shaw, D. J. *Introduction to Colloid and Surface Chemistry*; Butterworths: London, United Kingdom, 1980.

64. Duffy, D. C.; McDonald, J. C.; Schueller, O. J. A.; Whitesides, G. M. *Anal. Chem.* **1998**, *70*, 4974-4984.

65. Burgreen, D.; Nakache, F. R. *J. Phys. Chem.* **1964**, *68*, 1048-91.

66. Rice, C. L.; Whitehead, R. *J. Phys. Chem.* **1965**, *69*, 4017-4024.

67. Patankar, N. A.; Hu, H. H. *Anal. Chem.* **1998**, *70*, 1870-1881.

68. Herr, A. E.; Molho, J. I.; Santiago, J. G.; Mungal, M. G.; Kenny, T. W.; Garguilo, M. G. *Anal. Chem.* **2000**, *72*, 1053-1057.

69. Brotherton, C. M.; Davis, R. H. *J. Colloid Interface Sci.* **2004**, *270*, 242-246.

70. Kirby, B. J.; Hasselbrink, E. F. J. *Electrophoresis* **2004**, *25*, 187-202.

71. Kirby, B. J.; Hasselbrink, E. F. J. *Electrophoresis* **2004**, *25*, 203-213.

72. Ermakov, S. V.; Jacobson, S. C.; Ramsey, J. M. *Anal. Chem.* **1998**, *70*, 4494-4504.

73. Rathore, A. S.; Guttman, A. *Electrokinetic Phenomena*; Marcel Dekker, Inc.: New York, 2004.

74. Rubinstein, I. *J. Chem. Soc., Faraday Trans. 2* **1981**, *77*, 1595-609.

75. Rubinstein, I.; Maletzki, F. *J. Chem. Soc., Faraday Trans.* **1991**, *87*, 2079-87.

76. Rubinstein, I.; Zaltzman, B. *Phys. Rev. E* **2000**, *62*, 2238-2251.

77. Leinweber, F. C.; Tallarek, U. *Langmuir* **2004**, *20*, 11637-11648.

78. Leinweber, F. C.; Pfafferodt, M.; Seidel-Morgenstern, A.; Tallarek, U. *Anal. Chem.* **2005**, *77*, 5839-5850.

79. Tallarek, U.; Leinweber, F. C.; Nischang, I. *Electrophoresis* **2005**, *26*, 391-404.

80. Snita, D.; Paces, M.; Lindner, J.; Kosek, J.; Marek, M. *Faraday Dis.* **2001**, *120*, 53-66.

81. Pu, Q.; Yun, J.; Temkin, H.; Liu, S. *Nano Lett.* **2004**, *4*, 1099-1103.

82. Plecis, A.; Schoch, R. B.; Renaud, P. *Nano Lett.* **2005**, *5*, 1147-1155.

83. Garcia, A. L.; Ista, L. K.; Petsev, D. N.; O'Brien, M. J.; Bisong, P.; Mammoli, A. A.; Brueck, S. R. J.; Lopez, G. P. *LabChip* **2005**, *5*, 1271-1276.

84. Minteer, S. D. *Microfluidic Techniques: Reviews and Protocols*; Humana Press, Inc.: New Jersey, 2006.

85. Madou, M. M. *Fundamentals of Microfabrication: The Science of Miniaturization*; CRC Press: New York, 2002.

86. Senturia, S. D. *Microsystem Design*; Springer Science+Business Media, Inc.: New York, 2001.

87. Xia, Y.; Whitesides, G. M. *Annu. Rev. Mater. Sci.* **1998**, *28*, 153-184.

88. Campbell, D. J.; Beckman, K. J.; Calderon, C. E.; Doolan, P. W.; Ottosen, R. M.; Ellis, A. B.; Lisensky, G. C. *J. Chem. Educ.* **1999**, *75*, 537-541.

89. McDonald, J. C.; Duffy, D. C.; Anderson, J. R.; Chiu, D. T.; Hongkai, W.; Schueller, O. J. A.; Whitesides, G. M. *Electrophoresis* **2000**, *21*, 27-40.

90. Ren, X.; Bachman, M.; Sims, C.; Li, G. P.; Allbritton, N. *J. Chromatogr. B* **2001**, *762*, 117-125.

91. Ocvirk, G.; Munroe, M.; Tang, T.; Oleschuk, R.; Westra, K.; Harrison, D. J. *Electrophoresis* **2000**, *21*, 107-115.

92. Donnan, F. G. *J. Membr. Sci.* **1995**, *100*, 45-55.

93. Bruin, G. J. M. *Electrophoresis* **2000**, *21*, 3931-3951.

94. Olsen, K. G.; Ross, D. J.; Tarlov, M. J. *Anal. Chem.* **2002**, *74*, 1436-1441.

95. Oleschuk, R. D.; Shultz-Lockyear, L. L.; Ning, Y.; Harrison, D. J. *Anal. Chem.* **2000**, *72*, 585-590.

96. Han, J.; Craighead, H. G. *Science* **2000**, *288*, 1026-1029.

97. Khoury, C.; Adalsteinsson, T.; Johnson, B.; Crone, W. C.; Beebe, D. J. *Biomed. Microdevices* **2003**, *5*, 35-45.

98. De, S. K.; Aluru, N. R.; Johnson, B.; Crone, W. C.; Beebe, D. J.; Moore, J. S. *J. Microelectromech. Syst.* **2002**, *11*, 544-555.

99. Seong, G. H.; Zhan, W.; Crooks, R. M. *Anal. Chem.* **2002**, *74*, 3372-3377.

100. Heo, J.; Thomas, K. J.; Seong, G. H.; Crooks, R. M. *Anal. Chem.* **2003**, *75*, 22-26.

101. Zangmeister, R. A.; Tarlov, M. J. *Anal. Chem.* **2004**, *76*, 3655-3659.

102. Zangmeister, R. A.; Tarlov, M. J. *Langmuir* **2003**, *19*, 6901-6904.

103. Revzin, A.; Russell, R. J.; Yadavalli, V. K.; Koh, W.-G.; Deister, C.; Hile, D. D.; Mellott, M. B.; Pishko, M. V. *Langmuir* **2001**, *17*, 5440-5447.

104. Canal, T.; Peppas, N. A. *J. Biomed. Mater. Res.* **1989**, *23*, 1183-1193.

105. Nakane, J. J.; Akeson, M.; Marziali, A. *J. Phys.: Condens. Matter* **2003**, *15*, R1365-R1393.

106. Bezrukov, S. M. *J. Membr. Biol.* **2000**, *174*, 1-13.

107. *CRC Handbook of Chemistry and Physics;* Weast, R. C., Ed.; CRC Press: Boca Raton, FL, 1989.

108. Griffith, O. H.; Houle, W. A.; Kongslie, K. F.; Sukow, W. W. *Ultramicroscopy* **1984**, *12*, 299-308.

109. Whitesides, G. M. *Nature (London, United Kingdom)* **2006**, *442*, 368-373.

110. Eijkel, J. C. T.; van den Berg, A. *Microfluidics Nanofluidics* **2005**, *1*, 249-267.

111. Mijatovic, D.; Eijkel, J. C. T.; van den Berg, A. *LabChip* **2005**, *5*, 492-500.

112. Peters, T., Jr. *Adv. Protein Chem.* **1985**, *37*, 161-245.

113. Song, S.; Singh, A. K. *Anal. Bioanal. Chem.* **2006**, *384*, 41-43.

VITA

Rahul Rajesh Dhopeshwarkar received his Bachelor of Engineering in Chemical Engineering degree from Shivaji University, Kolhapur, India in May 2000. His Ph.D. studies in Chemical Engineering were completed under the guidance of Prof. Richard M. Crooks at Texas A&M University, College Station in August 2007.

Rahul Dhopeshwarkar's permanent address is Department of Chemical Engineering, Texas A&M University, 3122 TAMU, College Station, TX 77843-3122.